Transient and Pulsed Electron Paramagnetic Resonance Spectroscopy on Type I Photosynthetic Reaction Centers

by

Reza Siavashi MSc.

A THESIS SUBMITTED IN PARTIAL FULFILMENT OF

THE REQUIREMENTS FOR THE DEGREE OF

MASTER OF SCIENCE

in

The Faculty of Mathematics and Sciences

Department of Physics

BROCK UNIVERSITY

August 26, 2014

In presenting this thesis in partial fulfillment of the requirements for advanced degree at Brock University, I agree that the Library shall make it freely available for reference and study. I further agree that permission for extensive copying of this thesis for scholarly purposes may be granted by the head of my department or by his or her representatives. It is understood that copying or publication of this thesis for financial gain shall not be allowed without my written permission.

Signature: _____

Department of Physics
Brock University
500 Glenridge Avenue
St. Catharines, Ontario
Canada, L2S 3A1

Date: _____

To my Beautiful Wife

Abstract

Two time-resolved EPR techniques, have been used to study the light induced electron transfer(ET) in Type I photosynthetic reaction centers(RCs).

First, pulsed EPR was used to compare PsaA-M688H and PsaB-M668H mutants of *Chlamydomonas reinhardtii* and *Synechosystis* sp. PCC 6803.The out-of-phase echo modulation curves combined with other EPR and optical data show that the effect of the mutations is species dependent.

Second, transient and pulsed EPR data are presented which show that PsaA-A660N and PsaB-A640N mutations in *C. reinhardtii* alter the relative quantum yield of ET in the A- and B-branches of PS I.

Third, transient EPR studies on RCs from *Heliobacillus mobilis* that have been exposed to oxygen show partial inhibition of ET. In the RCs in which ET still occurs, the ET kinetics and EPR spectra show evidence of oxidation of some but not all of the, BChl *g* and BChl $g^{'}$ to Chl *a.*

Acknowledgment

First and foremost, I would like to express my special gratitude to my supervisor **Prof. Art van der Est**, for his patience, motivation, enthusiasm, and immense knowledge. I could not have asked for a better a supervisor and mentor. Thank you for your ever-present willingness to answer my questions.

My special thanks to my friend Sam Mula for helpful discussions and sharing his knowledge and positive energy during the time we shared an office.

Special thanks to our collaborators:

- Prof. John Golbeck, Dr. Junlei Sun and Bryan Ferlez at Pennsylvania State University.
- Profs. Kevin Redding and Andrew Webber, Dr. Mike McConnell and Syed Badshah at Arizona State University.

Thank you to Dr. Harroun for the encouragement at my committee meetings. I also thank Dr. Mitrovic. Special thanks to Dr. Stefan Stoll, my external examiner from University of Washington, for reading my thesis and his valuable comments.

I am very grateful for receiving financial support from department of physics and thank everyone at the department especially, Dr. Shyamal K. Bose for his wonderful advanced quantum mechanics classes.

Koosha, Yousef, Andrew, Farzan and all my great friends during my stay in St. Catharines, thank you all for the beautiful time and your friendly supports. I will never forget you.

Last but not least, I would like to thank my family for their kindly support.

To my wife:

YOU ARE INDEED THE BEAUTY OF MY LIFE.

Contents

List of Tables X

List of Figures XI

List of Abbreviations XIV

1 Introduction 1

2 Principles of Electron Paramagnetic Resonance 12

2.1 Free Electron in a Static Magnetic Field 13

2.2 Electron in an Atom or Molecule and the Zeeman Interaction 14

2.3 Two Interacting Electrons 17

2.3.1 Electron-Exchange Interaction 18

2.3.2 Electron-Electron Dipolar Interaction 19

2.4 Hyperfine Interaction 21

2.5 Relaxation Process in EPR Spectroscopy 22

3 Theory of Spin Correlated Radical Pairs 25

3.1 Eigenvalues and Eigenfunctions of the Two Electron Spin System in a Static Magnetic Field 25

3.2 Density Operator Formalism to Study the Spin Dynamics of the RPs 29

3.3 Time Evolution of the Density Operator 31

3.4 Transition Between States and EPR Signal Intensity 35

4 Time-Resolved EPR and its Application in Studying Electron Transfer in PS I and Heliobacterial Reaction Centers 40

4.1 Transient EPR: Experimental Spectra 40

4.1.1 The Effect of ESP on Transient EPR spectra 42

4.1.2 Sequential RP and the effect of precursors on Transient EPR signal 43

4.2 Pulsed EPR 45

4.2.1 Time Evolution of the Density Operator and Magnetization 46

5 An Out of Phase Electron Spin Echo Study of PsaA-M688H and PsaB-M668H mutants of two different species 51

5.1 The concept of directionality in ET 51

5.2 Point Mutagenesis Studies to Address the Directionality of ET 52

5.3 Literature Review on the Preparation and Behavior of PsaA-M688H 53

and PsaB-M668H 53

5.4 Experimental Setup for OOP-ESEEM Experiment 55

5.5 Results and Discussion 56

6 PsaA-A680N and PsaB-A660N, Transient EPR and Pulsed EPR Studies 66

6.1 Transient and Pulsed EPR Setup 68

6.2 Room Temperature X-band Transient EPR Results 69

6.3 Low Temperature X-band Transient EPR Results 72

6.4 Low Temperature Q-band Transient EPR Results 73

6.4 Low Temperature OOP-ESEEM Results 75

6.5 Summary of the results 77

7 Transient EPR Studies of the Oxidation of Heliobacterial Reaction Centers 78

7.1 Transient EPR Setup at X-band and Q-band 82

7.2 X-band and Q-band Transient EPR Results..... 82

7.3 Discussion on the Results 87

8 Bibliography 90

List of Tables

Table 5.1: The parameters used for fitting the experimental OOP-ESEEM modulation curves of $P_{700}^{+}PhQ^{-}$. 64

Table 7.1: Normalization factor for the X-band and Q-band spectra 85

Table 7.2: The parameters used to simulate the decays of the spectrum presented in Figure 7.6. The error in t_1 and t_2 is 0.1 ms. 87

List of Figures

Figure 1.1: Arrangement of the electron transport cofactors in PS I. A-branch and B-branch denote the two branches of PS I which are discussed in the text.. 4

Figure 1.2: The lifetimes of sequential ET in Photosystem I, along with mid-point potential of cofactors 6

Figure 1.3: A comparison of Type I and Type II RCs. 8

Figure 3.1: Energy Scheme for a coupled two electrons system.. 28

Figure 3.2: Stick spectrum for an RP generated from a singlet precursor 37

Figure 4.1: Time/Field EPR dataset. 42

Figure 4.2: Timing diagram for the out-of-phase-echo experiment. 48

Figure 5.1: .Top: The arrangement of the methionine residue PsaA-M688 in wild type PS I, between A_0 of the A-branch(chlorophyll $ec3_A$) and phylloquinone molecules; Bottom: A structural model in which the methionine residue has been replaced with histidine. 54

Figure 5.2: Room temperature spin-polarized transient EPR spectra of Wild Type, PsaA-M688H and PsaB-M668H of *Synechocystis* sp. PCC 6803 (Left) and *C. reinhardtii* (Right) 59

Figure 5.3: Spin polarized Transient EPR of Wild Type, PsaA-M688H and PsaB-M668H of *Synechocystis* sp. PCC 6803 (Left) and *C. reinhardtii*is (Right) at 80 K. 60

Figure 5.4: OOP-ESEEM spectra at 80 K.. 63

Figure 6.1: Position of alanine on each branch in PS I represented by yellow color. 67

Figure 6.2: Position of alanine between the $ec2_A$ and $ec3_A$ chlorophyll molecules and the PhQ molecule in the A-branch of PS I RC [120]. 68

Figure 6.3: Room temperature X-band spin-polarized transient EPR.. 70

Figure 6.4 Spin polarized X-band spectrum for Wild Type, PsaA-A680N and PsaB-A660N of *C. reinhardtii* for at 80 K 73

Figure 6.5: Polarized Q-band Transient EPR for Wild Type, PsaA-A680N and PsaB-A660N of *C. reinhardtii* at 80 K 74

Figure 6.6: Theoretical prediction for Q-band A and B branch ET spectra. 75

Figure 6.7: OOP-ESEEM spectra for WT, PsaA-A680N and PsaB-A660N and the fitting traces for three spectra..... 76

Figure 7.1: Absorption spectra of anaerobic (red) and aerobic (green) of heliobacterial cells [126]. 80

Figure 7.2: Chemical structure of 8^1-OH Chl *a* (top left) and BChl *g* (top right) and Chl a_F (bottom). 80

Figure 7.3 Transient EPR spectra at X-band of aerobic sample (T_0) and anaerobic samples (T_1 to T_4) of *Hb*RCs at 80 K.. 83

Figure 7.4: Transient EPR spectra at X-band of aerobic sample (T_0) and anaerobic samples (T_1 to T_4) of *Hb*RCs at 80 K using direct detection of EPR signals. .84

Figure 7.5:Transient EPR spectra at Q-band of aerobic sample (t_0) and anaerobic samples (T_1 to T_4) of *Hb*RCs at 80 K using direct detection of signals. 84

Figure 7.6: Decays of the X-band Transient EPR signal at 80 K using field modulation detection. 86

List of Abbreviations

A_0	Primary Electron Acceptor
A_1	Secondary Electron Acceptor
BChl	Bacteriochlorophyll
Chl	Chlorophyll
Chl a_F	Chlorophyll *a* with farnesyl side chain
C. reinhardtii	*Chlamydomonas reinhardtii*
ENDOR	Electron Nuclear Double Resonance
EPR	Electron Paramagnetic Resonance
ESEEM	Electron Spin Echo Envelope Modulation
ESP	Electron Spin Polarization
ET	Electron Transfer
Hb.	*Heliobacillus*
hfc	hyperfine coupling
OOP-ESEEM	Out of Phase echo-ESEEM
P	Primary Electron Donor
PhQ	Phylloquinone
PS I	Photosystem I
PS II	Photosystem II
RC	Reaction Centre
RP	Radical Pair
TR	Time Resolved
WT	Wild Type

1 Introduction

It can be argued that photosynthesis is the most important biological process on earth. Directly or indirectly all of the biological energy on earth is provided by photosynthesis accomplished by plants. Moreover, the oxygen in the atmosphere is one of the other important products of photosynthesis. The average solar energy flux hitting the earth is about 340.4 W/m^2 [1], and it can be used as an energy source for our daily needs. By photosynthesis this energy is converted into chemical energy in the form of chemical compounds like the reducing agent NADPH (reduced form of Nicotinamide Adanine Dinucleotide Phosphate) and adenosine triphosphate (ATP) as a chemical energy transporter within cells, and in some cases oxygen as a byproduct (for a review see [2–4]). Another issue that makes the importance of the solar energy more evident is the expected energy crisis in the aspects of limited source of energy and pollution caused by fossil fuels. However, the most significant problem associated with storing solar energy is the fact that it is very diffuse. Understanding the basic Chemistry and Physics of photosynthesis is important for designing man-made solar energy harvesting devices and hopefully, will lead to the development of new, efficient solar energy harvesting technologies based on the natural process (for a review on the progress and efficiency of artificial photosynthesis see [5]). Furthermore,

understanding the details of photosynthesis can help in agriculture by increasing the efficiency of food production [6].

During the past 250 years since the first investigations by J. Priestley, who demonstrated that plants produce a gas (later named oxygen), much has been learned about the chemical and physical aspects of photosynthesis. However, some aspects of the primary process of converting light energy quanta into electrochemical energy are not fully understood [2]. This initial energy conversion takes place in membrane-bound proteins called reaction centers (RCs). Unraveling the details of the structure and function of the RCs provides knowledge that can be used for designing solar energy conversion systems [7].

Generally, there are two types of photosynthesis: oxygenic photosynthesis, which occurs in plants, green algae and cyanobacteria, and anoxygenic photosynthesis, which occurs in purple bacteria, green bacteria and heliobacteria [8]. All photosynthetic organisms that produce oxygen have two types of pigment–protein complexes named Photosystem II (PS II) and Photosystem I (PS I) [9]. In these complexes, solar energy conversion is carried out by a chain of Electron Transfer (ET) steps. PS II oxidizes water and transfers electrons to plastoquinone, while PS I transfers electrons from plastocyanin to ferredoxin and ultimately to $NADP^+$. Thus, together the ET through PS II and PS I results in water oxidation and production of reduced NADP (NADPH) [8]. In contrast, anoxygenic (anaerobic) bacteria only use one RC [10], which is similar to either PS I or PS II. However, the ET in anaerobic bacteria is cyclic and it is used to generate the proton gradient needed to make ATP [7].

The main focus of this thesis is Electron Paramagnetic Resonance (EPR) studies on PS I RCs and *Heliobacillus* (*Hb*) RCs. Before introducing EPR, a brief review of the structures of the two RCs of particular interest is given in this chapter.

PS I is the protein complex of the thylakoid membrane that acts as the mediator of light induced ET from plastocyanin in the lumen to ferredoxin on the stromal side of membrane [11]. PS I is a large membrane protein comprised of 12 protein subunits, which binds 96 chlorophyll *a* (Chl *a*) molecules, 22 carotenoids that act as a light harvesting system and 6 chlorophylls, two phylloquinones and three iron-sulfur clusters that act as the ET chain [12]. The core of PS I is composed of the PsaA and PsaB protein subunits and the ET chain cofactors [13]. The antenna complex, composed of chlorophylls and carotenoid molecules absorbs photons of light and transfer the energy to the core of PS I. Once the core of PS I gets excited, the ET starts across the cofactors of PS I complex.

All photosynthesic organisms have a primary electron donor, which is a chlorophyll dimer. These dimers are referred to as P_{680}, P_{700}, P_{865}, etc, where P stands for pigment and the subscript is the wavelength in nm at which the pigment has its maximum absorption. In PS I, the donor is P_{700} and because it is composed of two different chlorophylls (chlorophyll *a* / chlorophyll *a*′) it is referred as a heterodimer donor. Once the P_{700} core donates the electron, there are two branches of cofactors in PS I where the ET process potentially can take place. These two branches are shown as the A-branch and B-branch in Figure 1.1, which shows a structural model of the ET cofactors in PS I derived from the 2.5 Å resolution X-ray structure [14]. It is known that both branches are active but their relative use and the factors controlling the directionality of ET in PS I are still under debate and study. However, the main photophysical reaction that occurs in PS I is [13]:

$$P_{700} \xrightarrow{h\upsilon} P_{700}^{*} \rightarrow P_{700}^{+}A_0^{-} \rightarrow P_{700}^{+}A_1^{-} \rightarrow P_{700}^{+}F_x^{-} \rightarrow P_{700}^{+}F_{A/B}^{-}$$

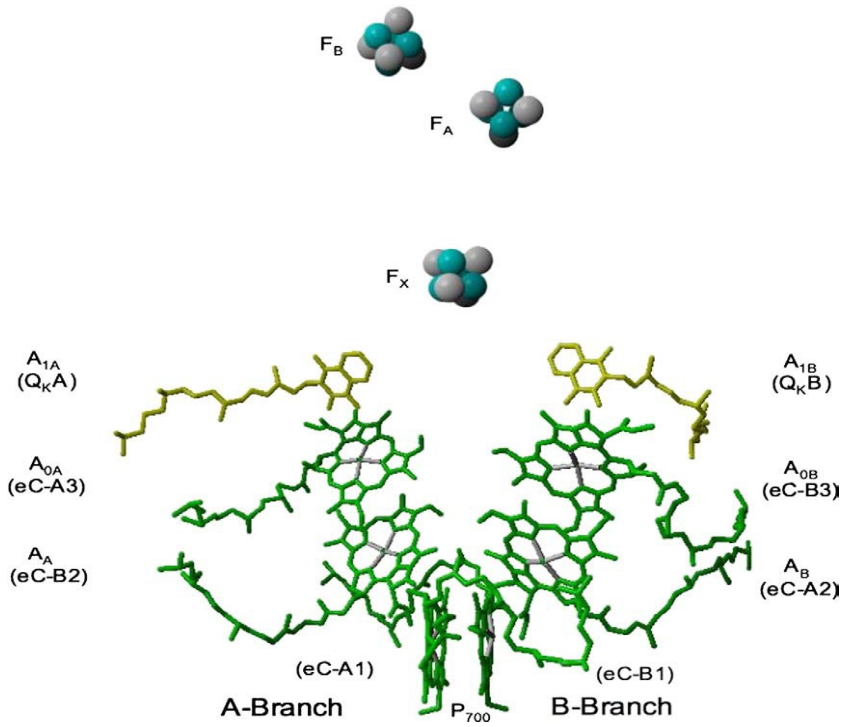

Figure 1.1: Arrangement of the electron transport cofactors in PS I. A-branch and B-branch denote the two branches of PS I which are discussed in the text. The spectroscopic names and the structural names (in parentheses) are indicated near each cofactor. (used with permission from [15]**).**

As mentioned before, the primary donor in PS I is a chlorophyll *a* / chlorophyll *a*¢ heterodimer (P_{700}). The location of initial charge separation in PS I is still under debate, because it is hard to clearly separate the excitation energy transfer and ET reaction[16]. There are two models describing charge separation in PS I. The first model suggests that light absorption gives rise to an excited singlet state of the primary donor (P^*_{700}), either directly or indirectly by energy transfer from antenna. P^*_{700} then transfers an electron to the chlorophyll *a* molecule (A_0), producing the radical pair $P_{700}^+A_0^-$ [13]. This model is supported by a recent study by Shelaev et al. who showed that if PS I complexes are excited at 720 nm by a laser pulse, the charge-separated state $P_{700}^+A_0^-$ is formed within 10 fs as an initial charge-separated state [16]. The second model for primary charge separation in PS I is suggested by Holzwarth and co-workers [17]. These authors proposed that the primary charge-separated state may not be $P_{700}^+A_0^-$, and that the lifetime of the initial charge separation is about 6-9 ps. In a later study, the same group [18] obtained absorption difference spectra for three different states

with lifetimes of 3, 14, and 25 ps. They attributed these spectra to $A_B^+A_{0A}^-$, $P_{700}^+A_{0A}^-$ and $P_{700}^+A_1^-$ respectively, indicating that the primary charge-separated state is $A_B^+A_{0A}^-$.

The secondary acceptor is a phylloquinone molecule (A_1). The lifetime of ET from A_0^- to A_1 to form the radical pair $P_{700}^+A_1^-$ is about 30 ps [18–21]. The next step of ET is oxidation of A_1^- and reduction of the first iron-sulfur cluster which is F_x in Figure1.1 [22, 23]. Interestingly, two different lifetimes of approximately 20 and 200 ns have been measured for this ET step [13, 24–27]. These two phases correspond to B-branch and A-branch ET respectively [29].

At cryogenic temperature, the $P_{700}^+F_x^-$ state decays with a lifetime of ~1 ms, and the state $P_{700}^+F_{A/B}^-$ is stable over days or more. If the iron-sulfur clusters are removed, back reaction from A_1^- to P_{700}^+ occurs with a lifetime of approximately 10 and 100 µs [30]. There is evidence that the electron acceptor after F_x is F_A and after that F_B [31]. However, the kinetics of ET between these clusters is not known with certainty. There are measurements in the literature that suggest that the lifetime of ET from F_x to F_A is approximately 180 ns and from F_x to F_B is less than 500 ns [31, 32]. In Figure 1.2 a summary of the lifetimes of the ET through Photosystem I along with the midpoint potentials of the cofactors is presented.

Another RC of interest in this study is the *Hb*RC. To introduce this type of RC, in the following paragraph the two general types of RCs are discussed briefly.

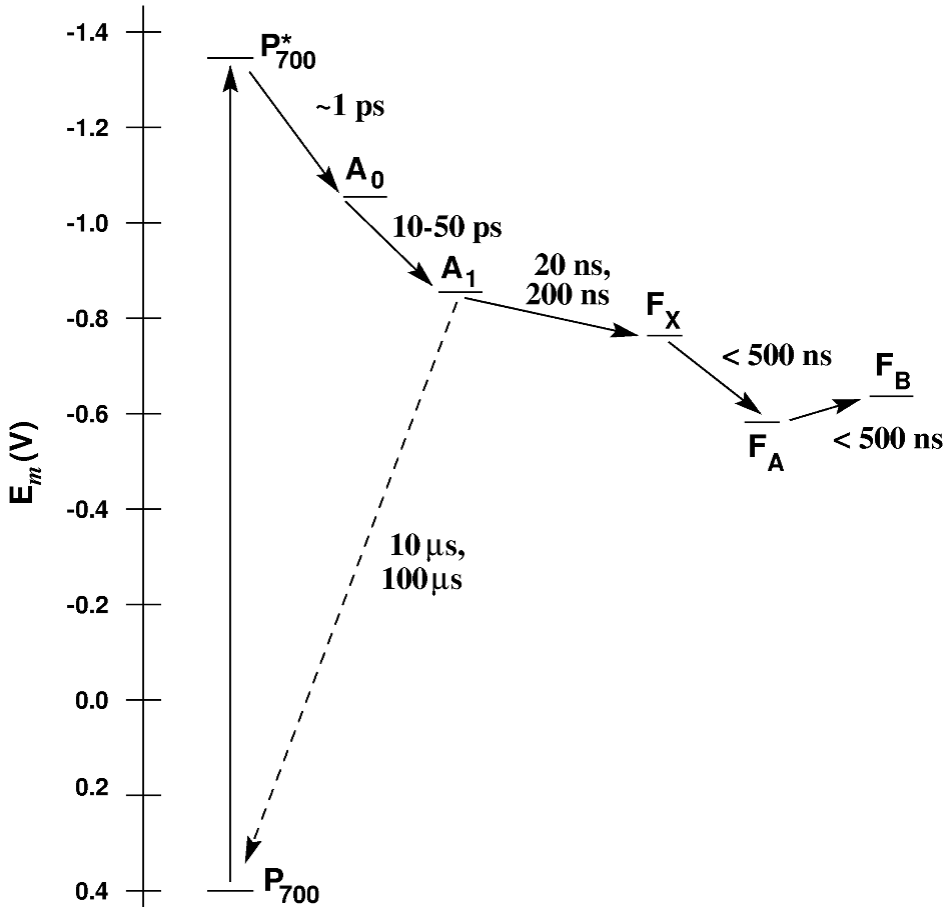

Figure 1.2: The lifetimes of sequential ET in Photosystem I, along with mid-point potential of cofactors. All the numbers are average accepted values in the literature. (Taken from [34]**, Used with permission of the publisher) .**

Generally, there are two types of photosynthetic RCs referred to as Type I and Type II [9]. In the Figure.1.3, the difference between Type I and Type II RCs is illustrated. Type I RCs are also known as iron-sulfur type RCs, because they employ iron-sulfur (Fe_4S_4) clusters as terminal electron acceptors. Type II RCs are also known as quinone-type reaction centers, because they employ quinones as electron acceptors [7]. In different photosynthetic organisms, either type I or type II RCs or both can be found. In higher plants, green algae and cyanobacteria two types of RCs exist [11]. What both types RCs have in common is that the primary electron donor is a chlorophyll dimer and two branches of cofactors that extend across the membrane from the donor. In PS I the two proteins, PsaA and PsaB, that bind the ET cofactors are different. Therefore, the core of PS I is a protein dimer made up of two different proteins

and it is referred to as a heterodimeric RC. Heliobacterial RCs are other example of Type I RCs. In heliobacteria two molecules of the same protein, PshA, bind the cofactors. Therefore, the *Hb*RC is a protein dimer made up of two identical proteins so it is referred to as a homodimeric RC [7]. This is indicated by the color difference of the ovals in the Figure 1.3, and the oval themselves represent the main protein subunit in each species. In Type I homodimers (such as RCs from Green-Sulfur bacteria and heliobacteria) it is assumed that electrons are transferred up both branches [35]. The situation in heterodimeric PS I is a little more complicated and will be explained later, but here in the figure it is assumed both branches are active in ET. Type II RCs are also subdivided into the heterodimeric, oxygen-evolving PS II RC and the heterodimeric, purple bacterial RC [7]. In Type II RC the ET occurs in just one branch [8], so the arrows in the Figure 1.3 are shown in just one branch. Briefly, in type II RCs when the primary donor is excited the ET starts. The first acceptor in purple bacteria is a accessory chlorophyll [36], and in PS II, it has been proposed that the initial charge separation is between a accessory chlorophyll and pheophytin [37]. Then, the electron is transferred to a bound plastoquinone molecule referred as Q_A. Q_A then donates the electron to plastoquinone $Q_{B,}$ which is a mobile electron carrier. In PS II when Q_B is doubly reduced it picks up two protons from the stroma. The doubly reduced and doubly protonated plastoquinone cannot bind to the binding site and diffuses away. Because it is a non-polar molecule it stays in the membrane. However, it does not stay on the stromal side but diffuses throughout the membrane and eventually releases the two protons into the lumen when it donates its two electrons to the cytochrome b_6f complex. This process is essentially the same in anaerobic bacterial type II RC, except that the two sides of the membrane are called the cytoplasm and periplasm not stroma and lumen. Finally the mobile plastoquinone will be replaced by a fresh plastoquinone [38]. In Figure 1.3, FeS and Q_B stand for iron-sulfur clusters and a mobile quinone molecule as terminal electron acceptors in type I and type II RCs respectively. X-ray crystal structures have been determined for the purple bacterial RC [39], PS I [40] and PS II [41]. For green-

sulfur bacterial RCs, only low resolution scanning transmission electron micrographs are available [42], and there is no structural information available for *Hb*RC.

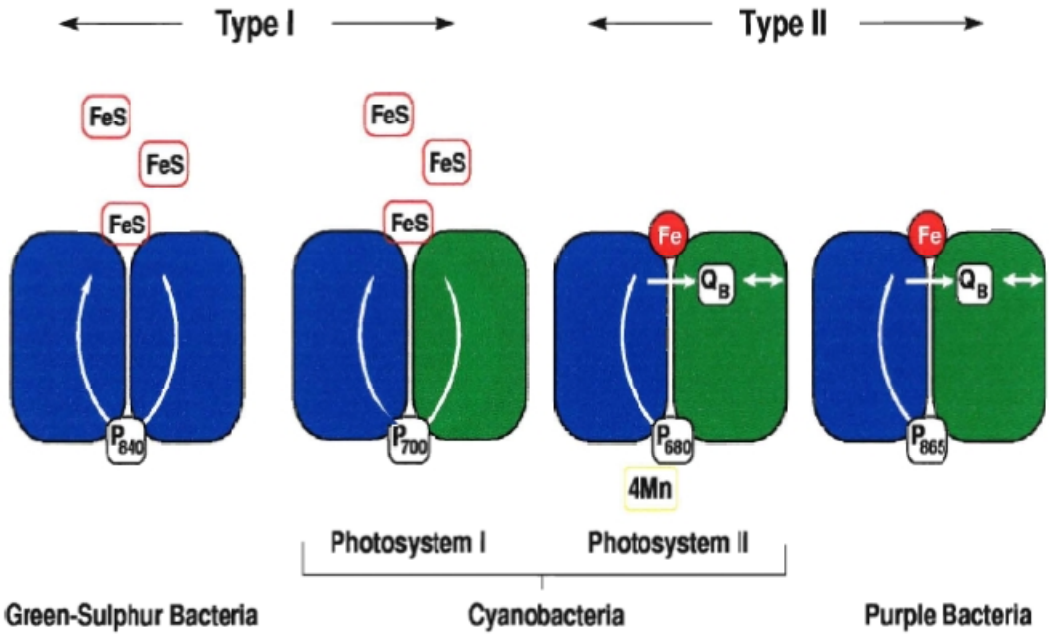

Figure 1.3: A comparison of Type I and Type II RCs. Used with permission [34]**.**

The main similarity between *Hb*RC and PS I is that both have iron-sulfur clusters as terminal acceptors [43], which is why they are both categorized as a Type I RCs. The protein pigment that makes *Hb*RC special among the bacterial RCs is bacteriochlorophyll g (BChl g) [44]. In the presence of light and oxygen, Bchl g isomerizes to Chl *a* [45]. The primary donor in *Hb*RC is a homodimer of BChl g′ [7], which is named P_{798}. Like P_{700} in PS I, 798 here refers the wavelength of maximum bleaching following excitation with light [45, 46]. The primary acceptor, A_0, is a BChl *a* molecule [48], and the charge separation

between P_{798} and A_0 happens in 1–2 ps [49]. The lifetime of forward ET transfer from A_0 is about 600 ps [47] at room temperature, and the back reaction between P_{798} and A_0 occurs in about 17 ns [50]. Unlike PS I, the participation of a quinone cofactor in the ET process in *Hb*RC is under debate. Although *Hb*RCs are known to contain two menaquinone molecules [51], optical and photovoltage kinetic experiments along with EPR studies have not shown any signatures of a functional quinone in the ET of *Hb*RC [51, 52]. A transient EPR spectrum of a radical pair in which one of the radicals has quinone-like properties has recently been reported for chemically reduced *Hb*RC at 14 K [54]. However, it is unclear whether this species has any relevance for ET under physiological conditions. There is strong evidence in support of an iron-sulfur cluster analogous to F_X in PS I as the secondary acceptor in *Hb*RC [7, 54]. The PshB protein houses two iron-sulfur clusters analogous to F_A and F_B in PS I. [54–58]. However, PshB is bound very loosely to the RC core and it is unclear whether it can be considered an integral part of the *Hb*RC.

The ET in PS I and *Hb*RCs generates a series of sequential radical pairs. These radical pairs are spin-correlated because they are generated on a timescale that is too short for the correlation present in the excited singlet state of the primary donor to be lost [59, 60]. Electron spin polarization (ESP) which is non-Boltzmann population of the spin state is a result of this correlation [62].

Electron Paramagnetic Resonance (EPR) is a spectroscopic technique which is one the most important biophysical methods employed to study ET in photosynthetic RCs [63]. By EPR spectroscopy we can detect the magnetic moment of unpaired electrons. In the systems under study in this thesis (PS I and heliobacteria), the light-induced radical pairs can be detected by EPR. We can obtain geometric and kinetic information of radicals because the magnetic moment of electron is sensitive to the local environment. However, there are limitations on detecting some cofactors because the response time of EPR is on order of tens of nanoseconds, so for instance the ET from initial donor to A_0 and

fast phase ET from A_1 to F_x cannot be detected directly. However, the ESP associated with light-induced ET, which increases the EPR signal amplitude by several orders of magnitude, depends on the precursor states [64]. During the lifetime of each radical pair (RP) generated in our system, the two correlated electron spin accumulate a phase difference in their precession and this difference influences the ESP pattern. Therefore at a given time the polarization pattern gives information about precursor RP even if it has a short lifetime [60, 64–67]. In this study, two time-resolved EPR techniques (transient-EPR and Pulsed-EPR) have been employed in order to study the RCs of interest. A brief introduction of the biological aspects of each study is given in the next paragraph, and the details can be found in the related chapter.

As mentioned before, in PS I RCs, ET can take place in the A-branch and B-branch. One of the most important questions is the activity of each branch in the ET process. To address the question of ET directionality, extensive point mutagenesis studies have been carried out on residues that are suspected to play a role in determining the redox potentials of the acceptors [68–75]. Two of the most important residues for mutation studies are the methionine residues PsaA - M688 and PsaB-M668.[1] The sulfur atom of these residues provides an axial ligand to the central Mg^{2+} of A_{0A} and A_{0B}. The effect of replacing methionine with histidine has been studied by a time-resolved pulse-EPR technique called Out of Phase Electron Spin Echo Envelope Modulation (OOP-ESEEM) on PS I from the green alga *Chlamydomonas reinhardtii* and the cyanobacterium *Synechocystis* sp. PCC 6802. In addition, an EPR study of the effect of alteration of alanine residues, PsaA-A680 and PsaB-A660 which have their methyl side chains directed towards the accessory chlorophylls eC-A2 (A_B) and eC-B2 (A_A), repsectively, have been done in PS I RCs of *C.reinhardtii*. The experiments include low temperature (80 K) Q-band, X-band transient EPR and ESEEM-OOP-ESEEM, and room temperature X-band transient EPR.

[1] It should be noted that here the numbering of the amino acids refers to gene sequences of *Synchococcus elongatus*. For other species the numbering is different but we always use the corresponding *Synchococcus. elongatus* numbering to make it easier to compare with the x-ray structure.

Another set of studies has been carried out on *Hb*RCs. As previously mentioned, heliobacteria are anaerobic bacteria, and they contain BChl g, which distinguishes them from other photosynthetic bacteria [7, 42 and 44]. When heliobacteria are exposed to oxygen and in the presence of light, Bchl g is oxidized to Chl *a* [7]. The influence of different chlorophylls on the rate of ET is unknown. Moreover, altering native chlorophylls is very difficult and to date this has only achieved in purple bacteria [77]. By exposing heliobacteria to oxygen and light, the effect of changing BChl *g* to Chl *a* on the rate and yield of ET can be studied by EPR.

After a brief introduction into the principles of EPR in the next chapter, the basic Hamiltonian for the spin correlated radical pairs to study light-induced ET in photosynthetic RC is derived and introduced in Chapter 3. Following that, in Chapter 4, the principles of the transient EPR, and Pulsed EPR experiments are explained. The next three chapters are devoted to describing the previously mentioned EPR experiment results on PS I and heliobacteria RCs.

2 Principles of Electron Paramagnetic Resonance

EPR[2] is a spectroscopic method for studying of paramagnetic species. This method established around 1945 as a result of research in the Soviet Union by Zavoisky and independently in England by Bleaney shortly after Zavoisky. This method and the related nuclear magnetic resonance (NMR) technique both make use of the magnetic resonance phenomenon, in the first case on electrons in the second on nuclei. EPR is based on the absorption (or emission) of electromagnetic radiation, which is usually in the microwave frequency region, by a paramagnetic sample placed in a magnetic field. The absorption (emission) takes place only for specific frequencies and magnetic field combinations, depending on the sample characteristics, which means that the absorption (emission) is resonant. The microwave technology in the frequency range 10^9 Hz and higher that is normally employed in EPR instruments had been developed for radar detection units during the Second World War. Today, EPR has a huge range of applications in the fields of physics, chemistry, biology, earth sciences, material sciences, and other branches of science (for several reviews see [62, 77 and 78]). Various species such as radicals, radical ions,

[2]Also is known as ESR: Electron Spin Resonance, they are synonyms. In this thesis we use EPR.

paramagnetic metal complexes, excited states with S>0 can be detected by EPR. As mentioned in the introduction the systems of particular interest in this thesis have sequential Radical Pairs (RPs). To understand the EPR data that are expected from such RPs, we first need to know the most important interactions in the system to construct the Hamiltonian. In this chapter these interactions are introduced.

2.1 Free Electron in a Static Magnetic Field

Electrons like all other elementary particles have intrinsic angular momentum referred to as spin. However, spin is a purely quantum mechanical property and cannot be interpreted as the rotation of electron about one of its axes. In fact, it does not have any classical counterpart and model. Electron spin angular momentum was first discovered by Stern and Gerlach and was developed by Uhlenbeck and Goudsmit [79, 80]. The magnetic dipole generated by electron spin is:

$$\boldsymbol{\mu}_e = -g_e\beta\boldsymbol{S} \tag{2.1}$$

β is the Bohr magneton $\beta = \frac{e\hbar}{2m_e}$, and g_e is the free electron g-factor, which is equal to 2.002 319 304 368 (20) [78], and $\boldsymbol{S}$ is the spin angular momentum of the electron. In the presence of a static magnetic field in the *z*-direction, free electrons can exist in two quantum states with the *z*-component of $\boldsymbol{\mu}_e$ aligned either anti-parallel ($|+>$ state) or parallel ($|->$ state) relative to the magnetic field. The energies of the two states differ as a result of the interaction of the magnetic dipole with the magnetic field and are given by:

$$E = m_s g_e \beta B_0 \tag{2.2}$$

where m_s is the quantum number for the *z*-component of the spin angular momentum. If a transition occurs between these two states based on the

selection rule $\Delta m_s = \pm 1$, emission or absorption of electromagnetic radiation with the following energy is possible:

$$\Delta E = g_e \beta B_0 = h\upsilon \tag{2.3}$$

The value of $g_e\beta/h$ is about 28 GHz/T. Thus, the frequency υ of the electromagnetic radiation lies in the microwave region with the magnetic fields around 0.3 to 3 Tesla, which are usually applied in EPR spectroscopy.

2.2 Electron in an Atom or Molecule and the Zeeman Interaction

If we consider the simple case of a single electron in an atom, the electron angular momentum has two contributions: one from the electron spin like a free electron, and another from the orbital motion of the electron around the nucleus. The magnetic moment is the sum of two terms, referring to the two contributions:

$$\mu_e = \mu_B \boldsymbol{L} + g\mu_B \boldsymbol{S} \tag{2.4}$$

Here $\boldsymbol{L}$ is orbital angular momentum. This equation is correct if the orbital and spin part of the wave-function and as a result their related contribution in the Hamiltonian can be divided into a part that only affects the spin part and another just affects the spatial part of wave-function. In reality, they are not, because spin and orbit angular momentum are coupled by the spin–orbit coupling. However, the spin-orbit coupling is often weak and we can separate the two parts of the wavefunction to a good approximation [78].

In most cases we are dealing with electrons in molecules. The symmetry of molecules is much lower than that of atoms and as a result the spin-orbit coupling, which depends on the movement of the electron in all directions relative to the nuclei in the system, is approximately averaged to zero, and its

effect can be described by replacing the free electron g-value eqn. (2.1) with a g-factor whose value varies between different molecules. The consequence of this variation is a change in the resonance frequency from the value corresponding to the free electron spin in eqn. (2.3). Because the g-factor deviation from the free electron g-value depends on the spin–orbit coupling, for heavy nuclei its value is large because the average distance between the electron and the nucleus decreases as the nuclear charge increases. For molecules containing light atoms, the deviation is smaller, but still important, because even such small deviations give important structural information, as well as information about the local environment. In general, the strength of the spin-orbit interaction depends on the relative orientation of the orbital angular momentum ($\boldsymbol{L}$) and spin angular momentum ($\boldsymbol{S}$) vectors. Therefore, the g-value, depends on the orientation of the molecule relative to the static magnetic field in an EPR experiment. So, in order to treat the g-factor more conveniently it is described as a matrix. If the orientation of the molecule in the static magnetic field ($\boldsymbol{B_0}$) is described by the vector **n** in the molecular frame, the effective g-value measured along this direction is [62, 81]**:**

$$g_{\text{eff}}(\theta, \varphi) = \sqrt{\mathbf{n^T g g^T n}} \tag{2.5}$$

In which :

$$\mathbf{n}(\theta, \varphi) = \begin{pmatrix} \sin\theta\cos\varphi \\ \sin\theta\sin\varphi \\ \cos\theta \end{pmatrix} \tag{2.6}$$

and$\theta, \varphi$are the polar and azimuthal angles describing **n** with respect to the principal axis system of **g**. To construct the Hamiltonian for this interaction, we make the approximation that the wavefunctions can be written as the product of a spatial and an spin part:

$$|\Psi(x,y,z)>.|\psi(m_s)> \tag{2.7}$$

where $|\Psi(x,y,z)>$ represents the spatial part of the wavefunction, and $|\psi(m_s)>$ denotes the spin part. The latter is either $|+>$ or $|->$, and m_s has a value of +1/2 or -1/2. Then the energies of the system can be calculated from the time-independent Schrödinger eqn.

$$\widehat{\mathcal{H}}|\psi_i> = E_i|\psi_i> \tag{2.8}$$

E_i is the energy of the spin-system. The interaction of an unpaired electron spin with the external static magnetic field, is named the Zeeman interaction, and its contribution to the Hamiltonian can be expressed as :

$$\widehat{\mathcal{H}}_{eZ} = \beta\, \boldsymbol{B_0 g \hat{S}} \tag{2.9}$$

In this equation, $\hat{\mathbf{S}}$ denotes the spin operator and **g** is the g-tensor of the unpaired electron, in which the spin-orbit coupling has been taken into account. The energies of the $|+>$ and $|->$states are:

$$\begin{aligned} E_+ &= +\frac{1}{2} g_{eff} \beta B_0 \\ E_- &= -\frac{1}{2} g_{eff} \beta B_0 \end{aligned} \tag{2.10}$$

The g-tensor can be diagonalized to be represented by its principal values, g_{xx} ,g_{yy} , g_{zz}. In liquid samples, because the rapid tumbling of molecules, the anisotropic part of g-tensor is averaged to zero [77, 81 and 82], and there is just a isotropic contribution in the form of:

$$g_{iso} = \frac{1}{3} (g_{xx} + g_{yy} + g_{zz}) \tag{2.11}$$

2.3 Two Interacting Electrons

Some molecular systems have two unpaired electron spins. Two electrons in the same orbital have the same energy and are spin paired because of the Pauli Exclusion Principle. Two electrons in different orbitals can have different energies and are spin unpaired. If there is no coupling between the two electrons, the possible eigenstates of the system are:

$$|++> \quad |+-> \quad |-+> \quad |--> \tag{2.12}$$

But if coupling exists between the two electrons, the eigenstates are linear combinations of the states in eqn. 2.12. For the RPs in photosynthetic RCs, the coupling between the two electrons has to be taken into account [61]. This coupling can be divided into two parts: an isotropic part, which is due to the exchange interaction, and an anisotropic part which is due to the dipolar interaction. For light-induced RPs, the initial state of the system is either a pure singlet state or a pure triplet state. Hence, it would be more convenient to use singlet-triplet wavefunctions as a basis set:

$$\begin{aligned} |T_+> &= |++> \\ |S> &= \frac{1}{\sqrt{2}}|+-> - \frac{1}{\sqrt{2}}|-+> \\ |T_0> &= \frac{1}{\sqrt{2}}|+-> + \frac{1}{\sqrt{2}}|-+> \\ |T_-> &= |--> \end{aligned} \tag{2.12}$$

By definition, the triplet state is symmetric and the singlet state is antisymmetric with respect to exchange of the electrons. Based on the Pauli exclusion principle, if the two electrons occupy the same orbital, only the singlet configuration is possible for electron spins, but if they occupy different orbitals, both singlet and triplet configurations are possible.

2.3.1 Electron-Exchange Interaction

The exchange interaction results in an energy difference between the singlet and triplet states. The spin Hamiltonian that represents this interaction is :

$$\widehat{\mathcal{H}}_{exch} = \sum_{ij} J_{ij} \widehat{\boldsymbol{S}}_{1i} \widehat{\boldsymbol{S}}_{2j} = \frac{1}{2} (\widehat{\boldsymbol{S}}_1^T . \boldsymbol{J} . \widehat{\boldsymbol{S}}_2 + \widehat{\boldsymbol{S}}_2^T . \boldsymbol{J} . \widehat{\boldsymbol{S}}_2) \qquad (2.13)$$

Here, indices i and j represent the spatial coordinates, 1 and 2 denote the two electrons. $\boldsymbol{J}$ is a 3×3 matrix that describes the exchange integral part of the Coulombic interaction between the two unpaired electrons [84]. As mentioned before, singlet and triplet states are antisymmetric and symmetric with respect to exchange of electrons. Based on the Pauli principle, the spatial part of the wavefunctions should be symmetric and antisymmetric respectively. This difference in the symmetry of the spatial parts causes an energy difference between singlet and triplet states, which explains why the Coloumb interaction has to be taken into account in the spin Hamiltonian. For RPs the exchange interaction is very weak (>10^{-7}eV) and it is sufficient to consider only the isotropic part of $\boldsymbol{J}$. This results in the isotropic exchange Hamiltonian :

$$\widehat{\mathcal{H}}_{iso} = -2 J \widehat{\boldsymbol{S}}_1 \widehat{\boldsymbol{S}}_2 \;\; With \quad J = \frac{1}{3} tr(\boldsymbol{J}) \qquad (2.14)$$

J is the isotropic electron-exchange coupling constant, and $2J$ is the energy difference between the singlet and triplet states when the Zeeman interaction and the dipolar interaction, which will be explained in next section, are absent or can be ignored to a first approximation. The strength of the exchange interaction decays exponentially as the distance between two electrons increases. [62, 77 and 83].

2.3.2 Electron-Electron Dipolar Interaction

The dipolar interaction is the interaction of the magnetic dipole moments of two electrons with each other. This anisotropic interaction removes the three-fold degeneracy of the triplet state even in the absence of the static magnetic field. This effect is sometimes called zero-field splitting. Spin-orbit coupling also contributes to the lifting of the degeneracy of triplet levels. However, for RPs and molecular triplet states its contribution is negligible. The Hamiltonian for the dipolar interaction is derived from the classical electromagnetic interaction of the two dipole moments separated by a distance *r* [78]:

$$\widehat{\mathcal{H}}_D(r) = \frac{\mu_0}{4\pi}\left[\frac{\widehat{\boldsymbol{\mu}}_1^T.\,\widehat{\boldsymbol{\mu}}_2}{r^3} - \frac{3\left(\widehat{\boldsymbol{\mu}}_1^T.\boldsymbol{r}\right)\left(\widehat{\boldsymbol{\mu}}_2^T.\boldsymbol{r}\right)}{r^5}\right] \tag{2.15}$$

If we consider the two electron spins as point dipoles, for the magnetic moments of each spin and considering the fact that the anisotropy in $\boldsymbol{g}$ is small for organic radicals [78], we have :

$$\widehat{\boldsymbol{\mu}}_i = \bar{V}\beta g_i \widehat{\boldsymbol{S}}_{\boldsymbol{i}} \tag{2.16}$$

Then eqn. (2.16) becomes:

$$\widehat{\mathcal{H}}_D(r) = \frac{\mu_0}{4\pi} g_1 g_2 \beta^2 \left[\frac{\widehat{\boldsymbol{S}}_{\boldsymbol{1}}^T.\,\widehat{\boldsymbol{S}}_{\boldsymbol{2}}}{r^3} - \frac{3\left(\widehat{\boldsymbol{S}}_{\boldsymbol{1}}^T.\boldsymbol{r}\right)\left(\widehat{\boldsymbol{S}}_{\boldsymbol{2}}^T.\boldsymbol{r}\right)}{r^5}\right] \tag{2.17}$$

By expanding the vector multiplications in this eqn and collecting terms, it will take the following form:

$$\widehat{\mathcal{H}}_D = 2\widehat{\boldsymbol{S}}_{\boldsymbol{1}}^T \boldsymbol{D} \widehat{\boldsymbol{S}}_{\boldsymbol{2}} = \widehat{\boldsymbol{S}}^T \boldsymbol{D}\, \widehat{\boldsymbol{S}} \tag{2.18}$$

Where $\widehat{\boldsymbol{S}} = \widehat{\boldsymbol{S}}_{\boldsymbol{1}} + \widehat{\boldsymbol{S}}_{\boldsymbol{2}}$ and $\boldsymbol{D}$ is a 3*3 matrix representing the anisotropy of the dipolar interaction:

$$\boldsymbol{D} = \frac{\mu_0}{8\pi} g_1 g_2 \beta^2 \begin{pmatrix} \langle \frac{r^2 - 3x^2}{r^5} \rangle & \langle \frac{-3xy}{r^5} \rangle & \langle \frac{-3xz}{r^5} \rangle \\ \langle \frac{-3xy}{r^5} \rangle & \langle \frac{r^2 - 3y^2}{r^5} \rangle & \langle \frac{-3yz}{r^5} \rangle \\ \langle \frac{-3xz}{r^5} \rangle & \langle \frac{-3yz}{r^5} \rangle & \langle \frac{r^2 - 3z^2}{r^5} \rangle \end{pmatrix} \tag{2.20}$$

$\boldsymbol{D}$ is a traceless matrix, that can be diagonalized and represented by its principal elements D_{xx}, D_{yy} and D_{zz} (see chapter 6 of reference [78]). Because it is traceless the principal elements can be expressed in terms of two parameters, D and E, which are often called the zero-field parameters. In terms of D and E, $\boldsymbol{D}$ is [78]:

$$\boldsymbol{D} = \begin{pmatrix} -\frac{1}{3}D - E & 0 & 0 \\ 0 & -\frac{1}{3}D + E & 0 \\ 0 & 0 & \frac{2}{3}D \end{pmatrix} \tag{2.21}$$

If the system has 3-fold or higher rotational symmetry (axial symmetry), E in the eqn. (2.21) becomes zero, therefore **D** reduces to:

$$\boldsymbol{D} = \begin{pmatrix} -\frac{1}{3}D & 0 & 0 \\ 0 & -\frac{1}{3}D & 0 \\ 0 & 0 & \frac{2}{3}D \end{pmatrix} \tag{2.22}$$

From eqn. (2.20), it is apparent that the elements of $\boldsymbol{D}$ depend on the distance, r, between the two magnetic moments. To simplify the relation between D and r, we assume that both g-factors are equal to free-electron g value. Then if the spins are far enough that their spatial distribution can be ignored and they can be treated as point dipoles. Then D becomes [78]:

$$D = -\frac{3g_e\beta\mu_0}{8\pi}\frac{1}{r^3} \approx -\frac{2786}{r^3} mT\text{Å}^3 \qquad (2.23)$$

The effect of the direction of the magnetic field on the magnitude of dipolar coupling, can be expressed by:

$$d = \boldsymbol{n}^T \boldsymbol{D}\boldsymbol{n} = \frac{1}{3}D(3cos^2\theta - 1) \qquad (2.24)$$

where $\boldsymbol{n}$ is a unit vector in the direction of the magnetic field and θ is the angle between $\boldsymbol{n}$ and the distance vector, r between the two spins. If the value of d can be measured, the distance between the two electrons and the direction of distance vector in the external static magnetic field can be determined. Finally if we combine eqns (2.24) and (2.19) we find the final eqn. for the dipolar interaction contribution in the spin Hamiltonian for two unpaired electrons:

$$\widehat{\mathcal{H}}_D = \frac{3}{3cos^2\theta - 1}\text{d}\,(\widehat{\boldsymbol{S}}_z^2 - \widehat{\boldsymbol{S}}^2) \qquad (2.25)$$

If the magnetic field and the dipolar coupling are parallel eqn. (2.25) becomes:

$$\widehat{\mathcal{H}}_D = \frac{3}{2}\text{d}\,(\widehat{\boldsymbol{S}}_z^2 - \widehat{\boldsymbol{S}}^2) \qquad (2.26)$$

2.4 Hyperfine Interaction

Many nuclei possess spin angular momentum like electrons, which arises from the summation over the spins of the neutrons and protons. If this summation is nonzero the nucleus has a magnetic dipole moment that can interact with the magnetic dipole moment of an unpaired electron. The interaction between an electron with surrounding nuclei has isotropic and anisotropic parts. The isotropic hyperfine interaction arises from the fact that electrons in s orbitals have nonzero electron density ($|\psi(0)|^2$) at the nucleus. Fermi has shown that for

systems with one unpaired electron the isotropic magnetic coupling is given approximately by [78]:

$$A_{iso} = \frac{2}{3}\mu_0\beta_N\,\beta\,g_N\,g\,|\psi(0)|^2 \qquad (2.27)$$

Here "N" denotes nucleus. The anisotropic hyperfine coupling arises from the magnetic dipole interaction of electron with a neighboring nucleus, therefore it can be treated like the dipolar interaction between two electrons (eqn. (2.18)). Hence, the hyperfine contribution for the spin Hamiltonian would have the following form:

$$\widehat{\mathcal{H}}_{hf} = \widehat{\boldsymbol{S}}^{\boldsymbol{T}} A\,\widehat{\boldsymbol{I}} = \widehat{\boldsymbol{S}}^{\boldsymbol{T}} A'\widehat{\boldsymbol{I}} + A_{iso}\widehat{\boldsymbol{S}}^{\boldsymbol{T}}\widehat{\boldsymbol{I}} \qquad (2.28)$$

Here, the nuclear and electron spins are indicated by **I** and **S** respectively and A' is the anisotropic coupling**.** The effect of the interaction between an electron with a nucleus is to split the energy levels of both the electron and the nucleus. In general, if there are m non-equivalent sets of n equivalent nuclei, the number of spin energy levels of the electron is: $2\prod_{i=1}^{m}(2n_iI_i+1)$, and the number of lines in the EPR spectrum, is $\prod_{i=1}^{m}(2n_iI_i+1)$ [78]. Coupling to a large nuclei results in a Gaussian lineshape [77, 81].

2.5 Relaxation Process in EPR Spectroscopy

Another factor that affects EPR spectra is spin relaxation. At thermal equilibrium the ratio of the populations of the two spin states is given by the Boltzmann distribution [78]:

$$\frac{N_+}{N_-} = exp(-\frac{\Delta E}{kT}) \qquad (2.29)$$

where, N_+ and N_- indicate the number of electron in each state of $|+>$ or $|->$, and $N = N_+ + N_-$ is the number of unpaired electrons in the system, k is the Boltzmann constant, T is the temperature and ΔE is the energy difference between the two states. As can be noticed in eqn. (2.29), lowering the temperature will lead to an increase in the population difference and hence the amplitude of the EPR signal. When the spin system is brought out of equilibrium by a microwave pulse, the population difference is disturbed, but after a while the spin system tends to recover to its stable state. Relaxation times describe this recovery of the spin system to equilibrium in magnetic resonance experiments. There are two types of relaxation, spin-lattice relaxation and spin-spin relaxation. In the first case, the energy is dissipated within the lattice as phonons, in the form of vibration, rotational and translational energy. The time constant of the exponential decay function that describes the restoration of the energy of spin system is called T_1. However, in addition to exchanging energy with the surroundings, there can be an energy exchange between the spins without transfer of energy to the lattice. This exchange leads to the loss of phase coherence and is known as spin-spin relaxation [85]. The decay constant associated with this process is T_2. The effects of the spin-lattice and spin-spin relaxation make the lifetime of the spin states and the EPR signal shorter, which leads to homogenous line broadening of the spectra with a Lorentzian line-shape with a line width which is proportional to $\frac{1}{T_1} + \frac{1}{T_2}$ [78]. By increasing theses two relaxation times, we have more time to detect the EPR signal and homogeneous line broadenting is reduced. Because T_1 is inversely proportional to the temperature [62, 84], this can be achieved by lowering the temperature. In fact, that is the reason why most of the EPR experiments, are performed at cryogenic temperature[3] [86].

In the next chapter, we use the concepts introduced in this chapter to construct the basic Hamiltonian for the two electron spin system generated in PS I RCs

[3] Organic radicals typically have the longest relaxation times among the paramagnetic species. Transition metals and triplet states usually relax more rapidly.

and heliobacterial RCs to explain the required theory to analyze spin polarized EPR spectra represented in this thesis.

3 Theory of Spin Correlated Radical Pairs

Following light excitation, a series of sequential RPs are generated in the *Hb*RCs and PS I RCs. The initial RP is generated on a picosecond time scale which is very fast compared to the time scale of the interactions within the RP, so it can be inferred that the first RP is formed in a pure singlet state [16]. The subsequent ET steps generate a series of spin correlated RPs, which can be studied by Time-Resolved EPR (TR-EPR) techniques [48,86]. To study the behavior of these RPs by TR-EPR techniques, we need to know the associated Hamiltonian to derive the eigenstates, eigenvalues, transition probabilities between states and population differences for such a spin system.

3.1 Eigenvalues and Eigenfunctions of the Two Electron Spin System in a Static Magnetic Field

The following interactions need to be included in the Hamiltonian ($\widehat{\mathcal{H}}_0$) for the two-spin system in the presence of an external magnetic field:

1. The Zeeman interaction of each electron with the external magnetic field $\widehat{\mathcal{H}}_{eZ1} + \widehat{\mathcal{H}}_{eZ2}$,
2. The hyperfine interaction between each electron and surrounding nuclei, $\widehat{\mathcal{H}}_{hf}$,
3. The spin-spin interactions between the two electrons, $\widehat{\mathcal{H}}_{SS} = \widehat{\mathcal{H}}_{D} + \widehat{\mathcal{H}}_{iso}$.

So the Hamiltonian has the following form:

$$\widehat{\mathcal{H}}_0 = \widehat{\mathcal{H}}_{eZ1} + \widehat{\mathcal{H}}_{eZ2} + \widehat{\mathcal{H}}_{hf} + \widehat{\mathcal{H}}_{SS} \tag{3.1}$$

For convenience in treating the EPR experiments, the Hamiltonian is transformed into a reference frame rotating at MW frequency. The effect of the microwave (MW) field applied in the *xy* plane with frequency ω_1 can be described by the Hamiltonian $\widehat{\mathcal{H}_1} = \omega_1(\widehat{\boldsymbol{S}}_{1x} + \widehat{\boldsymbol{S}}_{2x})$ [78]. Moreover, if the high-field approximation is applied, which means all the interaction are small compared to Zeeman interaction, the Hamiltonian can be expressed as follows [88]:

$$\begin{aligned}\widehat{\mathcal{H}}_0 = (g_1\beta B_0/\hbar - \omega_{MW})\widehat{\boldsymbol{S}}_{1Z} + (g_2\beta B_0/\hbar - \omega_{MW})\widehat{\boldsymbol{S}}_{2Z} \\ + \sum_{i,j} A_{ij}\widehat{\boldsymbol{S}}_{iZ}\widehat{\boldsymbol{I}}_{jZ} + \frac{3}{2}d(\widehat{\boldsymbol{S}}_z^2 - \widehat{\boldsymbol{S}}^2) - 2J\widehat{\boldsymbol{S}}_{\boldsymbol{1}}\widehat{\boldsymbol{S}}_{\boldsymbol{2}}\end{aligned} \tag{3.2}$$

Here g_1 and g_2 are the two effective g-values of the electron spin for a given orientation of the RP with respect to the external field, d is the effective dipolar coupling along the external magnetic field axis, J is the exchange interaction. The effective hyperfine coupling constant between electron i and nucleus j is given by A_{ij}. In the eqn. (3.2) and all of the following equations the energies are expressed in frequency units. The matrix representation of the Hamiltonian in the singlet-triplet basis is [88]:

$$\widehat{\mathcal{H}}_0 = \begin{array}{c} \begin{matrix} |T_+> & |S> & |T_0> & |T_-> \end{matrix} \\ \begin{pmatrix} \omega_0 - \frac{J}{2} + \frac{d}{2} & 0 & 0 & 0 \\ 0 & 3\frac{J}{2} & \Delta\omega & 0 \\ 0 & \Delta\omega & -\frac{J}{2} + d & 0 \\ 0 & 0 & 0 & \omega_0 - \frac{J}{2} + \frac{d}{2} \end{pmatrix} \end{array} \tag{3.3}$$

in which:

$$\begin{aligned} \omega_0 &= \frac{1}{2\hbar}\beta B_0(g_1 + g_2) + \frac{1}{2\hbar}\sum_j (A_{1j} + A_{2j})m_j \\ \Delta\omega &= \frac{1}{2\hbar}\beta B_0(g_1 - g_2)) + \frac{1}{2\hbar}\sum_j (A_{1j} - A_{2j})m_j \end{aligned} \tag{3.4}$$

m_j denotes the magnetic quantum number of nucleus j.

The eigenvalues and eigenvectors of the Hamiltonian are:

$$\begin{aligned} E_1 &= \omega_0 - \frac{(J-d)}{2} & |1> &= |T_+> \\ E_2 &= \Omega + \frac{(J-d)}{2} & |2> &= \cos\alpha|S> + \sin\alpha|T_0> \\ E_3 &= -\Omega + \frac{(J-d)}{2} & |3> &= -\sin\alpha|S> + \cos\alpha|T_0> \\ E_4 &= \omega_0 - \frac{(J-d)}{2} & |4> &= |T_-> \end{aligned} \tag{3.5}$$

Where Ω and α which are known as the singlet-triplet mixing frequency and singlet-triplet mixing angle α respectively, and are defined by:

$$\Omega^2 = \Delta\omega^2 + (\mathrm{J} + \mathrm{d}/2)^2$$
$$\sin(2\alpha) = \frac{\Delta\omega}{\Omega}\ ;\ \cos(2\alpha) = \frac{\mathrm{J} + \mathrm{d}/2}{\Omega} \qquad (3.6)$$

Thus, we obtain four energy levels, two of which are pure triplet states and two that are a mixture of singlet and triplet. Based on the selection rule for magnetic dipole transitions $\Delta m_s = \pm 1$ there are four allowed transitions, which are depicted in Figure 3.1, The initial RP is generated in a pure singlet state, which is not an eigenstate of the system and is a coherent superposition of levels */2>* and */3>.* Thus, initially the system oscillates between $|S>$ and $|T_0>$ states. However, this coherence decays rapidly leaving the four eigenstates populated according to their singlet character, *i.e.* only the two middle levels */2>* and */3>* populated.

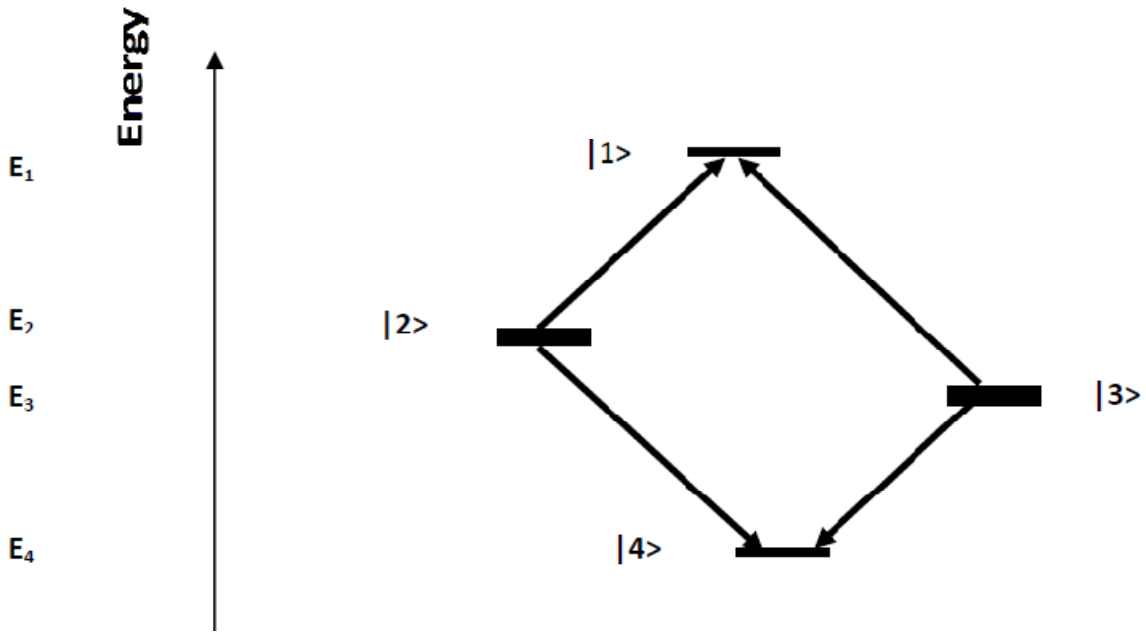

Figure 3.1: Energy Scheme for a coupled two electrons system. The arrow marks the allowed single quantum transitions between the energy levels. The states that are populated after decay of the initial coherence are indicated by bold bars. So, the thickness of the line for each energy level is meant to represent its relative population.

The singlet state is diamagnetic, so the initial state of the RP cannot be detected by EPR spectroscopy, but as it evolves under the Zeeman, hf, and spin-spin

interactions it acquires triplet character and can be detected. Although, the lifetime of the first RP is too short to be directly observed, its spin dynamics must be taken into account when describing the more stable RPs generated afterwards. The fact that only two of the eigenstates of the system contain singlet character means that the populations of the energy levels of the RPs are far from thermal equilibrium. This effect is known as Electron Spin Polarization ESP (for a review see [59, 60, 88]). In spin polarized EPR spectra, some transitions appear as emission (E) and others as absorption (A). The ESP pattern for an RP, which is long-lived enough to be directly observed, depends not only on its geometry, environment and magnetic properties, but also on the spin dynamics of its precursor RPs [61]. To describe the ESP pattern in a more convenient way and also describe the spin dynamics of a coupled spin system, which cannot be easily described by a vector picture, the density operator formalism has been used for studying the RP spin dynamics.

3.2 Density Operator Formalism to Study the Spin Dynamics of the RPs

For an ensemble of isolated spins $S=1/2$, a single spin is in a general superposition state:

$$|\psi> = c_+|+> + c_-|-> \quad \text{or} \quad |\psi> = \begin{pmatrix} c_+ \\ c_- \end{pmatrix} \tag{3.7}$$

which means the expectation value of an operator $\hat{Q}$:

$$<\hat{Q}> = <\psi|\hat{Q}|\psi> = (c_+^* \quad c_-^*)\begin{pmatrix} Q_{++} & Q_{+-} \\ Q_{+-} & Q_{--} \end{pmatrix}\begin{pmatrix} c_+ \\ c_- \end{pmatrix} \tag{3.8}$$

Which is equal to $c_+^* c_+ Q_{++} + c_+^* c_- Q_{+-} + c_+ c_-^* Q_{-+} + c_- c_-^* Q_{--}$, a quadratic product of c_+ and c_- has the following form:

$$|\psi><\psi| = \begin{pmatrix} c_+ \\ c_- \end{pmatrix} (c_+^* \quad c_-^*) = \begin{pmatrix} c_+^* c_+ & c_+ c_-^* \\ c_+^* c_- & c_- c_-^* \end{pmatrix} \tag{3.9}$$

By comparing (3.8) and (3.9) we find that:

$$< \hat{Q} > = Tr\{|\psi><\psi|\hat{Q}\} \tag{3.10}$$

This approach becomes useful if many independent spins are involved. The ensemble average then becomes (with the assumption that the wavefunctions are normalized):

$$\hat{\boldsymbol{\rho}} = (|\psi_1><\psi_1| + \cdots |\psi_N><\psi_N|) = \overline{|\psi><\psi|} \tag{3.11}$$

which is known as the density operator. Therefore, we can define the expectation value of any operator $\hat{Q}$ as:

$$< \hat{\boldsymbol{Q}} > = Tr\{\hat{\boldsymbol{\rho}}\hat{\boldsymbol{Q}}\} \tag{3.12}$$

The diagonal elements of the density operator are the populations of states $|+>$ and $|->$ and the off-diagonal elements are called coherences. A coherence between two energy eigenstates $|r>$ and $|s>$ defined as:

$$\rho_{rs} =< r|\hat{\rho}|s > =< r|\psi><\psi|s > \tag{3.13}$$

Hence, at any time if the density operator of the system is known, any observable of the system, like the macroscopic magnetization in our case, can be

derived by calculating the trace of the product of density matrix and the related observable. If we study a system, which evolves with time, we need to calculate the time evolution of the density operator to derive the expectation value of the operator of interest.

3.3 Time Evolution of the Density Operator

The time evolution of the system is derived from the time-dependent Schrödinger eqn:

$$\frac{\partial \hat{\boldsymbol{\rho}}}{\partial t} = i\left[\hat{\boldsymbol{\rho}}, \hat{\mathcal{H}}_{\mathbf{0}}\right] \tag{3.14}$$

which is known as Liouville equation [90]. The general equation for time evolution of density matrix under a time-independent Hamiltonian $\widehat{\boldsymbol{\mathcal{H}}}_0$ can be derived by integration of the Liouville equation. over time:

$$\hat{\boldsymbol{\rho}}(t) = \exp\left(-i\,\hat{\mathcal{H}}_0\,t\right)\hat{\rho}(0)\exp\left(i\,\hat{\mathcal{H}}_0\,t\right) \tag{3.15}$$

Since the RPs under study are generated in a singlet state by a laser flash, the initial density matrix in the singlet-triplet basis is given by [88]:

$$\hat{\boldsymbol{\rho}}(0) = \begin{array}{c} \begin{matrix} /T_+> & /S> & /T_0> & /T_-> \end{matrix} \\ \begin{pmatrix} 0 & 0 & 0 & 0 \\ 0 & 1 & 0 & 0 \\ 0 & 0 & 0 & 0 \\ 0 & 0 & 0 & 0 \end{pmatrix} \end{array} \tag{3.16}$$

The time evolution of $\hat{\boldsymbol{\rho}}(0)$in the singlet-triplet representation is given by [88]:

$$\widehat{\boldsymbol{\rho}}(t) = \begin{array}{c} \begin{matrix} /T_+> & /S> & /T_0> & /T_-> \end{matrix} \\ \begin{pmatrix} 0 & 0 & 0 & 0 \\ 0 & 1-\sin^2 2\alpha \sin^2 \Omega t & \rho_{23} & 0 \\ 0 & \rho_{32} & \sin^2 2\alpha \sin^2 \Omega t & 0 \\ 0 & 0 & 0 & 0 \end{pmatrix} \end{array} \qquad (3.17)$$

Where:

$$\rho_{23} = {\rho_{32}}^{*} = \sin 2\alpha \cos 2\alpha \ \sin^2 \Omega t - \frac{i}{2} \sin 2\alpha \sin 2\Omega t \qquad (3.18)$$

$\widehat{\boldsymbol{\rho}}(t)$ can be transformed to the eigenbasis of the Hamiltonian using a unitary transformation **U** used for diagonalization of the Hamiltonian:

$$\mathbf{U} = \begin{pmatrix} 1 & 0 & 0 & 0 \\ 0 & \cos\alpha & \sin\alpha & 0 \\ 0 & -\sin\alpha & \cos\alpha & 0 \\ 0 & 0 & 0 & 1 \end{pmatrix} \qquad (3.19)$$

Then this unitary matrix is applied in the following eqn.:

$$\widehat{\boldsymbol{\rho}}(t) = \mathbf{U}^{\mathrm{T}} \exp\left(-i\, \widehat{\mathcal{H}}_0^{diag} t\right) \mathbf{U}\, \hat{\rho}(0) \mathbf{U}^{\mathrm{T}} \exp\left(i\, \widehat{\mathcal{H}}_0^{diag} t\right) \mathbf{U} \qquad (3.20)$$

to give the time-dependent density matrix in the eigenbasis of $\widehat{\mathcal{H}}_0$:

$$\widehat{\boldsymbol{\rho}}(t) = \mathbf{U}^{\mathrm{T}} \begin{pmatrix} /1> & /2> & /3> & /4> \\ 0 & 0 & 0 & 0 \\ 0 & cos^2\alpha & -\sin\alpha\ \cos\alpha\, e^{-2i\Omega t} & 0 \\ 0 & -\sin\alpha\ \cos\alpha\, e^{+2i\Omega t} & \sin^2\alpha & 0 \\ 0 & 0 & 0 & 0 \end{pmatrix} \mathbf{U} \qquad (3.21)$$

As can be seen from eqns (3.17) and (3.21) the density matrix is different from the density matrix for thermal equilibrium, which is [90]:

$$\widehat{\boldsymbol{\rho}} = -\widehat{\boldsymbol{S}}_{\boldsymbol{z}} = -(\,\widehat{\boldsymbol{S}}_{\mathbf{1z}} + \widehat{\boldsymbol{S}}_{\mathbf{2z}}\,) \qquad (3.22)$$

On the other hand eqns (3.17) and (3.21) can be rewritten for t=0 as :

$$\widehat{\boldsymbol{\rho}} = \left(\frac{1}{4}\mathbb{I} - \widehat{\boldsymbol{S}}_{\mathbf{1z}}\widehat{\boldsymbol{S}}_{\mathbf{2z}}\right) + \frac{1}{2}cos2\alpha\,\left(\widehat{\boldsymbol{S}}_{\mathbf{1z}} - \widehat{\boldsymbol{S}}_{\mathbf{2z}}\right) - sin2\alpha\,\left(\widehat{\boldsymbol{S}}_{\mathbf{1x}}\widehat{\boldsymbol{S}}_{\mathbf{2x}} + \widehat{\boldsymbol{S}}_{\mathbf{1y}}\widehat{\boldsymbol{S}}_{\mathbf{2y}}\right) \qquad (3.23)$$

Compared to thermal equilibrium, the populations have been changed, and two off-diagonal elements have appeared. The off-diagonal elements oscillate with frequency (2Ω) which is the energy difference between states */2>* and */3>* in the Figure 3.1 and is known as the "zero-quantum coherence frequency" or "quantum beat frequency" [91], [92], Moreover, from eqn. (3.17) it is apparent that the population in the sublevels of */S>* and */T>* also oscillate with this frequency. Because the EPR transition intensities depend on the triplet characters of the mixed states */2>* and */3>*, as the system oscillates between */S>* and */T_0>*, the EPR signal intensity oscillates, and this oscillation is observable experimentally ([93], [94]) but decays rapidly due to destructive interference of the many frequencies present. Hence it does not have a significant effect on the time-resolved EPR (TREPR) spectra of singlet-born RPs measured at times longer than ~100 ns [60, 61]. However, it is important

because the initial zero-quantum coherence is the main mechanism by which additional spin polarization is generated in the subsequent RPs. For the primary radical pair, at times > 100 ns, all the terms in the eqns (3.17) and (3.21) containing zero-quantum coherence can be substituted by their average:

$$\sin^2\Omega t \to \frac{1}{2}, \qquad e^{\pm 2i\Omega t} \to 0, \qquad \sin 2\Omega t \to 0 \tag{3.24}$$

With these approximations the density matrix then is given by:

$$\widehat{\boldsymbol{\rho}}(t) = \begin{array}{c} \begin{matrix} /T_+> & /S> & /T_0> & /T_-> \end{matrix} \\ \begin{pmatrix} 0 & 0 & 0 & 0 \\ 0 & 1-\frac{1}{2}\sin^2 2\alpha & \frac{1}{2}\sin 2\alpha\cos 2\alpha & 0 \\ 0 & \frac{1}{2}\sin 2\alpha\cos 2\alpha & \frac{1}{2}\sin^2 2\alpha & 0 \\ 0 & 0 & 0 & 0 \end{pmatrix} \end{array} = \tag{3.25}$$

$$\begin{array}{c} \begin{matrix} /1> & /2> & /3> & /4> \end{matrix} \\ \mathbf{U^T} \begin{pmatrix} 0 & 0 & 0 & 0 \\ 0 & \cos^2\alpha & 0 & 0 \\ 0 & 0 & \sin^2\alpha & 0 \\ 0 & 0 & 0 & 0 \end{pmatrix} \mathbf{U} \end{array}$$

In this form it is apparent that the diagonal elements of the density matrix, which are populations, are the singlet characters ($|S>$) of the states. Therefore the populations n_i can be defined as follow:

$$n_i = \rho_{ii} = |<S|i>|^2 \tag{3.26}$$

In the next section, the dependence of the EPR signal on the population difference and its intensity will be discussed.

3.4 Transition Between States and EPR Signal Intensity

The EPR signal depends on the transitions between the eigenstates. The frequencies of the four single quantum transitions can be derived based on eqn. (3.6):

$$\begin{aligned} \omega_{12} &= E_1 - E_2 = \omega_0 - (J - d) - \Omega \\ \omega_{34} &= E_3 - E_4 = \omega_0 + (J - d) - \Omega \\ \omega_{13} &= E_1 - E_3 = \omega_0 - (J - d) - \Omega \\ \omega_{24} &= E_2 - E_4 = \omega_0 + (J - d) - \Omega \end{aligned} \tag{3.27}$$

The effect of the MW source, which by convention is considered to be polarized along the *x*-axis is given by the operator:

$$\widehat{\mathcal{H}_1} = \frac{g\beta B_1}{\hbar}\hat{\boldsymbol{S}}_x = \frac{g\beta B_1}{\hbar}\left(\hat{\boldsymbol{S}}_{1x} + \hat{\boldsymbol{S}}_{2x}\right) \tag{3.28}$$

whereB_1 is the strength of the magnetic field component of the MW source.
Then the transition moment between states i and j is:

$$p_{ij} = \left| < i|\widehat{\mathcal{H}_1}|j > \right|^2 \tag{3.29}$$

The intensity of the EPR signal is proportional to the transition moment times the population difference:

$$I_{ij} \propto -\Delta n_{ij} p_{ij} \tag{3.30}$$

where $\Delta n_{ij} = n_i - n_j$ and i refers to the state of higher energy. One can calculate the transition probabilities and the population differences corresponding to the transition frequencies given in eqn. (3.27). Using the wavefunctions given in eqn. (3.6) and eqns (3.29) and (3.26) one obtains:

$$
\begin{aligned}
p_{12} &= \tfrac{1}{2}\sin^2\alpha, & -\Delta n_{12} &= \cos^2\alpha \\
p_{34} &= \tfrac{1}{2}\cos^2\alpha, & -\Delta n_{34} &= -\sin^2\alpha \\
p_{13} &= \tfrac{1}{2}\cos^2\alpha, & -\Delta n_{13} &= \sin^2\alpha \\
p_{24} &= \tfrac{1}{2}\sin^2\alpha, & -\Delta n_{24} &= -\cos^2\alpha
\end{aligned}
\tag{3.31}
$$

Thus, the absolute value of the signal intensity for all four transitions based on eqn. (3.27) is proportional to:

$$
|I_{ij}| \propto \tfrac{1}{2}\sin^2\alpha\cos^2\alpha = \tfrac{1}{8}\tfrac{\Delta\omega^2}{\Omega^2} \tag{3.32}
$$

If we insert the sign of each intensity, two of the transitions are absorptions and the other two emissions. In Figure 3.2, the stick spectrum corresponding to these four transitions is shown. In this figure, two of the lines are transitions associated primarily with the donor and two are from the acceptor. The separation between the two pairs of lines is due to the difference in the g-values of the donor and acceptor, In the case of $\Delta\Omega \gg J + \frac{d}{2}$ the difference in the resonance frequencies of the donor and acceptor is approximately equal to the zero-quantum coherence frequency. As can be seen in Figure 3.2, the two transitions for each spin are centered at $\omega_0 + \omega_{MW}$ and the separation between them is given by $2(J-d)$. Here, we see that the polarization pattern not only depends on the signs of exchange and dipolar coupling but also on the angle between the magnetic field and the dipolar coupling vector (θ) (see eqns (2.15), (2.23), (2.24) and (3.6)). As can be seen from eqn. (2.23), the effective dipolar coupling constant is negative for two weakly interacting electron spins. In the Figure (3.2), $2(J-d)$ is assumed to be positive and thus, if J can be neglected the orientation $\theta < 54.7^\circ$ (magic angle) can be deduced from the sign of the polarization. On the other hand, if $\theta > 54.7^\circ$ then $d > 0$, and the polarization

pattern for the RP would change to A/E/A/E. And of course, for $\theta = 54.7°, d = 0$, the two lines for each spin cancel out each other and there would be no polarization pattern.

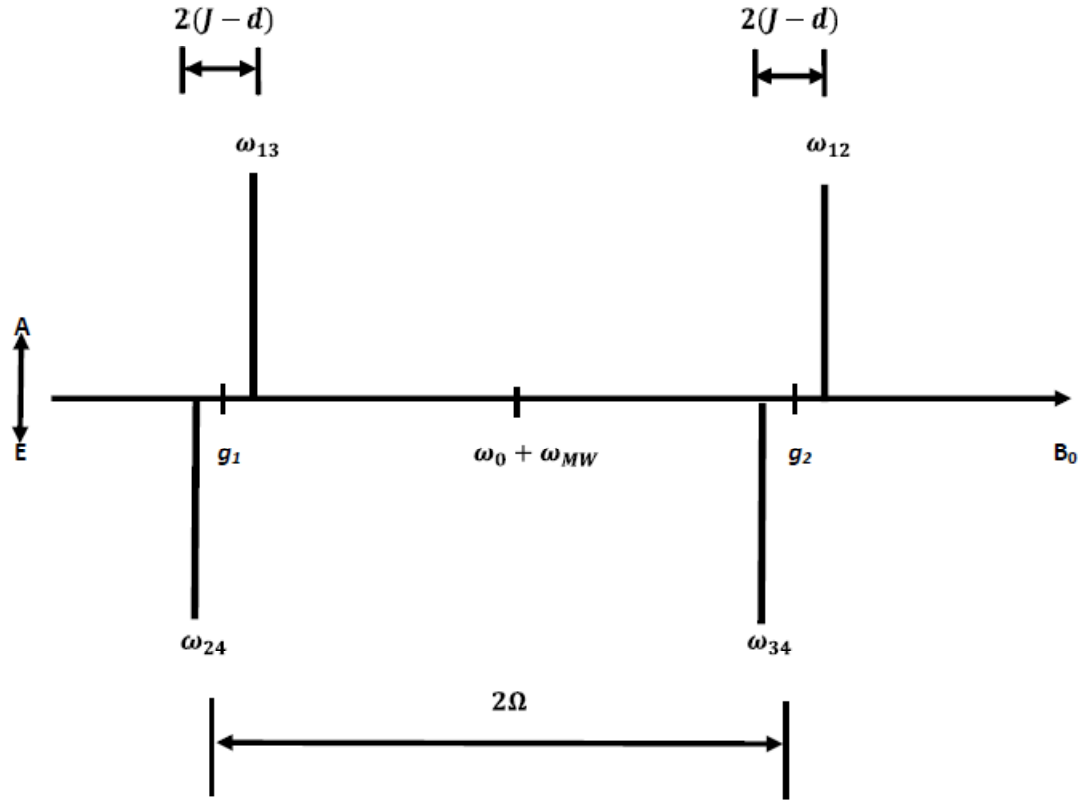

Figure 3.2: Stick spectrum for an RP generated from a singlet precursor. All parameters are in frequency unit.

In the stick spectrum shown in Figure 3.2 the hyperfine coupling has not been taken into account. As mentioned in the previous chapter, coupling to many nuclei leads to a Gaussian lineshape. The effect of hyperfine coupling is inhomogeneous broadening of EPR spectra. The lineshape in the presence of inhomogeneous broadening has been studied previously [57,59], and in the case where the linewidth associated with each radical D_1 and D_2 is greater than the exchange coupling, J and dipolar coupling, D the signal intensity was calculated as:

$$I = (D\left(cos^2\theta - \frac{1}{3}\right) - J)\left[\frac{\Delta\omega_1}{\sqrt{2}D_1^3}\exp\{-\frac{\Delta\omega_1^2}{2D_1^2}\} + \frac{\Delta\omega_2}{\sqrt{2}D_2^3}\exp\{-\frac{\Delta\omega_2^2}{2D_2^2}\}\right] \quad (3.33)$$

Here,

$$\Delta\omega_i = \omega_i - \omega_{MW} + \delta_i \quad (3.34)$$

In eqn. (3.34) i, refers to each radical (1 and 2), and δ_i refers to the shift of the resonance frequency of the unpaired electron of the radical i. Therefore, the splitting of the doublets around the g-value of each radical is no longer determined by spin-spin coupling, but instead by the Gaussian linewidth. On the other hand, the intensity of the signal is a linear function of the spin-spin couplings [62]. For a disordered sample, the EPR spectrum is the sum of spectra of all possible orientations of the RP relative to the external field. Such a spectrum is known as powder pattern. For a weakly coupled, singlet-born RP, the spin polarized powder pattern is sensitive to the orientation of the dipolar coupling axis relative to principal axes of the g-tensor of each radical. As discussed in [59, 61], the linear dependence of the signal on the spin-spin coupling and the fact that exchange interaction is small compared to dipolar coupling in the PS I and *Hb*RCs allows the integration over all orientation of the RPs to be written as the sum of four integrals:

$$I_{exp} = \kappa_{1,z} < I_{1,z} > + \kappa_{1,\Delta} < I_{1,\Delta} > \kappa_{2,z} < I_{2,z} > + \kappa_{1,\Delta} < I_{1,\Delta} > \quad (3.35)$$

The terms in the brackets are four powder spectra that are independent of the internal geometry of the RP and brackets indicate the summation over all orientations relative to the external field. The factors $\kappa_{1,z}$, etc. are weighting factors that depend on the internal geometry for each radical and are given by [62]:

$$\kappa_{1,z} = -\frac{1}{2}\,\varepsilon D\left(\cos^2\theta_1 - \frac{1}{3}\right)$$

$$\kappa_{1,\Delta} = -\frac{1}{2}\,\varepsilon D\,\sin^2\theta_1\cos 2\varphi_1$$

$$\kappa_{2,z} = -\frac{1}{2}\,\varepsilon D\,(\cos^2\theta_2 - \frac{1}{3}) \qquad (3.36)$$

$$\kappa_{2,\Delta} = -\frac{1}{2}\,\varepsilon D\,\sin^2\theta_2\cos 2\varphi_2$$

Because the EPR signal cannot be easily calibrated to give absolute intensities, a parameter ε is introduced as an arbitrary scaling factor to normalize the simulation amplitude to the experimental one. The main problem to make expressions in eqn. (3.36) applicable in simulating and fitting the EPR spectra for the photosynthetic RPs, is that the sign of the cosine expressions cannot be determined, and that causes eight fold ambiguity in the geometry related to the placement of orientation of the dipolar coupling in eight quadrants of a sphere. These ambiguities combined with scaling factor ε put the number of unknown numbers greater than the number of adjustable parameters. Hence, there is no unique set of angles that describe the experimental spectra [62]. Instead of a unique geometry, a function of the angles θ and φ describe a set of possible angles. The geometry for the RPs in PS I is known from the X-ray structure [40], but some uncertainty about the orientation of the g-tensor axes in P_{700} still remains.

As mentioned, a series of sequential RPs occurs in the photosynthetic RCs. Hence, the evolution of the spin polarization during the ET is important. In the next chapter, the time-resolved EPR techniques that are employed for monitoring the spin polarization and its properties in sequential RPs will be introduced.

4 Time-Resolved EPR and its Application in Studying Electron Transfer in PS I and Heliobacterial Reaction Centers

Time-Resolved EPR methods have been employed extensively to study the geometries, local environments and lifetimes of the light-induced RPs in photosynthetic RCs. These methods fall into two categories: Pulsed EPR and Transient EPR.

4.1 Transient EPR: Experimental Spectra

In a transient EPR experiment, in the presence of continuous microwave irradiation and a static magnetic field the sample is irradiated by a short laser pulse, which generates one or more paramagnetic species such as the RPs in photosynthetic RCs. The light-induced signal is then detected as a function of time after the laser pulse. The time trace is stored, the field is set to a new value and another time trace is collected. This process is repeated over a range of magnetic field values. After collecting and storing the series of time traces at

different magnetic fields we have time/magnetic field/ signal intensity dataset, which is very useful for studying the lifetimes and physical and electronic structures of the RPs generated in photosynthesis RCs. In the Figure 4.1, the three dimensional dataset is shown for the triplet state of zinc tetraphenylporphyrin at the bottom left of the figure. The two dimensional "Time/EPR signal" has been extracted from the data set at a selected field position on the right of the field range where the signal is absorptive. And the "magnetic field/EPR signal" spectrum was extracted from the data set by calculating the difference in the average signal intensity in two time windows after and before the laser flash. In transient EPR, the RPs in photosynthetic RCs are generated by a laser flash. The strength of this technique in studying the ET in photosynthetic RCs is that it provides both geometric and kinetic information along with information on the local environment of paramagnetic species. Like any other experimental technique, it has some drawbacks, which are related to the very low sensitivity and limited time resolution, which at best is about 10 ns. As mentioned in the introduction section, some of the paramagnetic species are too short lived to be detected. Fortunately, the concept of ESP introduced in the previous chapter, to some extent solves these problems.

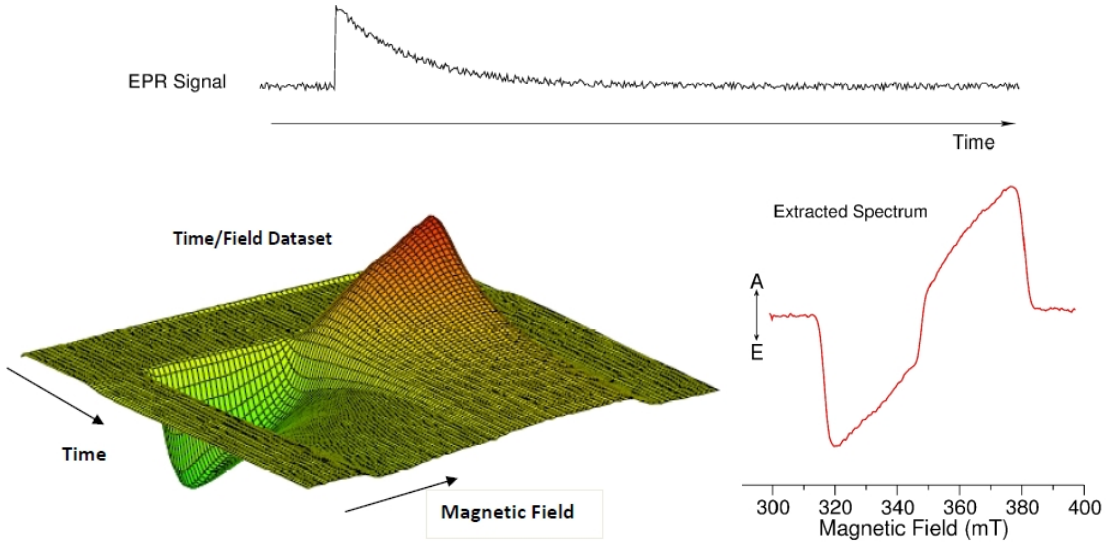

Figure 4.1: Time/Field EPR dataset. Used with permission [86]**. The description of each figure can be found in the text.**

4.1.1 The Effect of ESP on Transient EPR spectra

As discussed in the previous chapter, ESP is a direct result of the generation of the first RP in a pure singlet state. The correlation between the electrons that was present in the singlet state persists long enough to be detected as a non-Boltzmann distribution of the populations and coherent motion of the spin states in the RPs. That means, the ESP of each RP generated in a sequential ET depends on the evolution of the spin dynamic of precursors [59, 60 and 65]. If the lifetime of each precursor is greater than 500 ps, it can have a significant impact on the spin polarization of the subsequent RP [95]. Therefore, although the response time of a transient EPR spectrometer is usually greater than 10 ns, the spin evolution in precursors with lifetimes greater than ~500 ps influences the EPR spectra of subsequent RPs. Thus, even though some of the RPs in PS I and *Hb*RCs cannot be observed directly by transient EPR their properties can be deduced from the effect of their spin dynamics on the spectra of subsequent RPs. In the next part a brief explanation of how the effect of precursors can be taken into account in simulating the transient EPR of a sequential RP is given.

4.1.2 Sequential RP and the effect of precursors on Transient EPR signal

The polarization patterns of singlet-born sequential RPs have been studied by several authors [60, 64–67 and 95]. A general approach to this problem is complicated, but simplifications are possible for the conditions in the photosynthetic RCs. For instance, if the coherent oscillations are ignored, the polarization pattern of each RP can be written as a linear combination of polarization patterns of singlet precursor and contributions from the spin dynamics of precursors with lifetime greater than 500 ps [59, 60 and 96]. The latter can be divided to two parts: hyperfine and net polarization contributions.

4.1.2.1 Hyperfine contribution

The hyperfine contribution can be divided into two parts: The contribution from the donor and the contribution from the acceptor in each RP. The polarization generated in subsequent RPs depends on the local hyperfine field in the precursor. The polarization generated in the acceptor must be summed over all possible local hyperfine fields of the acceptor in the precursor. This is because there is no correlation between the local field in the two acceptors. When sum of the polarization from precursor acceptors with all possible local hyperfine fields is taken the result is zero [97]. Since the donor remains the same, no sum over the local fields of the donor must be done. Therefore, we are left with the hyperfine contribution from the donor, which gives rise to an antiphase doublet centered at the g-value of the donor in the EPR spectra for all subsequent RPs. The intensity of this contribution to the polarization is proportional to [59, 60]:

$$I^h \propto \frac{b_0 D}{k^2} \tag{4.1}$$

Where $b_0 = 2J_0 + d_0$ (0 refers to the primary RP), k is the rate of ET from the precursor RP to the subsequent RP and D is the linewidth in the precursor state. The assumption in eqn. (4.1) is that the back reaction rate is negligible compared to the forward ET, which is the case for the RCs under study in this thesis [97].

4.1.2.2 Net Polarization

This effect is caused by spin precessions of the radicals in precursor states of the RPs and manifests itself as pure absorption or emission in the contribution to the EPR spectrum from each radical. The net polarization effect for a given radical can be estimated as [97]:

$$p \approx \frac{b\,\Delta\omega}{k^2 + \Omega^2} \tag{4.2}$$

Where $b, \Omega, \Delta\omega$ and k are the spin-spin coupling $2(J + d)$, zero-quantum coherence frequency, resonance frequency difference and ET rate for the precursor RP. From this eqn, the dependence of the sign of the polarization (absorptive or emissive), on the sign of the spin-spin coupling and the Zeeman frequency difference of each RP can be inferred. Therefore, the polarization pattern of EPR visible RPs gives information on the geometry and lifetime of its precursor. There are two very useful limiting cases for eqn. (4.2), which are applicable in this study: a short-lived precursor and a long-lived precursor.

In the case of a short-lived precursor, the ET rate is large and eqn. (4.2) reduces to:

$$p \approx \frac{b\,\Delta\omega}{k^2} \tag{4.3}$$

and in the case of a long lived precursor, the ET rate becomes negligible. Moreover, if the lifetime of the precursor is long it means that the recombination rate is slow and hence the two electrons must be far apart. This implies that the

coupling is weak. Therefore, the spin-spin coupling in the zero-quantum coherence in eqn. (3.6) becomes negligible, which means $\Delta\omega \approx \Omega$ and eqn. (4.2) reduces to:

$$p \approx \frac{b}{\Delta\omega} \tag{4.4}$$

$\Delta\omega$ which depends on the strength of the external field (see eqn (3.4)) is in the numerator in eqn (4.3) and in the denominator in the eqn (4.4). Therefore, the net polarization increases at high field values for the short-lived precursors and decreases for long-lived precursors [96].

With these expressions combined with an estimate of the geometric and magnetic information of the system, the static polarization pattern of EPR-visible RPs, can be derived for static P_{700}^{+} PhQ^{-} and P_{700}^{+} F_x^{-} spectra, and those spectra can be used to determine the relative amounts of the two kinetics components from A_1 to F_x in PS I [95]. In chapter 6, a kinetic study of PS I from the wild type and two mutantstrains of *C. reinhardtii* in which the mutations affect either the A or B branch of ET is presented along with analysis of static spectra at extracted in different time windows. In the next part of this chapter, the principles of the echo modulation EPR technique will be briefly discussed.

4.2 Pulsed EPR

Pulsed EPR is an approach to EPR measurement in which a series of MW pulses excite the electron spins and then the signal induced by these pulses is measured in the absence of applied microwaves. The common technique in pulsed EPR is to measure a spin echo and vary the time between two strong MW pulses used to generate the echo. In many cases, the echo amplitude is modulated as a function of the spacing time. Information about hyperfine and dipolar interactions can be obtained from the frequency of this Electron Spin Echo Envelope Modulation (ESEEM) (for review see [62, 89]). When pulsed EPR is applied to light-induced spin correlated RPs the echo is phase shifted and is known as an Out of

Phase-ESEEM (OOP-ESEEM). The modulation of the OOP-ESEEM is sensitive to the dipolar coupling between the two radicals and almost independent of their relative orientations. Here, a brief explanation of the response of the light-induced RCs to the sequence of MW pulses is given. In order to derive the expected behavior of the system the density matrix formalism, which is introduced in the previous chapter is used.

In order to give a better insight into the theoretical and experimental aspects of pulsed EPR spectroscopy, first a brief review of the density matrix theory is presented and then the application of density matrix representation to Pulsed EPR is discussed.

4.2.1 Time Evolution of the Density Operator and Magnetization

Eqn. (3.17) is the general equation for the time evolution of the density matrix under a time-independent Hamiltonian. In order to determine the Hamiltonian in a pulsed EPR experiment, we need to consider the development of magnetization of the system under MW exposure and applied magnetic field. In the absence of MW irradiation, when the strong magnetic field is applied, the net magnetization of the system, which is the summation over all magnetic moments per unit volume, is given by:

$$M = \frac{1}{V}\sum_{i=1}^{N}\mu_i = -\frac{\beta}{V}\sum_{i=1}^{N} g_i \hat{S}_i \qquad (4.5)$$

and it is parallel to the applied field. By convention, the magnetic field direction is defined as the *z*-direction. In order to treat pulsed EPR experiments it is more convenient to transform the spin Hamiltonian from the laboratory frame to the frame rotating at the MW frequency. In this frame, the microwave pulses can be treated as rotation operators that rotate the net magnetization about a certain axis [90]. By convention, we assume that the MW field is in the x-direction. In the pulse sequence used in this thesis, the first pulse tips the magnetization 90^o

about the *x*-axis, then the magnetization evolves in the x-y plane. After a certain time (the spacing time between the two pulses) the second pulse tips it 180^o about *x*-axis again. Therefore, the Hamiltonian for the evolution of the density operator during the time when the MW pulses are applied can be written as [90]:

$$\widehat{\mathcal{H}}_{\mathbf{1}} = \omega_1 \widehat{\boldsymbol{S}}_x \tag{4.6}$$

Where $\omega_1 \approx \frac{1}{2}\beta(g_1 + g_2)B_1$, is the MW frequency. In the case where this frequency is much greater than ω_0, which means the MW field is much greater than the effective static field in the rotating frame, all EPR transitions are uniformly excited and the overall Hamiltonian reduces to eqn. (4.6). The angle of rotation is defined by:

$$\theta = \omega_1 t_p \tag{4.7}$$

In which t_p, is the length of the MW pulse. During the microwave pulses the evolution of the density matrix is given by:

$$\widehat{\boldsymbol{\rho}}(t) = \exp\left(-i\,\widehat{\mathcal{H}}t\right)\hat{\rho}(0)\exp(i\,\widehat{\mathcal{H}}t) \tag{4.8}$$

where $\widehat{\boldsymbol{\mathcal{H}}} = \widehat{\boldsymbol{\mathcal{H}}}_{\mathbf{1}} + \widehat{\boldsymbol{\mathcal{H}}}_{\mathbf{0}}$. For two MW pulses with the rotation angles of $\frac{\pi}{2}$ and π separated by a spacing τ and with the first pulsed applied at a time τ_L after a laser flash, the density matrix at $t = \tau_L + 2\tau$ has the following form:

$$\begin{aligned}\widehat{\boldsymbol{\rho}}(\tau_L + 2\tau) = \exp(-i\,\widehat{\mathcal{H}}_{\mathbf{0}}\tau)\exp(-i\,\pi\,\widehat{\boldsymbol{S}}_x)\exp(-i\,\widehat{\mathcal{H}}_{\mathbf{0}}\tau)\exp\left(-i\frac{\pi}{2}\widehat{\boldsymbol{S}}_x\right).\\ \widehat{\boldsymbol{\rho}}(\tau_L)\exp\left(i\frac{\pi}{2}\widehat{\boldsymbol{S}}_x\right)\exp(i\,\widehat{\mathcal{H}}_0\tau)\exp(i\,\pi\,\widehat{\boldsymbol{S}}_x)\exp(i\,\widehat{\mathcal{H}}_0\tau)\end{aligned} \tag{4.9}$$

The pulse sequence used in eqn. (4.9) can be written as $h\nu - \tau_L - \left(\frac{\pi}{2}\right)_x - \tau - (\pi)_x$ which is the case in the OOP-ESEEM experiment on light induced RPs in this thesis. The time diagram of the pulse sequence is illustrated in Figure 4.2.

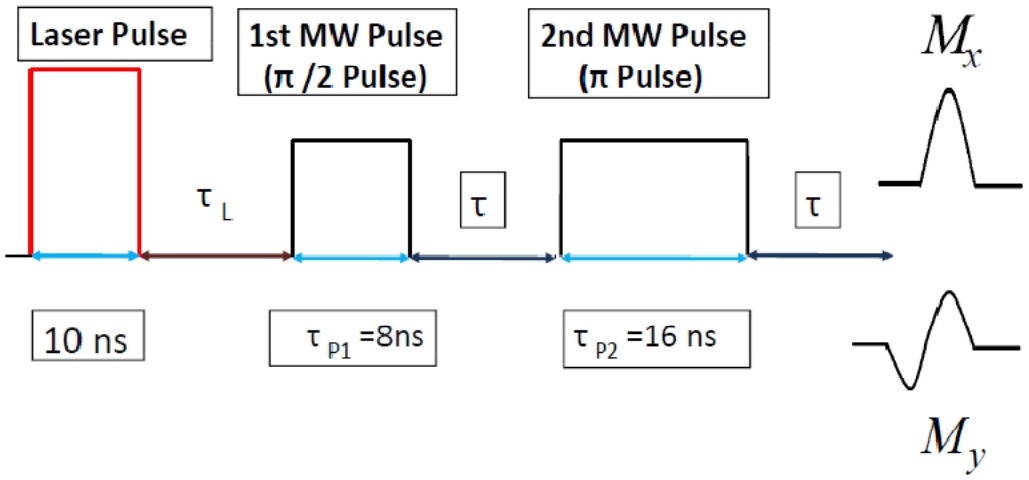

Figure 4.2: Timing diagram for the out-of-phase-echo experiment. In this experiment if we assume that the MW field is in x-direction then the echo is absorption in the x-channel and dispersion in the y-channel. The two pulses rotate the magnetization arises from singlet born RP about the x-axis.

To avoid any influence from the coherence present initially in the spin system and reach eqn. (3.24), τ_L is chosen to be long enough (about 300 ns) to fulfill the condition $\Omega\tau_L \gg 1$ and be much longer than the phase relaxation of the coherence.

When the pulse sequence described above is applied to a singlet-born radical pair, the echo is observed along *x*-direction in the rotating frame whereas for a stable radical it is observed along *y*-direction. This means the echo is phase shifted by 90º for the radical pair. If we want to derive the transverse magnetization as observable operator in Pulsed EPR experiment we need to calculate:

$$\widehat{\boldsymbol{S}}_x = \mathrm{Tr}\left(\widehat{\boldsymbol{S}}_x\, \rho\right) \tag{4.10}$$

$$\widehat{\boldsymbol{S}}_y = \mathrm{Tr}\left(\widehat{\boldsymbol{S}}_y\, \rho\ \right)$$

In order to accomplish this calculation we have to insert the matrix representation for all terms in eqn. (4.9). The result for the transverse magnetization at time $t = 2\tau + \tau_L$ as a function of the spacing between the pulses is given by [88]:

$$\begin{aligned} M_x(\tau) &= \sin^2 2\alpha \,.\cos^2 2\alpha \,.\sin(\Gamma\tau)\,[1-\cos(2\Omega\tau)] \\ &= \frac{\Delta\omega^2(2J+d)^2}{4\Omega^2}\sin(\Gamma\tau)\,[1-\cos(2\Omega\tau)] \\ M_y(\tau) &= 0 \end{aligned} \tag{4.11}$$

In which $\Gamma = 2(\mathrm{J}-\mathrm{d})$. For a disordered sample and assuming that all spins are excited equally by the microwave pulses, the signal is the integral over all possible orientations (powder average) of the transverse magnetization:

$$\langle M_x(\tau)\rangle = \frac{1}{4\pi}\int_0^{2\pi}\int_0^{\pi} M_x(\tau,\theta,\varphi)\sin\theta\; d\theta d\,\varphi \tag{4.12}$$

The main feature of eqn. (4.11) is that $\boldsymbol{M_x}$ has two oscillatory terms, one with the frequency $\Gamma = 2(\mathrm{J}-\mathrm{d})$, which causes the signal amplitude to be modulated with a frequency determined by the dipolar and exchange interactions, the other term oscillates with the zero-quantum coherence frequency. This modulation decays within about 100 ns, and therefore experimentally the observed modulation frequency is Γ:

$$\begin{aligned} M_x(\tau) &= sin^2 2\alpha \,.cos^2 2\alpha \,.sin(\Gamma\tau) \\ &= \frac{\Delta\omega^2(2J+d)^2}{4\Omega^2}sin(\Gamma\tau) \end{aligned} \tag{4.13}$$

Hence, the OOP-ESEEM signal depends strongly on the spin-spin couplings, which usually cannot be determined in the transient EPR experiment because they are smaller than the inhomogeneous line broadening. Therefore, these two TREPR experiments are two complementary techniques in studying photosynthetic RCs[4]. In the next three chapters the application of these two techniques to samples of PS I from mutant and wild type strains of cyanobacteria and green algae and to samples of *Hb*RCs will be discussed.

[4]However, it should be mentioned that at X-band oscillations from the hyperfine couplings are also expected to contribute to the echo modulation. We assume that they can be ignored but they limit the accuracy with which the couplings can be determined

5 An Out of Phase Electron Spin Echo Study of PsaA-M688H and PsaB-M668H mutants of two Different Species

5.1 The concept of directionality in ET

As pointed out in the introduction section, all known photosynthetic RCs organisms have two branches of ET cofactors. The ET is considered to be unidirectional if it occurs in only one of the two branches, and bidirectional if both branches are involved in the ET process. The definition of unidirectional and bidirectional is used to mean near-exclusive use of one branch or two branches within the uncertainty of the experimental techniques employed to study the directionality. In PS I RCs, despite the fact that there is high symmetry between the two branches, they are distinguishable through the interaction of the cofactors with their surroundings. One of the main strategies to address the question of directionality in PS I RCs is to make point mutations to amino acid residues near specific cofactors to selectively alter the behavior of the cofactor in each branch.

5.2 Point Mutagenesis Studies to Address the Directionality of ET

Such mutation studies are very useful for investigating the role of the cofactors in ET. For instance, if ET can be blocked in one branch by altering the midpoint potential of a cofactor it provides a significant opportunity to measure the activity of each branch by comparing to the behavior of PS I from the mutant and from the wild type (WT). For point mutagenesis studies to be valid, at least two conditions must be met. First, the position of the related amino acid relative to the cofactor(s) must be known. With the help of crystal structure of a species the position of amino acids can be identified. The high resolution crystal structure is known for one species of cyanobacterium and for PS I from spinach [97, 98]. In addition, the amino acid sequence is highly conserved between species so these structures can be used for predicting the effect of mutations in other species. This is the reason that the amino acid numbering scheme in this thesis applies to *Synechococcus elongatus* for which the crystal structure of PS I is known, ***i.e*** the corresponding numbers in *C. reinhardtii* are different. But as mentioned before, the amino acid sequence is highly conserved between species. Second, the effect of mutations should not affect the RCs so that it perturbs the whole system. It means, if a too drastic a change is made the organism will not produce any PS I and will not grow.

However, point mutagenesis studies on PS I RCs have provided strong evidence that both branches are active and that ET occurs mostly in the A-branch. The relative use of the B branch is estimated to be less than 20% in the cyanobacterium *Synechocystis* sp. PCC 6803 [99] but ~40% in the green alga *C. reinhardtii* [100, 101]. However, contradictory conclusions have been drawn in different papers in the literature. This is particularly true of mutations to the methionine residues PsaA-M688 and PsaB-M668, which act as the axial ligands to chlorophylls $ec3_A$ and $ec3_B$, respectively.

5.3 Literature Review on the Preparation and Behavior of PsaA-M688H and PsaB-M668H

Quite different results have been reported in studies of histidine mutants of the methionine residues PsaA-M688 and PsaB-M668 of PS I RCs in the cyanobacterium *Synechocystis* sp. PCC 6803 and the green alga *C. reinhardtii*. In optical studies on the *C. reinhardtii* species, a long-lived chlorophyll-*a* anion was observed and interpreted as an indication that the electrons cannot reach PhQ_A/PhQ_B [102, 103]. The optical data do not show which branch the chlorophyll anion is in, but it is reasonable to assume it is in the branch with the mutation. On the other hand, a recent study has shown that the same mutation in *Synechocystis* sp. PCC 6803 results only in partial blockage of ET in the branch carrying the mutation [104]. Briefly, in PsaA-M688H/PsaB-M668H it was found that about 50% of the electrons were passed forward from A_{0A}/A_{0B} to PhQ_A/PhQ_B, the remaining electrons were found to recombine with P_{700}^+. The electrons that passed A_{0A}/A_{0B} and reach PhQ_A/PhQ_B did not proceed forward to the iron sulfur clusters, but recombine with P_{700}^+ with lifetimes of ~15 µs and ~5 µs, respectively [104]. Hydrogen bond formation between the *d*-nitrogen of the histidine with the O_1 carbonyl oxygen of the PhQ (phylloquinone) was the suggestion by the authors as the reason for the altered PhQ to Fx kinetics [104]. The position of methionine and histidine with respect to A_0 and PhQ is shown in Figure 5.1. Therefore, in contrast to the observations in *C. reinhardtii* the mutations in *Synechocystis* sp. PCC 6803 do not completely block ET from A_0 to PhQ and alter the ET kinetics for PhQ to F_x.

In addition, at low temperature reversible ET to PhQ occurs in a fraction of the RCs. In a pulsed EPR study, ESEEM data on whole cells of the wild type and PsaB-M668H mutants in *Synechocystis* sp. PCC 6803 at 100 K suggested that the reversible ET exclusively occurs in the A-branch (branching ratio of < 0.2) and no signal was observed in the PsaA-M688H mutant [105]. In support of this result, in a recent high field EPR study reversible ET was found to proceed

exclusively via the A-branch of PS I RCs of wild type *Synechocystis*sp. PCC 6802 at cryogenic temperature [106]. But on the other hand, there is evidence that in the whole cells of the same mutants in *C.rheinhartdii* that the ET is bidirectional. A branching ratio of 0.42 was assigned to ET in B-branch based on EPR measurements of whole cells that were illuminated before freezing [105].

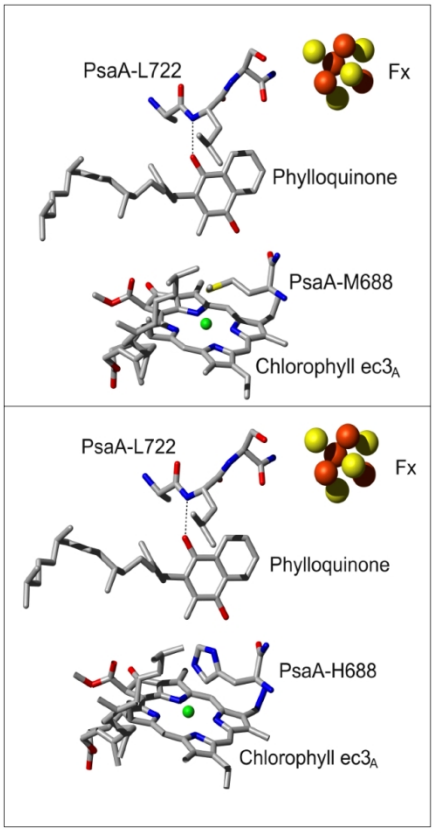

Figure 5.1: .Top: The arrangement of the methionine residue PsaA-M688 in wild type PS I, between A_0 of the A-branch(chlorophyll $ec3_A$) and phylloquinone molecules; Bottom: A structural model in which the methionine residue has been replaced with histidine. Used with permission [104]

Hence, we have evidence that the ET is species dependent but it is possible that the different behavior is because the data have been collected under different conditions in different laboratories. Thus, there is a need to perform all the experiment in the same laboratories and under the same conditions.

The systematic study has been done by collaboration of three research groups. The point mutants of *Synechocystis* sp. PCC 6803 were prepared by Dr. Junlei

Sun working with Prof. John Golbeck at The Pennsylvania State University. The same mutants in *C. reinhardtii* were prepared by Dr. Michael McConnell working with Profs. Kevin Redding and Andrew Webber at Arizona State University. All EPR experiments have been carried out in the EPR laboratory at Brock University. The OOP-ESEEM data were collected as a part of this thesis. Here, we present results that show that there are indeed significant differences between the Met to His mutants in the two species.

5.4 Experimental Setup for OOP-ESEEM Experiment

The OOP-ESEEM experiments have been performed at 80 K on a Bruker Elexsys E580 X-band spectrometer. The echo was generated using the following timing sequence: laser flash $-\tau_L-(\frac{\pi}{2})_x-\tau-(\pi)_x$, where $(\frac{\pi}{2})_x$ and $(\pi)_x$ are 8 ns and 16 ns microwave pulses applied in the *x*-direction in the rotating frame, respectively. The delay between the two microwave pulses was varied in 4ns steps starting from 64 ns. The echo intensity was integrated over a 48 ns window centered at the echo maximum at $t = 2\tau$ after the first microwave pulse. The delay between laser flash and initial microwave pulse (τ_L) was 400 ns. A Continuum Surelite Nd-YAG laser operating at 532 nm, 10 Hz and 4.0 mJ/pulse was used to excite the sample. PS I particles from the point mutant strains PsaA-M688H and PsaB-M668B of *Synechocystis* sp. PCC 6803 and in *C. reinhardtii* were supplied by our collaborators. The details of the generation of the point mutations and isolation of PS I are reported in [107] for *Synechocystis* sp. PCC 6803 and in [108] for *C. reinhardtii* samples. The chlorophyll concentration of all samples was 1 to 2 mg Chl/ml. Sodium L-ascorbate and phenazinemethosulfate (PMS) were added to final concentrations of 50 mM and 5 μM, respectively. Before illumination, all samples were dark adapted for 20 minutes on ice to completely reduce any P_{700}^{+} present in them and then frozen in the dark

5.5 Results and Discussion

Figure 5.2 shows transient EPR spectra at room temperature of the two mutants and the WT from two species *Synechocystis* sp. PCC 6803 and *C. reinhardtii.* The wild type, PsaA-M688H mutant, and PsaB-M668B mutant are in the top, middle and bottom panels of Figure 5.2, respectively. The values for the time shown in the figures are the time after laser flash at which the spectra were extracted from time/field data sets. The times were chosen to show the time evolution of the spin-polarized signal qualitatively. Starting from the WT spectra, we can see at 220 ns the spectra for both species are a mixture of the E/A/E pattern from $P_{700}^{+}PhQ_A^{-}$ and the almost purely emissive pattern of $P_{700}^{+}(FeS)^{-}$ [5]. The lifetime of the former pattern is reported to be 240±20 ns and 220±20 ns for the ET from PhQ_A^{-} to F_X in *Synechocystis* sp. PCC 6803 and *C. reinhardtii*, respectively [109]. At 1000 ns after the laser flash the polarization pattern becomes almost purely emissive pattern results from $P_{700}^{+}(FeS)^{-}$. Fits of the kinetic traces show a decay lifetime of 2 µs for this pattern for the two species. It has been shown previously that this decay is due to spin relaxation [25]. The polarization pattern from PhQ_B^{-} is not resolved in the spectra because of its short lifetime (about 20ns) but, the B-branch ET leads to a contribution from $P_{700}^{+}(FeS)^{-}$ at early time. When a significant amount of $P_{700}^{+}(FeS)^{-}$ is present at early time the absorptive feature of the E/A/E pattern becomes weak because it overlaps with the emissive signal from $P_{700}^{+}(FeS)^{-}$. And it can be obviously seen in Figure 5.2 that this contribution is larger in the *C. reinhardtii.* wild type sample compared to *Synechocystis* sp. PCC 6803, which is in qualitative agreement with the reported analyses of these samples at room temperature that suggest an estimated contribution of 40% B-branch ET in *C. reinhardtii* and < 20% in *Synechocystis* sp. PCC 6803. In addition to these differences, the spectra at 1000 ns for both WT species are slightly different in the high field part where the absorptive signal for the *C. reinhardtii* is stronger

[5] we use the notation (FeS) because we cannot tell which of the three iron sulfur clusters the electron is on but as mentioned in Chapter 1 it is known that the first step is to F_x.

compared to *Synechocystis* sp. PCC 6803. The polarization pattern of $P_{700}^{+}(FeS)^{-}$ depends on the lifetime and geometry of the precursor. Thus, B-branch ET produces a different $P_{700}^{+}(FeS)^{-}$ polarization pattern than A-branch transfer. The larger absorption in the *C. rheihardtii* $P_{700}^{+}(FeS)^{-}$ spectrum is probably due to a larger contribution from B-branch transfer. Considering the fact that the reported B-branch ET in *C. reinhardtii* is larger than *Synechocystis* sp. PCC 6803, it is reasonable to assign the stronger absorptive signal at 1000 ns in the WT samples as due to the B-branch contribution to the EPR signal.

The effect of the PsaA-M688H mutation in the A-branch shown in the middle part of Figure 5.2, represents an obvious difference between the two species. Here we see in both cases the early spectrum just decays and does not evolve into a different spectrum at late time. In the *Synechocystis* sp. PCC 6803 spectrum only an E/A/E pattern, which can be assigned to $P_{700}^{+}PhQ_{A}^{-}$ is observed. On the other hand, in the left panel for the *C. reinhardtii* only the E/A pattern with the predominant emissive pattern from $P_{700}^{+}(FeS)^{-}$ is observed. Therefore, the effect of mutation in the A-branch is species dependent and causes these differences in transient EPR spectra. One of the obvious difference between the A-mutant and WT spectra for the *Synechocystis* sp. PCC 6803, is that the A-mutant spectra lacks the shoulder on the absorptive peak in the centre of the WT spectrum which is known to be due to hyperfine coupling to the methyl group at the 2-position of the PhQ headgroup [110]. This difference in the hyperfine structure in the *Synechocystis* sp. PCC 6803 samples has been proposed to be the result of H-bonding between the *d*-nitrogen of PsaA-H688 and the O_1 carbonyl oxygen of PhQ [104]. Moreover, from the optical data it has been proposed that in a fraction of the A-mutant sample, the ET past the PhQ_{A}^{-} is blocked because of the stabilization of the quinone molecule by the H-bond, and in another fraction the ET transfer is blocked beyond chlorophyll ec-A3 [104]. In the right part of the Figure 5.2, the story is different for the PsaA-M688H mutant of *C. reinhardtii*. In the spectra there is no evidence for $P_{700}^{+}PhQ_{A}^{-}$, indicating that the ET is blocked past the ec-3_A chlorophyll

molecule, and what we see is the $P_{700}^{+}(FeS)^{-}$ state arising from B-branch ET. The stronger absorptive peak on the high field part of the spectrum is a support for this argument.

Finally, for the B-mutant spectra, in the bottom part of the Figure 5.2, it is seen that the spectra of the species are almost identical. If these spectra are compared to the related WT spectra, it can be seen that the difference in the *C. reinhardtii* spectra is greater. In addition, the weaker contribution from $P_{700}^{+}(FeS)^{-}$ state at early time in both species indicates a greater contribution from A-branch ET. Especially, if we look at the B-mutant in *C. reinhardtii* for all spectra both the contribution from $P_{700}^{+}(FeS)^{-}$ at early time and the absorptive part of the late signal are very weak compared to the WT and A-mutant spectra. Therefore, the effect of this mutation can be explained as the blockage of ET in the B-branch in *C. reinhardtii*. In *Synechocystis* sp. PCC 6803 optical data indicate that ET to PhQ_B is probably not completely blocked but because of the inherently small amount of B-branch transfer its contribution is small [107]. Thus, the spectra in the bottom panel of the Figure 5.2 represent predominantly A-branch ET in both species.

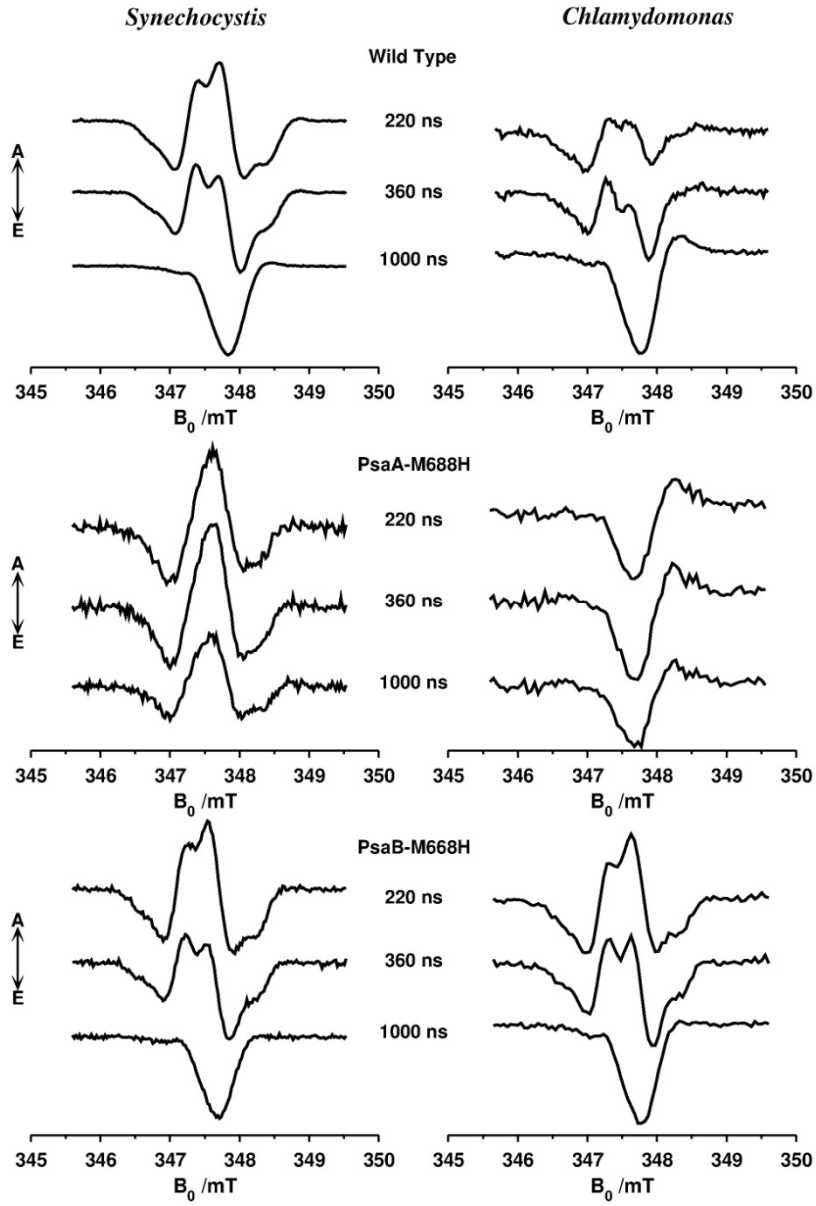

Figure 5.2: Room temperature spin-polarized transient EPR spectra of Wild Type, PsaA-M688H and PsaB-M668H of *Synechocystis* sp. PCC 6803 (Left) and *C. reinhardtii*s (Right). Taken from [109] **used by permission of the authors.**

The transient X-band EPR spectra of these mutants in the two species have been studied at low temperature as well. The result of this study is represented in Figure 5.3. Before explaining the features of the spectrum represented in Figure 5.3, it should be noted that at 80K reversible ET to PhQ is observed and previous point mutation experiments suggest that the spectrum is dominated by the A-branch RP [74, 103]. In addition to the reversible ET, irreversible ET to F_A/F_B also occurs and that is why the fraction of each branch in the ET is not

known. It has been speculated that irreversible ET occurs via the B-branch but this has never been shown conclusively [28, 111]. As can be seen, the B-mutant and WT spectra from *Synechocystis* sp. PCC 6803 are identical to each other and to the B-mutant spectrum for *C. reinhardtii*. Like the room temperature data the spectrum of the WT from *C. reinhardtii*is also similar to these three spectra but shows some small differences. Again, the A-mutant spectra are different. However, in both cases the signal is weaker than in the WT as would be expected if the ET in the A-branch was blocked or partially blocked. By considering the fact that there is no evidence for any A-branch ET in the A-mutant in *C. reinhardtii* at room temperature [109], we expect that we should not really get a spectrum at low temperature in the A-mutant. Thus it is not clear which RP we are observing in C. reinhardtii and why the spectrum is different in Synechocystis sp. PCC 6803. To test this, we have performed OOP-ESEEM measurements.

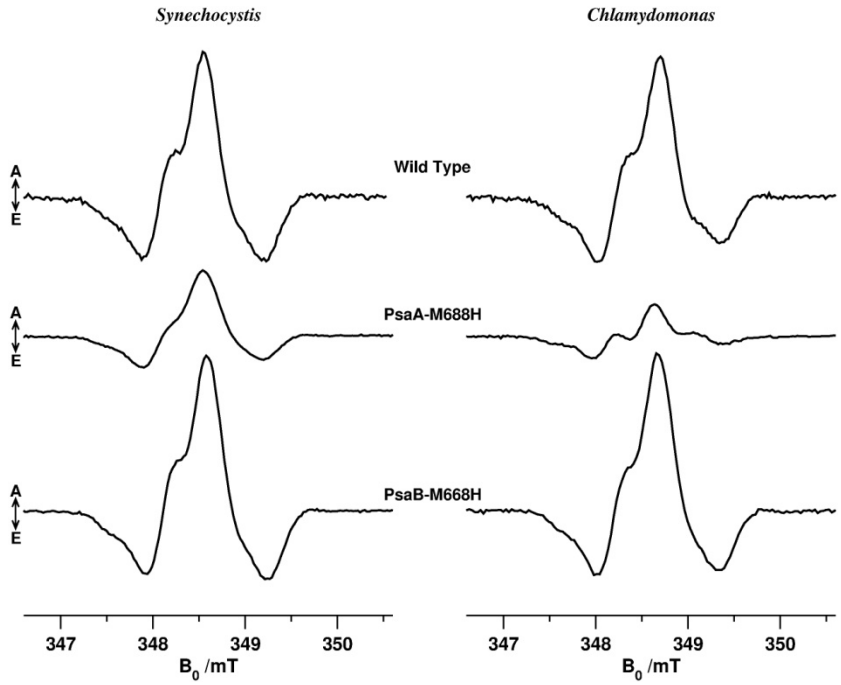

Figure 5.3: Spin polarized Transient EPR of Wild Type, PsaA-M688H and PsaB-M668H of *Synechocystis* sp. PCC 6803 (Left) and *C. reinhardtii*is (Right) at 80 K. Taken from [109] **used by permission of the authors.**

The OOP-ESEEM traces for the two species are shown in Figure 5.4. From top to bottom the first two sets of curves represent the OOP-ESEEM modulation of the *C. reinhardtii* for the A-mutant and B-mutant compared with the WT trace, respectively. The bottom two sets of curves are the corresponding traces for the *Synechocystis* sp. PCC 6803 samples. The black, blue and red traces represent WT, PsaB-M668H and PsaA-M688H respectively, and all time traces are normalized so that the amplitude of the first maximum is the same in all cases. The dashed traces are calculated echo modulations curves plotted using the same color as the corresponding mutant or WT experimental spectra they have been fitted to. The parameters used to fit the calculated modulation curves to the experimental ones are presented in Table 5.1. The vertical lines in Figure 5.4 are the location of corresponding minima in each sample. The position of the minimum is a measure of the main frequency in the modulation curve. If the minimum occurs earlier the frequency is higher and if it appears later the frequency is lower. The color of each vertical line is the same as the corresponding sample. As can be seen in the figure, the modulation frequencies are the same for all three *Synechocystis* sp. PCC 6803 samples but slightly different frequencies are observed for *C. reinhardtii* samples. The modulation frequency of the OOP-ESEEM depends on the dipolar coupling of the RP. From the X-ray structure [14] and EPR studies showing that the unpaired electron in P_{700}^{+} is localized on the B-branch chlorophyll of the P_{700} dimer [112], it is known that the distance between the two electrons is slightly shorter in $P_{700}^{+}PhQ_{B}^{-}$ compared to $P_{700}^{+}PhQ_{A}^{-}$ [75, 106 and 113–115]. Thus, for *C. reinhardtii* the data indicate that both $P_{700}^{+}PhQ_{A}^{-}$ and $P_{700}^{+}PhQ_{B}^{-}$ contribute to the signals but the relative contributions vary between the samples.

For the *Synechocystis* sp. PCC 6803 samples the same frequency was obtained within the error of the fit. For the WT it has been shown that the modulation curve is due to the A-branch RP [106, 116], and since all three samples give the same frequency we can conclude that they all represent the A-branch RP. This result supports the transient EPR data in the previous section. Since we know

that the frequency in the *Synechocystis* sp. PCC 6803 corresponds to the A-branch RP, we can conclude that the signal in the PsaB-M668H in *C. reinhardtii* is also from the A-branch RP because it has almost the same frequency and is what we would expect since the mutation should block B-branch ET. The other two *C. reinhardtii* samples show faster oscillations, which implies that they have a contribution from the B-branch RP. The PsaA-M688H has the highest frequency and therefore should have the largest contribution.

For the fitting functions of the A-mutants and B-mutants in both species the geometry obtained from high field EPR studies have been used [106, 117]. As discussed before, the modulation of OOP-ESEEM traces depends strongly on the spin-spin couplings of the observed RP, therefore the dipolar and exchange couplings can be derived from fitting of the OOP-ESEEM traces.

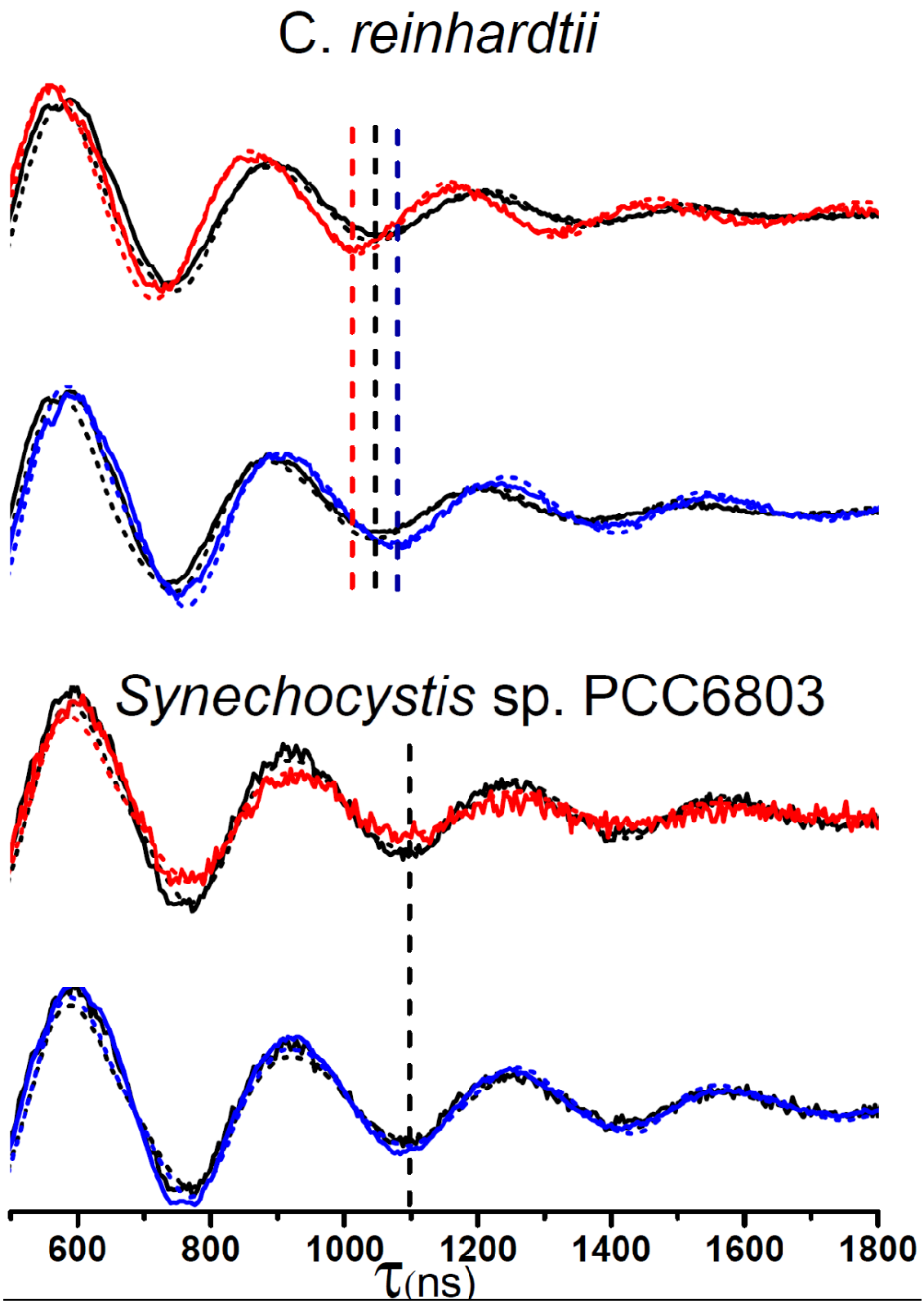

Figure 5.4: OOP-ESEEM traces at 80 K. Black, blue and red curves represent WT, PsaB-M668H and PsaA-M688H respectively. The vertical lines represent the place of a adjacent minima in each trace correspond to a specific mutant.

In Table 5.1 these results accompanying the corresponding distance between the two radicals is presented. Here, it is assumed that the exchange coupling is very small compared to dipolar coupling and the value has been kept fixed as 0.001 mT as in many previous studies [96, 106, 117 and 118]

Species	Mutant	D (mT)	J (mT)	r (Å)
Synechocystis sp. PCC 6803	PsaA-M688H	-0.165	0.001	25.6
	PsaB-M668H	-0.165	0.001	25.6
	Wild Type	-0.165	0.001	25.6
C. reinhardtii	PsaA-M688H	-0.172	0.001	25.0
	PsaB-M668H	-0.168	0.001	25.5

Table 5.1: The parameters used for fitting the experimental OOP-ESEEM modulation curves of $P_{700}^{+}PhQ^{-}$. D, J and r are dipolar coupling, exchange coupling, and the distance between the two radical centers of the RP. The error in D is 0.001 mT and for r is 0.1 Å. For the fitting of the *C. reinhardtii* WT sample a mixture of 60 % of B-mutant and 40% of A-mutant have been used.

From this table we see that the dipolar coupling related to B-mutant in *C. reinhardtii*is close to its related value in *Synechocystis* sp. PCC 6803, and the magnitude of this value in the A-mutant sample is greater than the two previous mentioned values. These results combined with room temperature data which do not show any 200 ns phase, implies that the data from the PsaA-M688H must be from the B-branch RP. Hence, the distance between the two RPs $P_{700}^{+}PhQ_{A}^{-}$ and $P_{700}^{+}PhQ_{B}^{-}$ can be derived by using eqn. (2.24) and the dipolar couplings obtained for PsaB-M668H and PsaA-M688H respectively. Also, for the *Synechocystis* sp. PCC 6803 samples the distance for the RP, $P_{700}^{+}PhQ_{A}^{-}$ is derived with the same approach. All of these results are presented in the Table 5.1. These distances represent the distance between the centers of spin density in the two radicals. In the case of PS I, the centre of spin density of the donor P_{700}^{+} is known to be localized largely on the chlorophyll that bound to the PsaB

subunit [97, 119]. For the acceptor, the center of spin density is delocalized over the head group of phylloquinone molecule, and the centre of the spin density can be taken as the midpoint between the two carbonyl oxygen atoms

For the fitting of the *C. reinhardtii* WT sample a mixture of 60 % of B-mutant and 40% of A-mutant has been used, which shows a very good agreement with the experimental modulation curve. This result for the branching ratio is in agreement with that found by Li et. al [100]. However, it does not represent the relative use of the two branches because as previously mentioned a fraction of the complexes are trapped at $P_{700}^{+}(F_A/F_B)^{-}$. Moreover, it is known that the reversible ET to the iron sulfur clusters occurs under the conditions used here [27]. It is likely that at least some of the reversible PhQ to F_x ET occurs with a lifetime of ~20 ns because this lifetime has been found to be temperature independent [27]. In both cases, trapping as $P_{700}^{+}(F_A/F_B)^{-}$ and/or fast ET results in a fraction of PS I complexes that would not be detected by OOP-ESEEM.

It should be noted here, that the iron sulfur-clusters were not chemically pre-reduced. Therefore, in the samples for which a contribution from the B-branch RP is observed, ET from PhQ_B to Fx becomes blocked in a fraction of complexes at low temperature.

The overall result of this set of experiments is that the directionality of ET in PS I RCs, is species dependent. It has been shown that in *Synechocystis* sp. PCC 6803 RCs, the reversible ET is strongly biased towards the A-branch at low temperature, but for *C. reinhardtii,* although most of the reversible ET occurs in the A-branch, a noticeable fraction takes place in the B-branch.

.

6 PsaA-A680N and PsaB-A660N, Transient EPR and Pulsed EPR Studies

In continuation to the study of the role of different residues near the cofactors, together with our collaborators at Arizona State University we decided to investigate the role of the eC2 chlorophylls in the ET by making point mutations of PsaA-A680 and PsaB-A660 in *C. reinhardtii*. The location of PsaA-A680 and PsaB-A660 in each branch is represented in the Figure 6.1. As can be seen in this figure, this alanine residue is located close the eC2 chlorophyll with the methyl group of alanine directed toward the eC2 chlorophyll as illustrated in Figure 6.2. Alteration of the methyl group is expected to affect the excitation energy coupling and ET between the eC2 chlorophyll and eC3 chlorophyll in each branch. After replacement of this residue with some other amino acids like cysteine, histidine, aspartic acid, isoleucine, and asparagine, our collaborators found that the asparagine mutants gave the best combination of producing an observable effect in the transient absorbance spectroscopy and accumulating sufficient amounts of PS I to work with [120].

Samples of isolated PS I complexes from the PsaA-A680N and PsaB-A660N mutants of *C. reinhardtii* were prepared by our collaborators for EPR studies. The details of preparation of the samples are explained in [120].

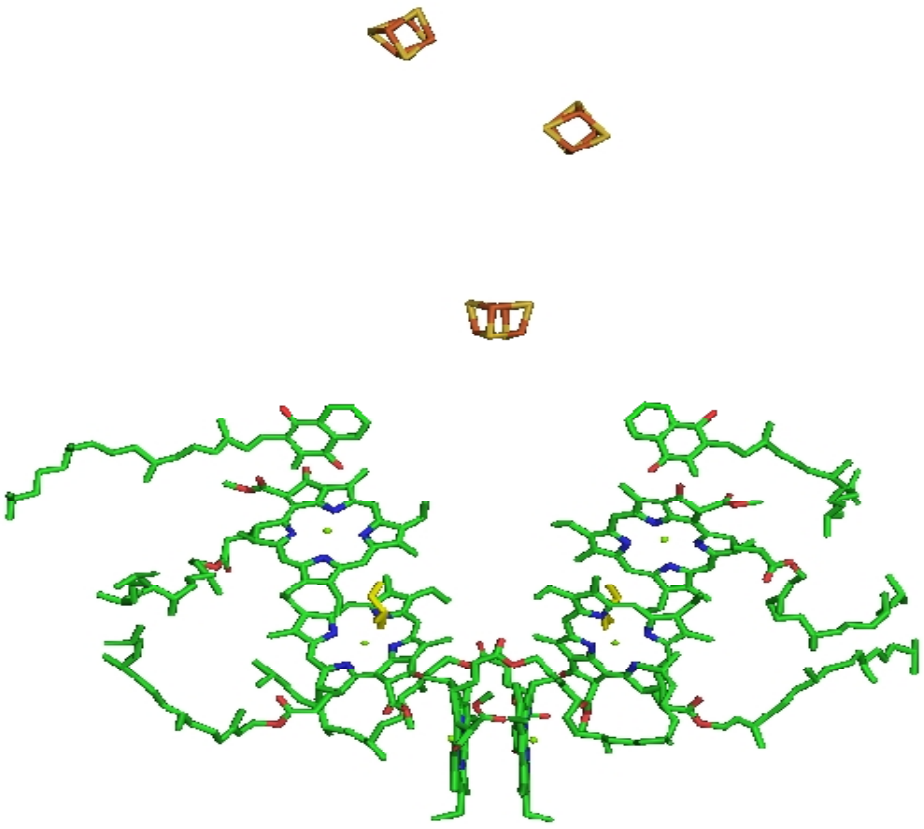

Figure 6.1: Position of alanine on each branch in PS I represented by yellow color, used with permission of author [120]**.**

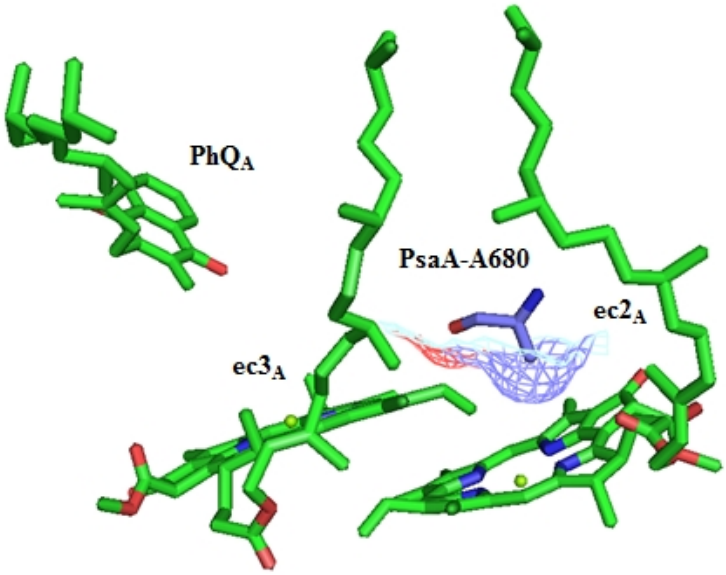

Figure 6.2: Position of alanine between the $ec2_A$ and $ec3_A$ chlorophyll molecules and the PhQ molecule in the A-branch of PS I RC [120]**.**

6.1 Transient and Pulsed EPR Setup

Transient EPR experiments were carried out using a modified Bruker ER 200D-SRC spectrometer with ER 041 X-MR X-band and ER 051 QR Q-band microwave bridges. A Flexline ER 4118 X-MD-5W1 dielectric resonator was employed at 80 K and an ER 4103 TM cylindrical mode resonator was employed for room temperature X-band experiments. For Q-band experiments an ER 5106 QT-W cylindrical resonator was used. In order to keep the temperature stable during the experiments an Oxford Instruments CF935 gas flow cryostat was used. In all transient EPR experiment the signal was collected in direct-detection mode with a home-built broadband amplifier (bandwidth > 500 MHz). The signal was digitized using a LeCroy LT322 500 MHz digital oscilloscope and saved on a PC for analysis. The OOP-ESEEM modulation curves were collected with the same experimental setup described in the previous chapter. The samples had a Chl concentration of 1 to 2 mg Chl/mL and they were treated with 1 mM sodium ascorbate and 50 µM phenazinemethosulfate (PMS) to final concentrations of 50 mM and 5 µM, respectively. In order to make sure that P_{700}^{+} is reduced prior to the low

temperature experiments, the samples were dark adapted for 20 minutes on ice and frozen in the dark.

6.2 Room Temperature X-band Transient EPR Results

The room temperature spin-polarized transient EPR spectra of PS I complexes isolated from the wild type and the PsaA-A660N, PsaB-A680N and WT mutants are shown in Figure 6.3. The spectra shown on the left have been extracted from time/field data sets at 220 ns, 360 ns and 1000 ns (1 μs) after the laser flash. The right panel of Figure 6.3 shows transients taken at the field positions indicated by the corresponding arrows under the spectra. The time traces and spectra are normalized to the emissive signal due to $P_{700}^{+}(FeS)^{-}$ state at field position "b" indicated in the figure. The dashed curves are calculated spectra and time traces that have been fitted to the experimental data.

The details of the WT spectra are given in the previous chapter. Briefly, we can see the evolution from a mixture of $P_{700}^{+}PhQ_A^{-}$ and $P_{700}^{+}(FeS)^{-}$ at 220 ns to pure $P_{700}^{+}(FeS)^{-}$ at 1000 ns. The time trace at field position "a" has only a contribution from PhQ_A^{-} so it decays with 200 ns. At position "b" the $P_{700}^{+}PhQ_A^{-}$ spectrum is absorptive and $P_{700}^{+}(FeS)^{-}$ is emissive so the spectrum evolves from an absorptive signal at early time to an emission at late time at this field position. This time behaviour at positions "a" and "b" is illustrated in the right panel in Figure 6.3. Because the contribution from PhQ_B^{-} to F_X ET with a lifetime of 20 ns results in an emissive signal from $P_{700}^{+}(FeS)^{-}$ within the risetime of the spectrometer the absorptive contribution to the spectrum at 220 ns and in the time trace at position b is weak. From the simulation of the whole time/field dataset we can estimate the size of the fraction of B-branch ET. Details of the simulation procedure are given in [121]. For the simulation shown in the figure, 51% of B-branch and 49% of A-branch contribution reproduce the experimental dataset reasonably well.

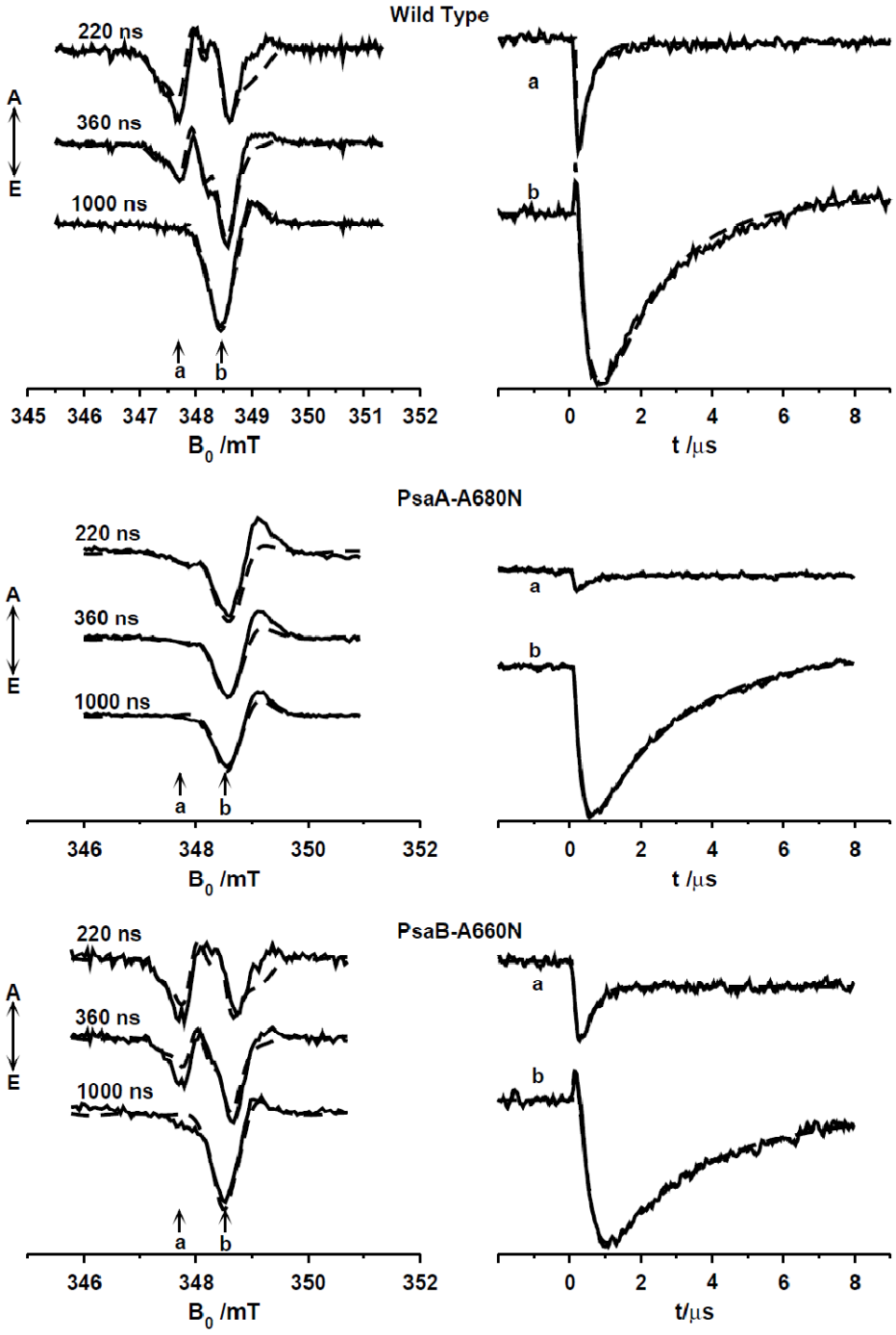

Figure 6.3: Room temperature X-band spin-polarized transient EPR. Left panel: Field-dependent spectra. Right Panel: Time-dependent transients (right). The details of each trace are explained in the text. The negative offset at long times in transients a and b for the PsaB-A660N mutant is an artifact generated by laser light striking the walls of the resonator.

This result is in agreement with transient absorbance optical data reported in [122]. The parameters used in the simulation were taken from [106] for A-branch and [123] for B-branch ET. With the assumption that the lifetime of fast phase ET is 20 ns, the lifetime for the slow phase in the simulation for WT spectra is found to be 200 ns.

In the middle part of the Figure 6.3 the EPR spectra for PsaA-A680N are shown. In the left panel it can be seen that there is very little $P_{700}^{+}PhQ^{-}$ present at early time and the spectrum is mostly just the $P_{700}^{+}(FeS)^{-}$ RP spectrum. In the right panel for the time traces, the signal at field position "a" is very weak and at position "b" there is no absorptive contribution at early time indicating that the $P_{700}^{+}PhQ^{-}$ contribution is much weaker than in the WT. The fitted simulation results for the PsaA-A680N mutant in Figure 6.3 with 70% of B-branch (the fast component) ET indicate that the mutation changes the relative use of two branches. However, from the EPR data it is not possible to distinguish between blockage of ET in the A-branch or redirection of electrons into the B-branch. The relatively strong absorptive contribution to the $P_{700}^{+}(FeS)^{-}$ spectrum at 1000 ns of PsaA-A680N is similar to that observed for the PsaA-M688H mutant discussed in the previous chapter and is also indicative of a greater relative contribution from the B-branch. It is not reproduced in our simulation suggesting that the parameters used to describe $P_{700}^{+}PhQ^{-}_{B}$ taken from [114] may not be completely correct. With the assumption that the lifetime of fast phase ET is 20 ns, the lifetime for the slow phase in the simulation for PsaA-A680N spectra is found to be 200 ns. Thus, the mutation does not affect the rate of ET from PhQ_{A}^{-} to F_x as expected.

In the bottom part of the Figure 6.3 the corresponding spectra and time traces for the PsaB-A660N mutant are presented. The data are very similar to the WT and from the shape of the early signal and the intensity of the absorptive feature at field position "b", it is clear that there is a significant amount of fast component of ET. However, the fitting results give a fraction of 31% for the B-branch ET, which indicates that the amount of fast component is smaller in PsaB-A660N than WT (51%). This result suggests that the PsaB-A660N mutation produces

the opposite effect to the PsaA-A680N mutation and decreases the relative amount of B-branch ET. With the assumption that the lifetime of fast phase ET is 20 ns, the lifetime for the slow phase in the simulation for PsaB-A660N spectra is found to be 240 ns, which is slightly longer than found in WT and PsaA-A680N samples but almost within the estimated uncertainty of ±30 ns.

6.3 Low Temperature X-band Transient EPR Results

In Figure 6.4 the X-band transient EPR spectra of the samples taken at 80 K are presented. In this figure, the amplitudes are normalized so that the low field emissive peak is the same for all three samples. As can be seen, the spectra of the two mutants share similarities and differences. The main difference is that in the PsaA-A680N spectrum the high field emission is weak and the shoulders due to hyperfine coupling are more pronounced. We saw this effect in the corresponding spectrum of the PsaA-M688H mutant discussed in the previous chapter. In the case of the PsaA-M688H mutant, the mutation blocks ET in the A-branch and the spectrum is due to $P_{700}^{+}PhQ_{B}^{-}$. Consistent with the room temperature EPR data, the PsaA-A680N spectrum appears to have a greater contribution from the B-branch radical pair, and the shape of the WT spectrum is between that of the two mutants. The two RP spectra differ because of the different orientations of the dipolar coupling vector relative to the g-tensor of P_{700}^{+}. The better resolution of the contributions from P_{700}^{+} and PhQ^{-} at higher field, the differences in the spectra should be more pronounced at Q-band.

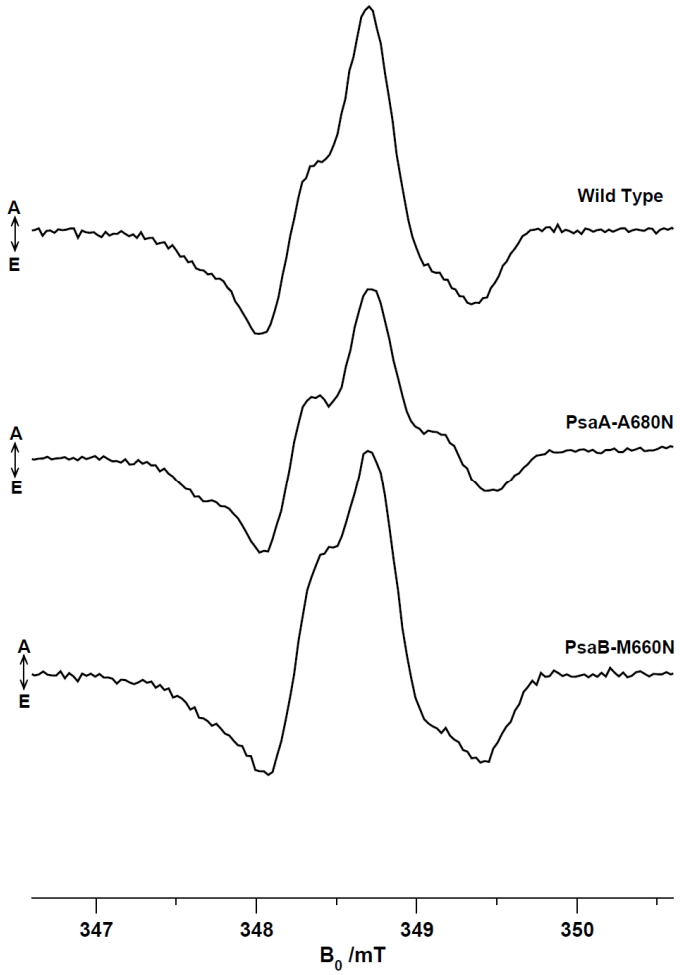

Figure 6.4: Spin polarized X-band spectrum for Wild Type, PsaA-A680N and PsaB-A660N of *C. reinhardtii* at 80 K.

6.4 Low Temperature Q-band Transient EPR Results

Figure 6.5 shows the low temperature transient EPR spectrum at Q-band for WT, PsaA-A680N and PsaB-A660N from top to bottom, respectively. In Figure 6.6 the predicted theoretical spectra for the A and B branch RPs are represented as well. All of the spectra are normalized so that the emissive signals in the low field region have the same amplitude. The Q-band results are similar to the X-band result and despite the poor signal to noise for the PsaA-A680N spectrum it can be seen that the spectra are the same in the low field region. The spectrum for the PsaA-A680N and PsaB-A660N in this region are very close to the spectra that have been reported in other point mutation studies [92, 123] if the

A-mutant spectrum was dominated by the B-branch radical pair and the B-mutant spectrum was dominated by the A-branch RP.

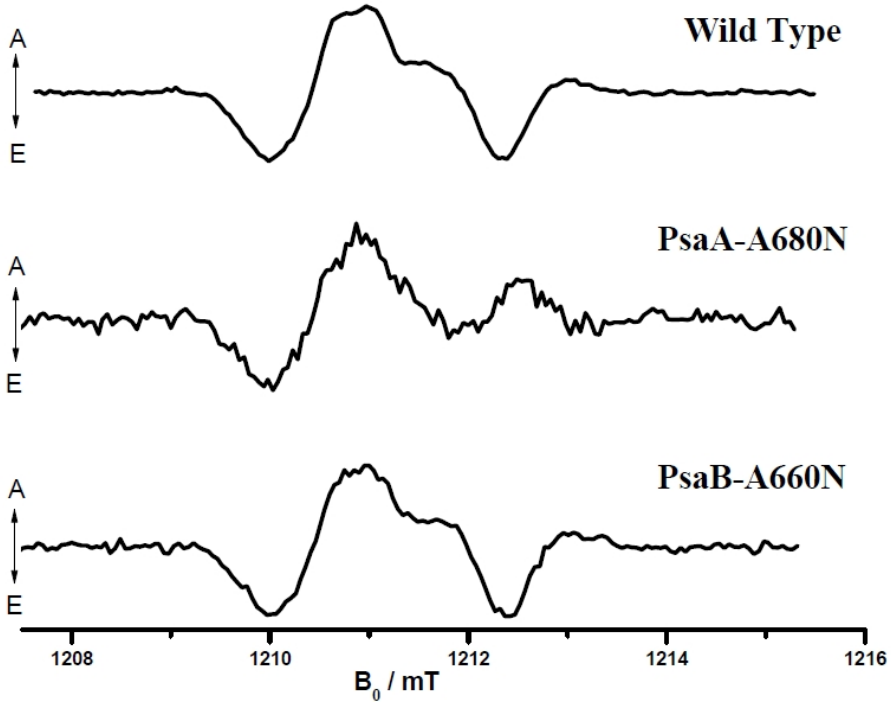

Figure 6.5: Polarized Q-band Transient EPR for Wild Type, PsaA-A680N and PsaB-A660N of *C. reinhardtii* at 80 K

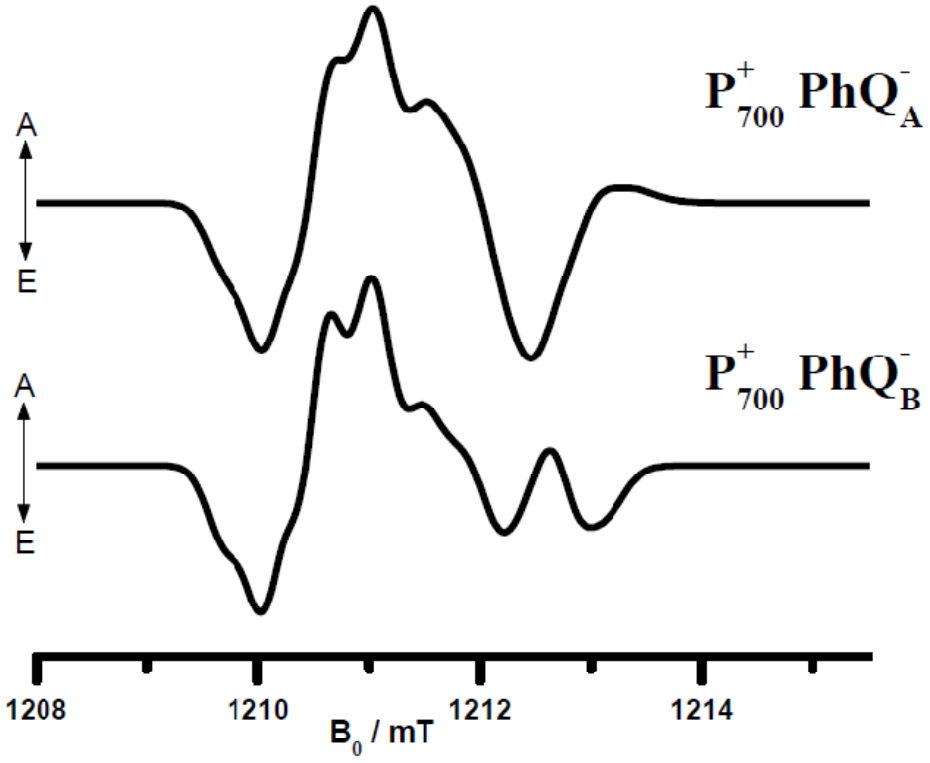

Figure 6.6: Theoretical prediction for Q-band A and B branch ET spectra. The parameters used to simulate $P_{700}^{+}PhQ_A^{-}$ and $P_{700}^{+}PhQ_B^{-}$ are obtained from[121, 122]**, respectively**

As was the case for the room temperature and low temperature X-band spectra the spectra for the WT and the PsaB-A660N mutant are almost identical while the PsaA-A680N mutant is different. Qualitatively, the difference between the two theoretical spectra (Figure 6.5) is similar to that observed experimentally again suggesting that the relative contribution of the A and B branch radical pairs is altered by the mutations.

As the final test of this hypothesis we have carried out OOP-ESEEM experiments on the two mutants.

6.4 Low Temperature OOP-ESEEM Results

In the Figure 6.7 the OOP-ESEEM spectra for WT, PsaA-A680N and PsaB-A660N mutants along with calculated traces fitted to the data are shown. In the figure, solid lines represent the experimental spectra and their corresponding

fitting curves are represented with the same color by dashed lines. Based on the OOP-ESEEM results for the histidine mutants discussed in the previous chapter, we expect that the PsaA-A680N OOP-ESEEM trace would show a higher modulation frequency. The black, red and blue vertical lines show the position of the minimum near τ = 750 ns for the three modulation curves, From the position of the vertical lines we can see that the oscillation frequency is highest for the PsaA-A680N mutant and lowest for the PsaB-M668H mutant and the WT lies between the two mutants. In the calculated modulation curves a mixture of the A-Branch and B-branch contribution were used as in the previous chapter. The ratios of the A- and B-branch contributions obtained from the best fits to the data were 15:85 for the PsaA-A680N mutant, 70:30 for the PsaB-A660N mutant and 60:40 for the wild type.

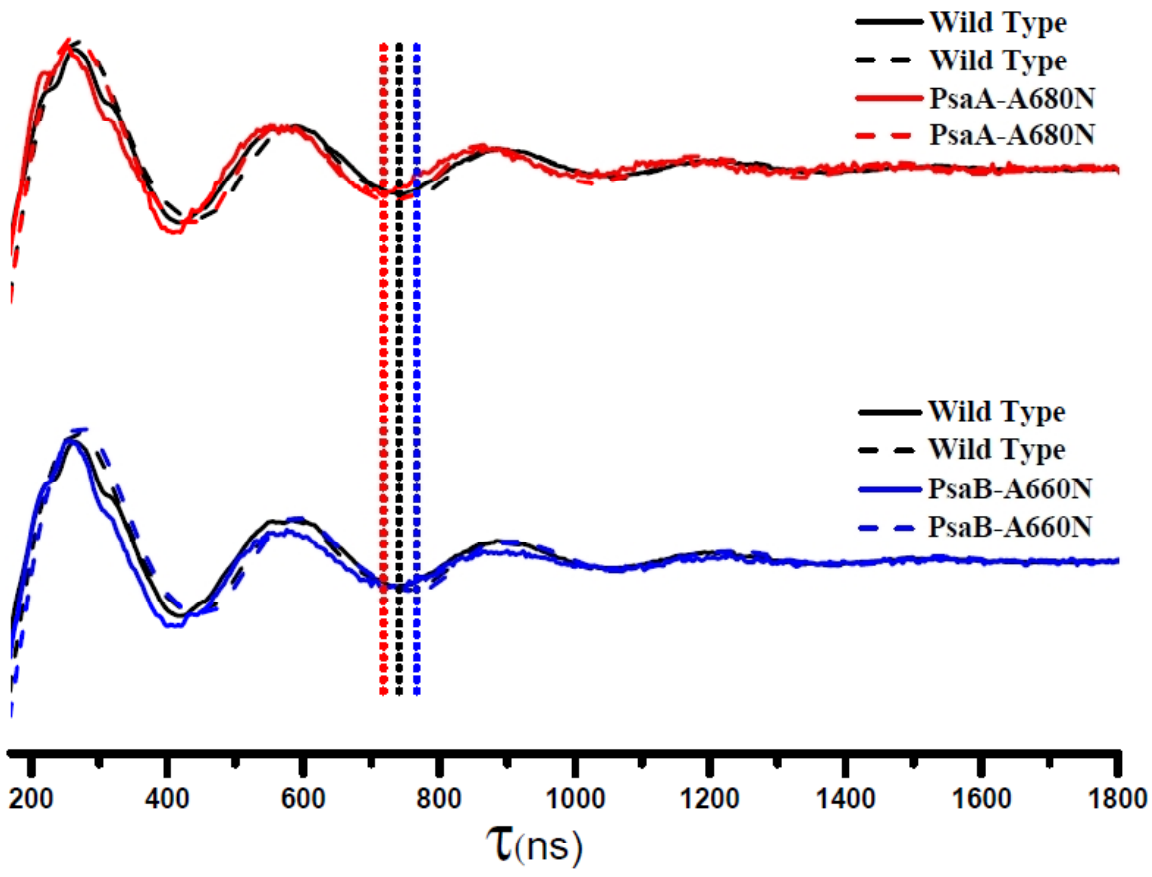

Figure 6.7: OOP-ESEEM traces for WT, PsaA-A680N and PsaB-A660N and their corresponding fitting traces.

6.5 Summary of the results

In conclusion, the different X-band EPR spectra at room temperature for the two samples and their different time evolutions is an indication that replacement of alanine residues PsaA-A660 and PsaB-A640 with asparagine causes a decrease in the relative amount of ET in the branch carrying the mutation. The low temperature spectra at X-band and Q-band also show differences consistent with alteration in the relative amounts of $P_{700}^{+}PhQ_A^{-}$ and $P_{700}^{+}PhQ_B^{-}$. The different frequencies observed in the OOP-ESEEM modulation curves of the two mutants indicated that a mixture of the dipolar couplings expected for the $P_{700}^{+}PhQ_A^{-}$ and $P_{700}^{+}PhQ_B^{-}$ RPs is present and that the mutations affect the relative amounts of the two radical pairs. Although the EPR data show that the mutations alter the relative use of each branch, it is not possible to strictly state whether ET is simply being blocked in the branch with mutation or whether electrons are being re-directed into the other branch. One way to distinguish these two possibilities is to measure the absolute intensity of the signal from a given branch to see if it is increasing or decreasing. However, this is very difficult to do in a transient EPR experiment because there is no internal reference signal we can use to normalize the data and changes in the local environments of the radicals in the mutants can alter the intensity of the spectrum. But, in transient absorbance data, the bleaching of the P_{700} absorbance can be used as an internal reference and the absorbance is less sensitive to changes in the local environment. The transient absorbance experiments on PsaA-A660N and PsaB-A640N are in progress to find out whether the mutation blocked the ET in the branch carrying the mutation or electrons are being redirected into other branch [120].

7 Transient EPR Studies of the Oxidation of Heliobacterial Reaction Centers

Heliobacillus (*Hb*) *mobilis* is an anaerobic photosynthetic organism. The color of a culture of anaerobic *Hb* is brown and is called "Braunstoff" (German word for "brown substance" [125]). As mentioned in the introduction section, the unique pigment bacteriochlorophyll *g* (BChl *g*) is found in this bacterium. Two molecules of BChl *g*′ (the 13^2 epimer of BChl *g*) are thought to be the symmetric electron donor [48]. The primary electron acceptor is 8^1-hydroxychlorophyll *a* (8^1-OH-Chl *a*) [48]. In the absorption spectrum of anaerobically grown *Hb. mobilis* shown in Figure 7.1 as the red curve, we can see there are two intense absorbance peaks at 570 and 798 nm corresponding to BChl *g* [126]. There is also a less intense peak at 670 nm which corresponds to 8^1-OH-Chl *a* [126]. When *Hb* cultures are exposed to oxygen in the presence of light their colour

changes gradually from brown to green. The green form of the culture is called "Grünstoff" (German for "green substance"). The absorption spectrum for the aerobic states of heliobacterial cells is the green trace in Figure 7.1. Here, we observe that the peak which is related to 8^1-OH-Chl *a* becomes more intense and the peaks related to BChl *g* become less intense. In fact the electron donor becomes spectroscopically equivalent to Chl *a*, which is found in PS I RCs [7]. It is well known that BChl *g* can isomerize to Chl a_F [127], in the presence of light and/or acid and this process is clearly occurring when *Hb* cultures are exposed to oxygen. In Figure 7.2, molecular structure of BChl *g*, 8^1-OH-Chl *a* and Chl a_F are shown. Little was known about the effect of the oxidation on the function of Grünstoff prior to an NMR study carried out on both Braunstoff and Grünstoff that demonstrated that under exposure to oxygen, light induced RPs are generated in Grünstoff as well as Braunstoff in *Hb*RCs [126]. However, the kinetics and quantum yield of ET in oxidized *Hb*RCs remain unknown. Here, we report a transient EPR study of the light-induced RPs in anaerobic and aerobic *Hb*RCs at X-band and Q-band. We will show that exposure to oxygen greatly reduces the yield of charge separation and shortens its lifetime.

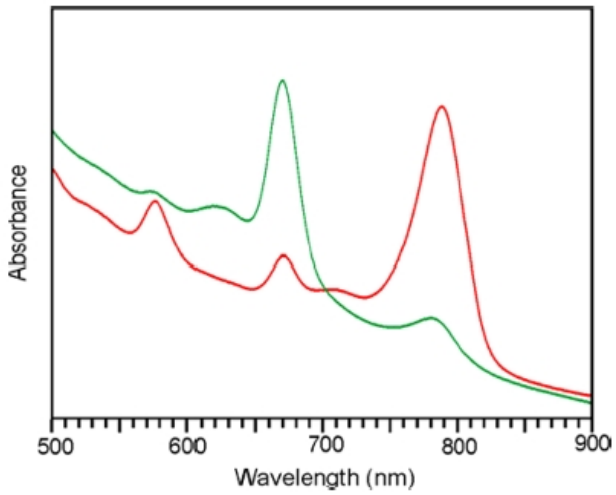

Figure 7.1: Absorption spectra of anaerobic (red) and aerobic (green) of heliobacterial cells [126]**. Used with permission.**

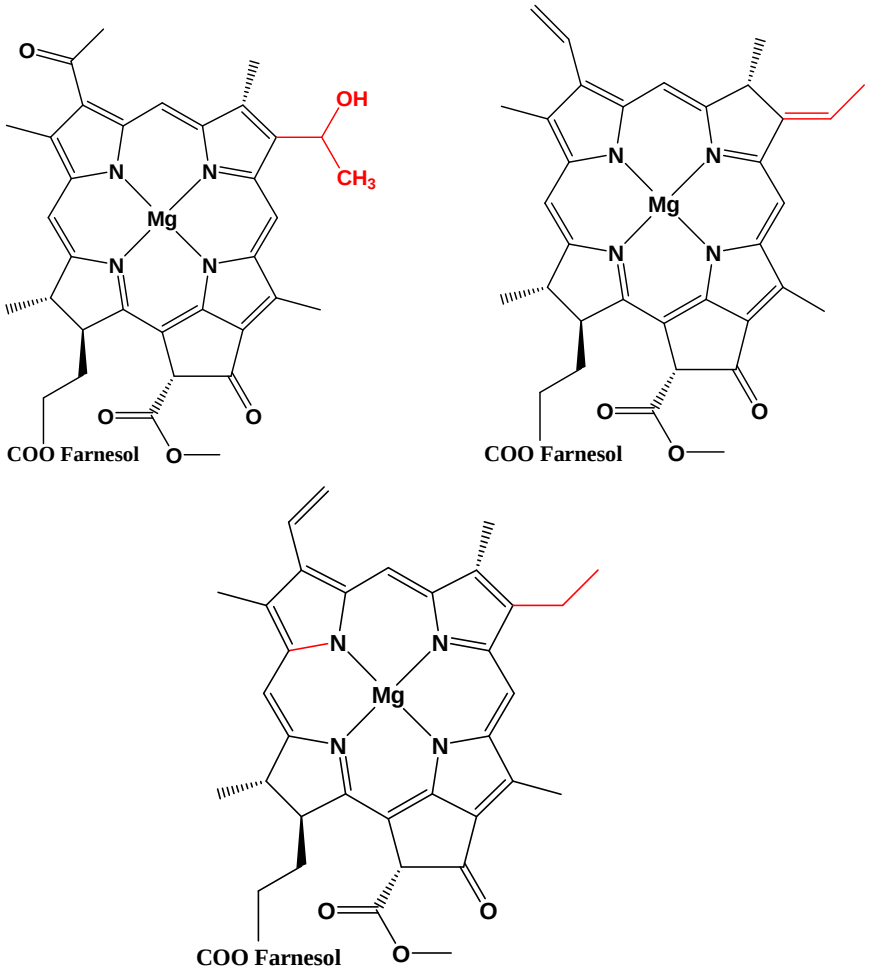

Figure 7.2: Chemical structure of 8[1]-OH Chl *a* (top left) and BChl *g* (top right) and Chl a_F (bottom).

7.1 Transient EPR Setup at X-band and Q-band

The transient EPR X-band and Q-band setup is described in section 5.1. For studying the lifetime of P_{798}^{+} in each sample time/field datasets were collected as described in chapter 5 and 6 except that the field modulation technique was used to detect the signal and the output of the lock-in amplifier was digitized using the transient recorder.

*Hb*RCs were isolated under strictly anaerobic conditions and then exposed to oxygen. Samples of the *Hb*RCs were taken at five different time points during the exposure oxidation and frozen. The first sample (T_0) is anaerobic, the other four samples (T_1 T_2 T_3 and T_4) were exposed to oxygen for 2, 4, 8, and 12 hours respectively and frozen immediately. The frozen samples were stored in liquid nitrogen and were kept frozen when being transferred to the EPR spectrometer. All EPR data were collected at 80 K. The samples were provided by our collaborators Bryan Ferlez and John Golbeck at The Pennsylvania State University [128].

7.2 X-band and Q-band Transient EPR Results

In Figures 7.3 and 7.4 transient EPR spectra at X-band of anaerobic sample (T_0) and aerobic samples (T_1 to T_4) of *Hb*RCs at 80 K are shown. In Figure 7.3 the spectra are not normalized so that the changes of the signal intensity as the RCs are exposed to oxygen are apparent. It can be seen that as the sample is exposed to oxygen the signal intensity decreases. In Figures 7.4, the same spectra are normalized so that the absorptive signal have the same amplitude and the normalization factors, which are presented in Table 7.1, give a measure of the decrease in intensity. Comparison of the normalized spectra allows changes in the net polarization to be seen more easily. Corresponding Q-band spectra are shown in Figure 7.5. It should be noted that these spectra are of the state $P_{798}^{+}Fx^{-}$ and only the contribution from P_{798}^{+} is observed. In addition, the spectra show net absorptive polarization that is due to singlet-triplet mixing during the 700 ps lifetime of $P^{+}A_0^{-}$ [52, 63]. In Figures 7.4 and 7.5 the relative intensity of the emissive part of the signal increases as the samples are oxidized indicating that

the relative amplitude of the net polarization decreases. At Q-band the rate of singlet-triplet mixing is faster and hence the net polarization is greater as can be seen in the spectrum at T_0 in Figure7.5. However, the decrease in intensity and net polarization as the sample is oxidized are essentially the same as observed at X-band. Careful inspection of the spectra in Figures 7.4 and 7.5 also shows that the line-width becomes larger during the oxidation.

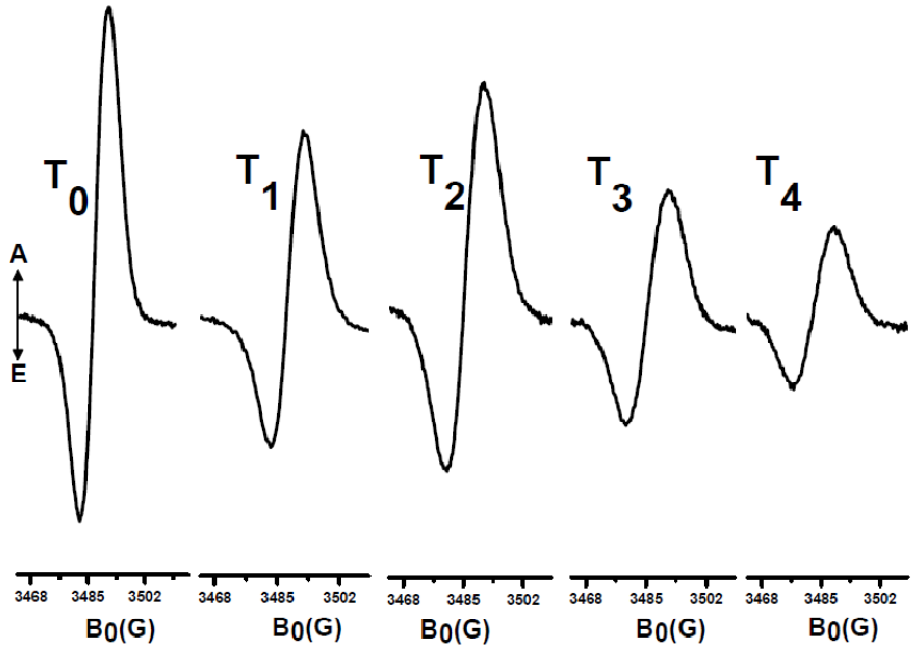

Figure 7.3 Transient EPR spectra at X-band of aerobic sample (T_0) and anaerobic samples (T_1 to T_4) of *Hb*RCs at 80 K, These spectra are not normalized to show the changes of the signal intensity as the RCs are exposed to oxygen.

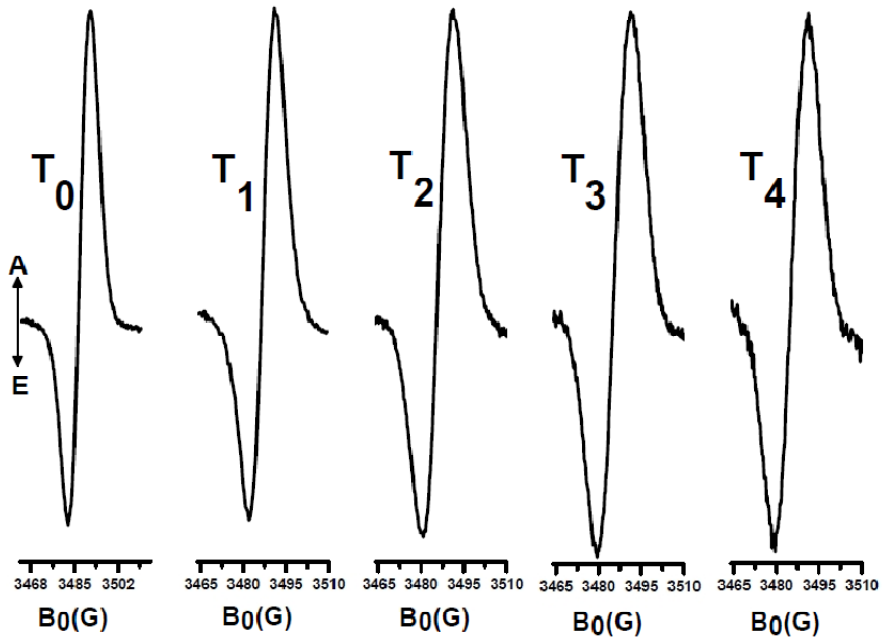

Figure 7.4: Transient EPR spectra at X-band of aerobic sample (T_0) and anaerobic samples (T_1 to T_4) of *Hb*RCs at 80 K using direct detection of EPR signals. These spectra are normalized to the absorptive signal of T_0 .

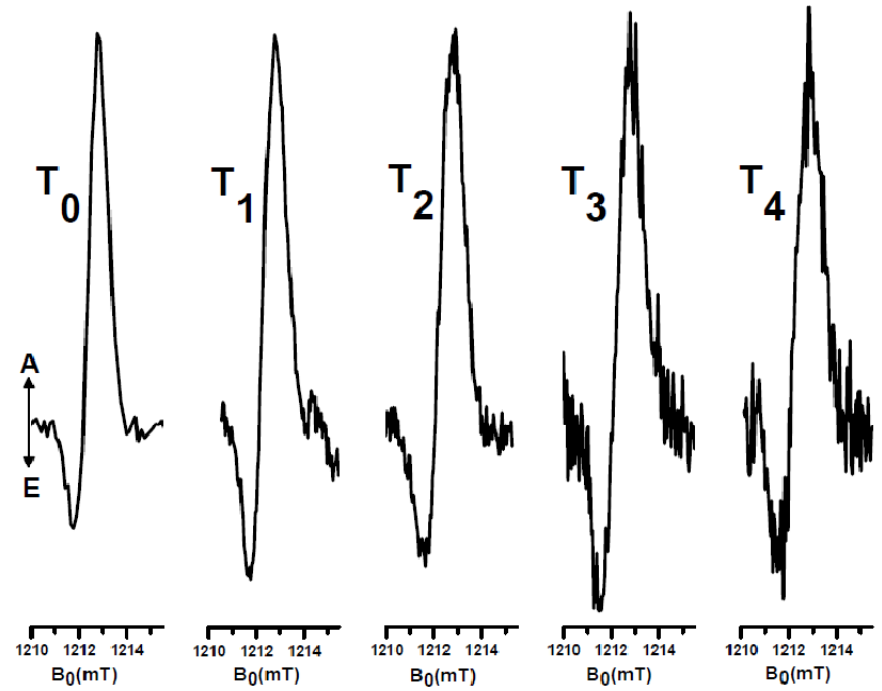

Figure 7.5: Transient EPR spectra at Q-band of aerobic sample (T_0) and anaerobic samples (T_1 to T_4) of *Hb*RCs at 80 K using direct detection of signals. These spectra are normalized to the absorptive signal of T_0 .

Sample	X-band Normalization Factor	Q-band Normalization Factor
T_0	1	1
T_1	1.6	1.2
T_2	1.4	2.3
T_3	2.3	3.9
T_4	3.5	4.3

Table 7.1: Normalization factor for the X-band and Q-band spectra

As mentioned in chapter 3, the decay of EPR signals using direct detection is due to relaxation of spin polarization. T_0 measure the lifetime of charge separation, the decay of EPR signal using field modulation detection can be used. In Figure 7.6, the decay of the field modulation detected EPR signals of the samples due to back reaction of $P_{798}^{+}F_x^{-}$ are shown. The time traces are normalized to have the same amplitude, and the normalization factors are the same as obtained for the direct detection spin polarized X-band transient EPR spectra given in Table 7.1.

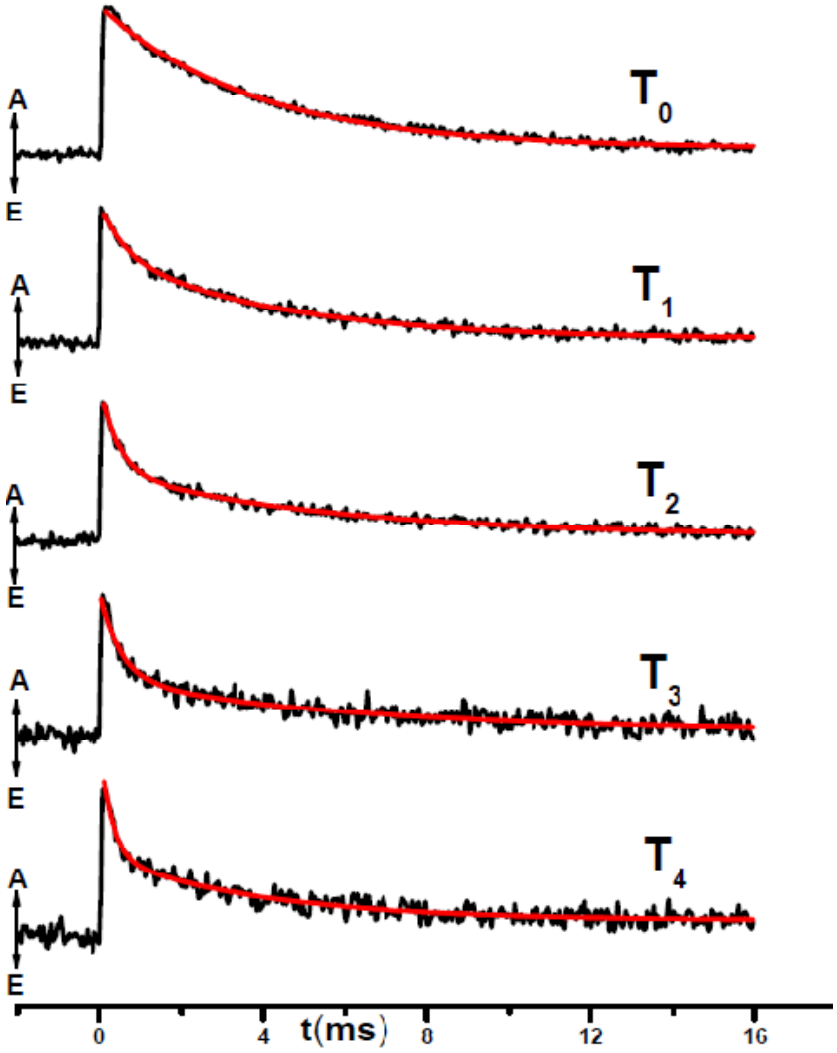

Figure 7.6: Decays of the X-band Transient EPR signal at 80 K using field modulation detection. The red traces were obtained by fitting eqn. 7.1 to the experimental data.

The red curves in Figure 7.6 were obtained by fitting the bi-exponential decay function,

$$y = A_0[x \exp\left(-\frac{t}{t_1}\right) + (1 - x) \exp\left(-\frac{t}{t_2}\right)] \qquad (7.1)$$

to the data. In eqn. 7.1 A_0 is the amplitude of the absorptive signal for the intact sample "T_0".

Sample	x(± 0.05)	t_1(ms)	(1-x)	t_2(ms)
T_0	1.00	3.7	0.00	0.0
T_1	0.66	4.2	0.34	0.6
T_2	0.47	5.5	0.53	0.5
T_3	0.34	5.3	0.66	0.4
T_4	0.42	4.0	0.58	0.3

Table 7.2: The parameters used to simulate the decays of the spectrum presented in Figure 7.6. The error in t_1 and t_2 is 0.1 ms.

The amplitudes and decay constants for each trace are presented in Table 7.2. As can be seen, the fitting function for the anaerobic sample "T_0" is mono-exponential and for the other samples the traces are bi-exponential. The lifetimes of the two components are roughly the same in all of the samples but their relative amplitudes change. The amplitude of slow component observed in the anaerobic sample becomes smaller as the samples exposed longer to oxygen. The amplitude of the other fraction, which can be assigned to back reaction in RCs that have been partially oxidized, becomes greater up to time point T_3 and then decreases slightly. Moreover, the decay constant related to aerobic ET is faster than the anaerobic ET by one order of magnitude.

7.3 Discussion on the Results

When the *Hb*RCs are exposed to oxygen, we observe some changes experimentally. First of all, the colour turns from brown to green. Second, the EPR signals get weaker. Third, the backreaction kinetics change and become bi-exponential with two different decay times, one component is faster than that in the intact sample and the other has the same lifetime. Fourth, the line-width of the EPR spectrum both at Q-band and X-band becomes larger. Finally, the amount of net polarization in the transient EPR spectra decreases.

As mentioned before, the change in color based on the absorbance spectra in the Figure7.1 can be interpreted as the oxidation of BChl g to Chl a_F when the intact sample is exposed to oxygen. The weaker EPR signal indicates that some of the RCs become non-functional when the BChl g and BChl g' cofactors are

oxidized. However, alteration of the kinetics and EPR properties of the remaining signal means that some RCs are still partially functional. This can be most easily understood as the result of oxidation of some, but not all, of the BChl *g* and BChl *g′*. The fact that the EPR spectra are broadened when the RCs are exposed to oxygen means that unresolved hyperfine couplings of P_{798}^{+} are stronger. Changes in the back reaction kinetics indicate that the redox potentials of P_{798}^{+} and/or F_x are altered. Finally, weaker net polarization means that the spin dynamics of the precursor state $P_{798}^{+}A_0^{-}$ is changed. We do not expect 8^1-OH-Chl *a*, which is A_0 in the *Hb*RCs, and F_x to be affected by exposure to oxygen. Thus, the only candidates for oxidation in the ET chain are the two BChl *g′* molecules of P_{798}. However, potentially accessory chlorophylls may present in *Hb*RCs like in PS I, PS II and bRCs and they could also be oxidized.

We see that if all BChl *g* and BChl *g′* molecules present in the *Hb*RC are oxidized they become non-functional and as a result EPR silent. For the intermediate states in which the RCs are still functional, the most likely scenario is that only one of the two BChl *g′* molecules that make up P_{798}^{+} is oxidized. In this scenario the larger line-width in the EPR spectrum of the aerobic samples compared to anaerobic ones can be interpreted as well. In the anaerobic RCs the unpaired electron on P_{798}^{+} is delocalized over two BChl *g′* molecules of the homodimer. If one these were to become oxidized, P_{798} would become a heterodimer and the unpaired electron would probably become localized on one of the two Chls. As a result, the hyperfine couplings would become greater as a result of localization of the unpaired electrons.

By looking at eqn. 4.3, we see that for a short-lived precursor such as $P_{798}^{+}A_0^{-}$ in *Hb*RCs, the net polarization generated by the spin dynamics in the precursor becomes smaller for a shorter lifetime, smaller g-value differences, and/or smaller spin-spin coupling. Eqn. 4.1 shows that stronger multiplet polarization arising from hyperfine contribution is observed when the linewidths in the precursor are larger. Experimentally, we are only able to determine the ratio of the multiplet to net polarization. However, some combination of these effects occurs in the partially oxidized *Hb*RCs. It is not possible to distinguish these

possibilities but it is most likely the change in the ratio of net to multiplet polarization is a result of a change in the linewidth of P_{798}^{+} and a change in the difference in the g values of P_{798}^{+} and A_0^{-}.

To test this hypothesis it would be useful to carry out high field EPR (W-band or higher frequencies) and ENDOR (Electron Nuclear Double Resonance) experiments to determine how the g-values and hyperfine couplings are changing. We note, however, that such experiments will be complicated by the fact that both intact and partially oxidized forms of P_{798}^{+} will be present.

8 Bibliography

[1] NASA, “Earth’s Energy Budget,” *National Aeronautics and Space Administration*. [Online]. Available: http://science-edu.larc.nasa.gov/energy_budget/.

[2] H.-W. Heldt and F. Heldt, *Plant Biochemistry*. Academic Press, 2005, p. 630.

[3] Y. Munekage, M. Hashimoto, C. Miyake, K. Tomizawa, T. Endo, M. Tasaka, and T. Shikanai, “Cyclic electron flow around photosystem I is essential for photosynthesis.,” *Nature*, vol. 429, no. 6991, pp. 579–82, Jun. 2004.

[4] M. Campbell and S. Farrell, *Biochemistry*. Cengage Learning, 2014, p. 864.

[5] R. E. Blankenship, D. M. Tiede, J. Barber, G. W. Brudvig, G. Fleming, M. Ghirardi, M. R. Gunner, W. Junge, D. M. Kramer, A. Melis, T. A. Moore, C. C. Moser, D. G. Nocera, A. J. Nozik, D. R. Ort, W. W. Parson, R. C. Prince, and R. T. Sayre, “Comparing photosynthetic and photovoltaic efficiencies and recognizing the potential for improvement.,” *Science*, vol. 332, no. 6031, pp. 805–9, May 2011.

[6] D. Gust, “Why Study Photosynthesis?,” 1996. [Online]. Available: (http://bioenergy.asu.edu/photosyn/study.html).

[7] M. Heinnickel and J. H. Golbeck, “Heliobacterial photosynthesis.,” *Photosynth. Res.*, vol. 92, no. 1, pp. 35–53, Apr. 2007.

[8] N. Nelson and A. Ben-Shem, “The structure of photosystem I and evolution of photosynthesis.,” *Bioessays*, vol. 27, no. 9, pp. 914–22, Sep. 2005.

[9] R. E. Blankenship and H. Hartman, “The origin and evolution of oxygenic photosynthesis,” *Trends Biochem. Sci.*, vol. 23, no. 3, pp. 94–97, Mar. 1998.

[10] R. E. Blankenship, “Origin and early evolution of photosynthesis.,” *Photosynth. Res.*, vol. 33, no. 2, pp. 91–111, Aug. 1992.

[11] J. Golbeck, “Structure and function of photosystem I,” *Annu. Rev. Plant Biol.*, 1992.

[12] W. Saenger, P. Jordan, and N. Krauß, “The assembly of protein subunits and cofactors in photosystem I,” *Curr. Opin. Struct. Biol.*, vol. 12, no. 2, pp. 244–254, Apr. 2002.

[13] K. Brettel and W. Leibl, “Electron transfer in photosystem I.,” *Biochim. Biophys. Acta*, vol. 1507, no. 1–3, pp. 100–14, Oct. 2001.

[14] P. Jordan, P. Fromme, H. T. Witt, O. Klukas, W. Saenger, and N. Krauss, “Three-dimensional structure of cyanobacterial photosystem I at 2.5 A resolution.,” *Nature*, vol. 411, no. 6840, pp. 909–17, Jun. 2001.

[15] N. Srinivasan and J. H. Golbeck, “Protein-cofactor interactions in bioenergetic complexes: the role of the A1A and A1B phylloquinones in Photosystem I.,” *Biochim. Biophys. Acta*, vol. 1787, no. 9, pp. 1057–88, Sep. 2009.

[16] I. V Shelaev, F. E. Gostev, M. D. Mamedov, O. M. Sarkisov, V. A. Nadtochenko, V. A. Shuvalov, and A. Y. Semenov, “Femtosecond primary charge separation in Synechocystis sp. PCC 6803 photosystem I.,” *Biochim. Biophys. Acta*, vol. 1797, no. 8, pp. 1410–20, Aug. 2010.

[17] M. G. Müller, J. Niklas, W. Lubitz, and A. R. Holzwarth, “Ultrafast transient absorption studies on Photosystem I reaction centers from Chlamydomonas reinhardtii. 1. A new interpretation of the energy trapping and early electron transfer steps in Photosystem I.,” *Biophys. J.*, vol. 85, no. 6, pp. 3899–922, Dec. 2003.

[18] A. R. Holzwarth, M. G. Müller, J. Niklas, and W. Lubitz, “Ultrafast transient absorption studies on photosystem I reaction centers from Chlamydomonas reinhardtii. 2: mutations near the P700 reaction center chlorophylls provide new insight into the nature of the primary electron donor.,” *Biophys. J.*, vol. 90, no. 2, pp. 552–65, Jan. 2006.

[19] G. Hastings, F. A. M. Kleinherenbrink, S. Lin, T. J. McHugh, and R. E. Blankenship, “Observation of the Reduction and Reoxidation of the Primary Electron Acceptor in Photosystem I,” *Biochemistry*, vol. 33, no. 11, pp. 3193–3200, Mar. 1994.

[20] B. Hecks, K. Wulf, J. Breton, W. Leibl, and H.-W. Trissl, “Primary Charge Separation in Photosystem I: A Two-Step Electrogenic Charge Separation

Connected with P700+A0- and P700+A1- Formation," *Biochemistry*, vol. 33, no. 29, pp. 8619–8624, Jul. 1994.

[21] K. Brettel and M. H. Vos, "Spectroscopic resolution of the picosecond reduction kinetics of the secondary electron acceptor A1 in photosystem I," *FEBS Lett.*, vol. 447, no. 2–3, pp. 315–317, Mar. 1999.

[22] S. Savikhin, W. Xu, P. Martinsson, P. R. Chitnis, and W. S. Struve, "Kinetics of Charge Separation and A 0 - → A 1 Electron Transfer in Photosystem I Reaction Centers †," *Biochemistry*, vol. 40, no. 31, pp. 9282–9290, Aug. 2001.

[23] A. van der Est, C. Bock, J. Golbeck, K. Brettel, P. Setif, and D. Stehlik, "Electron Transfer from the Acceptor A1 to the Iron-Sulfur Centers in Photosystem I As Studied by Transient EPR Spectroscopy," *Biochemistry*, vol. 33, no. 39, pp. 11789–11797, Oct. 1994.

[24] J. Lüneberg, P. Fromme, P. Jekow, and E. Schlodder, "Spectroscopic characterization of PS I core complexes from thermophilic Synechococcus sp," *FEBS Lett.*, vol. 338, no. 2, pp. 197–202, Jan. 1994.

[25] C. H. Bock, A. J. van der Est, K. Brettel, and D. Stehlik, "Nanosecond electron transfer kinetics in photosystem I as obtained from transient EPR at room temperature," *FEBS Lett.*, vol. 247, no. 1, pp. 91–96, Apr. 1989.

[26] P. Setif and K. Brettel, "Forward electron transfer from phylloquinone A1 to iron-sulfur centers in spinach photosystem I," *Biochemistry*, vol. 32, no. 31, pp. 7846–7854, Aug. 1993.

[27] E. Schlodder, K. Falkenberg, M. Gergeleit, and K. Brettel, "Temperature dependence of forward and reverse electron transfer from A1-, the reduced secondary electron acceptor in photosystem I.," *Biochemistry*, vol. 37, no. 26, pp. 9466–76, Jun. 1998.

[28] P. Joliot and A. Joliot, "In vivo analysis of the electron transfer within photosystem I: are the two phylloquinones involved?," *Biochemistry*, vol. 38, no. 34, pp. 11130–6, Aug. 1999.

[29] K. Redding and A. van der Est, "The Directionality of Electron Transport in Photosystem I," *Adv. Photosynth. Respir.*, vol. 4, pp. 413–437, 2006.

[30] K. Brettel and J. H. Golbeck, "Spectral and kinetic characterization of electron acceptor A1 in a Photosystem I core devoid of iron-sulfur centers F X, F B and F A.," *Photosynth. Res.*, vol. 45, no. 3, pp. 183–93, Sep. 1995.

[31] I. Vassiliev, "Iron–sulfur clusters in type I reaction centers," *Biochim. Biophys. Acta - Bioenerg.*, vol. 1507, no. 1–3, pp. 139–160, Oct. 2001.

[32] M. Byrdin, S. Santabarbara, F. Gu, W. V Fairclough, P. Heathcote, K. Redding, and F. Rappaport, “Assignment of a kinetic component to electron transfer between iron-sulfur clusters F(X) and F(A/B) of Photosystem I.,” *Biochim. Biophys. Acta*, vol. 1757, no. 11, pp. 1529–38, Nov. 2006.

[33] K. Brettel, “Electron transfer in photosystem I,” *Biochim. Biophys. Acta - Bioenerg.*, vol. 1507, no. 1–3, pp. 100–114, Oct. 2001.

[34] A. van derEst, “Electron Transfer Involving Phylloquinone in Photosystem I,” *Adv. Photosynth. Respir.*, vol. 24, pp. 387–411, 2006.

[35] P. Heathcote, M. R. Jones, and P. K. Fyfe, “Type I photosynthetic reaction centres: structure and function.,” *Philos. Trans. R. Soc. Lond. B. Biol. Sci.*, vol. 358, no. 1429, pp. 231–43, Jan. 2003.

[36] C. Kirmaier and D. Holten, “Primary photochemistry of reaction centers from the photosynthetic purple bacteria.,” *Photosynth. Res.*, vol. 13, no. 3, pp. 225–60, Sep. 1987.

[37] A. R. Holzwarth, M. G. Müller, M. Reus, M. Nowaczyk, J. Sander, and M. Rögner, “Kinetics and mechanism of electron transfer in intact photosystem II and in the isolated reaction center: pheophytin is the primary electron acceptor.,” *Proc. Natl. Acad. Sci. U. S. A.*, vol. 103, no. 18, pp. 6895–900, May 2006.

[38] J. H. Golbeck, “Chapter 3 Photosynthetic Reaction So little time , so much to do,” in *Biophysics Textbook On Line*, On Line.

[39] J. Deisenhofer and H. Michel, “Nobel lecture. The photosynthetic reaction centre from the purple bacterium Rhodopseudomonas viridis.,” *EMBO J.*, vol. 8, no. 8, pp. 2149–70, Aug. 1989.

[40] P. Fromme, P. Jordan, and N. Krauß, “Structure of photosystem I,” *Biochim. Biophys. Acta - Bioenerg.*, vol. 1507, no. 1–3, pp. 5–31, Oct. 2001.

[41] Y. Umena, K. Kawakami, J.-R. Shen, and N. Kamiya, “Crystal structure of oxygen-evolving photosystem II at a resolution of 1.9 Å.,” *Nature*, vol. 473, no. 7345, pp. 55–60, May 2011.

[42] H. W. Rémigy, H. Stahlberg, D. Fotiadis, S. A. Müller, B. Wolpensinger, A. Engel, G. Hauska, and G. Tsiotis, “The reaction center complex from the green sulfur bacterium Chlorobium tepidum: a structural analysis by scanning transmission electron microscopy.,” *J. Mol. Biol.*, vol. 290, no. 4, pp. 851–8, Jul. 1999.

[43] S. Neerken, “The antenna reaction center complex of heliobacteria: composition, energy conversion and electron transfer,” *Biochim. Biophys. Acta - Bioenerg.*, vol. 1507, no. 1–3, pp. 278–290, Oct. 2001.

[44] M. Madigan, “The family Heliobacteriaceae,” *The prokaryotes*, 2006.

[45] H. Brockmann and A. Lipinski, “Bacteriochlorophyll g. A new bacteriochlorophyll from Heliobacterium chlorum,” *Arch. Microbiol.*, vol. 136, no. 1, pp. 17–19, Oct. 1983.

[46] R. C. Fuller, S. G. Sprague, H. Gest, and R. E. Blankenship, “A unique photosynthetic reaction center from Heliobacterium chlorum,” *FEBS Lett.*, vol. 182, no. 2, pp. 345–349, Mar. 1985.

[47] A. M. Nuijs, R. J. v. Dorssen, L. N. M. Duysens, and J. Amesz, “Excited states and primary photochemical reactions in the photosynthetic bacterium Heliobacterium chlorum,” *Proc. Natl. Acad. Sci.*, vol. 82, no. 20, pp. 6865–6868, Oct. 1985.

[48] E. J. van de Meent, M. Kobayashi, C. Erkelens, P. A. van Veelen, J. Amesz, and T. Watanabe, “Identification of 81-hydroxychlorophyll a as a functional reaction center pigment in heliobacteria,” *Biochim. Biophys. Acta - Bioenerg.*, vol. 1058, no. 3, pp. 356–362, Jul. 1991.

[49] S. Lin, H. C. Chiou, F. A. Kleinherenbrink, and R. E. Blankenship, “Time-resolved spectroscopy of energy and electron transfer processes in the photosynthetic bacterium Heliobacillus mobilis,” *Biophys. J.*, vol. 66, no. 2, pp. 437–445, Feb. 1994.

[50] F. A. M. Kleinherenbrink, T. J. Aartsma, and J. Amesz, “Charge separation and formation of bacteriochlorophyll triplets in Heliobacterium chlorum,” *Biochim. Biophys. Acta - Bioenerg.*, vol. 1057, no. 3, pp. 346–352, May 1991.

[51] A. Hiraishi, “Occurrence of menaquinone as the sole isoprenoid quinone in the photosynthetic bacterium Heliobacterium chlorum,” *Arch. Microbiol.*, vol. 151, no. 4, pp. 378–379, Mar. 1989.

[52] K. Brettel, “Electron transfer in the heliobacterial reaction center: evidence against a quinone-type electron acceptor functioning analogous to A1 in photosystem I,” *Biochim. Biophys. Acta - Bioenerg.*, vol. 1363, no. 3, pp. 175–181, Mar. 1998.

[53] A. van der Est, C. Hager-Braun, W. Leibl, G. Hauska, and D. Stehlik, “Transient electron paramagnetic resonance spectroscopy on green-sulfur bacteria and heliobacteria at two microwave frequencies,” *Biochim. Biophys. Acta - Bioenerg.*, vol. 1409, no. 2, pp. 87–98, Dec. 1998.

[54] T. Kondo, M. Matsuoka, C. Azai, H. Mino, H. Oh-oka, and S. Itoh, “Reaction of A 1 -menaquinone in Type I Reaction Center of Heliobacterium Modesticaldum at Cryogenic Temperature,” pp. 21–24, 2013.

[55] M. Heinnickel, R. Agalarov, N. Svensen, C. Krebs, and J. H. Golbeck, “Identification of FX in the heliobacterial reaction center as a [4Fe-4S] cluster with an S = 3/2 ground spin state.,” *Biochemistry*, vol. 45, no. 21, pp. 6756–64, May 2006.

[56] W. Nitschke, P. Setif, U. Liebl, U. Feiler, and A. W. Rutherford, “Reaction center photochemistry of Heliobacterium chlorum,” *Biochemistry*, vol. 29, no. 50, pp. 11079–11088, Dec. 1990.

[57] H. Oh-oka, “Type 1 reaction center of photosynthetic heliobacteria.,” *Photochem. Photobiol.*, vol. 83, no. 1, pp. 177–86, 2007.

[58] S. P. Romberger and J. H. Golbeck, “The bound iron-sulfur clusters of type-I homodimeric reaction centers.,” *Photosynth. Res.*, vol. 104, no. 2–3, pp. 333–46, Jun. 2010.

[59] S. P. Romberger, C. Castro, Y. Sun, and J. H. Golbeck, “Identification and characterization of PshBII, a second FA/FB-containing polypeptide in the photosynthetic reaction center of Heliobacterium modesticaldum.,” *Photosynth. Res.*, vol. 104, no. 2–3, pp. 293–303, Jun. 2010.

[60] Y. E. Kandrashkin, K. M. Salikhov, a. Est, and D. Stehlik, “Electron spin polarization in consecutive spin-correlated radical Pairs: Application to short-lived and long-lived precursors in type 1 photosynthetic reaction centres,” *Appl. Magn. Reson.*, vol. 15, no. 3–4, pp. 417–447, Dec. 1998.

[61] Y. E. Kandrashkin, K. M. Salikhov, and D. Stehlik, “Spin dynamics and EPR spectra of consecutive spin-correlated radical pairs. Model calculations,” *Appl. Magn. Reson.*, vol. 12, no. 2–3, pp. 141–166, Mar. 1997.

[62] A. van der E. Y. K. Kandarshkin, “Applied Magnetic Resonance Time-Resolved EPR Spectroscopy of Photosynthetic Reaction Centers : from Theory to Experiment,” vol. 122, pp. 105–122, 2007.

[63] M. Brustolon, *Electron Paramagnetic Resonance: A Practitioner’s Toolkit (Google eBook)*. John Wiley & Sons, 2009, p. 608.

[64] a van der Est, “Light-induced spin polarization in type I photosynthetic reaction centres.,” *Biochim. Biophys. Acta*, vol. 1507, no. 1–3, pp. 212–25, Oct. 2001.

[65] J. B. Pedersen, “Determination of the primary reactions of photosynthesis from transient ESR signals,” *FEBS Lett.*, vol. 97, no. 2, pp. 305 – 310.

[66] J. R. Norris, A. L. Morris, M. C. Thurnauer, and J. Tang, “A general model of electron spin polarization arising from the interactions within radical pairs,” *J. Chem. Phys.*, vol. 92, no. 7, p. 4239, Apr. 1990.

[67] A. L. Morris, S. W. Snyder, Y. Zhang, J. Tang, M. C. Thurnauer, P. L. Dutton, D. E. Robertson, and M. R. Gunner, “Electron Spin Polarization Model Applied to Sequential Electron Transfer in Iron-Containing Photosynthetic Bacterial Reaction Centers with Different Quinones as QA,” *J. Phys. Chem.*, vol. 99, no. 11, pp. 3854–3866, Mar. 1995.

[68] P. J. HORE, “RESEARCH NOTE Transfer of spin correlation between radical pairs in the initial steps of photosynthetic energy conversion,” *Mol. Phys.*, vol. 89, no. 4, pp. 1195–1202, Nov. 1996.

[69] B. Boudreaux, F. MacMillan, C. Teutloff, R. Agalarov, F. Gu, S. Grimaldi, R. Bittl, K. Brettel, and K. Redding, “Mutations in both sides of the photosystem I reaction center identify the phylloquinone observed by electron paramagnetic resonance spectroscopy.,” *J. Biol. Chem.*, vol. 276, no. 40, pp. 37299–306, Oct. 2001.

[70] W. Fairclough, M. Evans, S. Purton, S. Rigby, and P. Heathcote, “Site-directed mutagenesis of PsaA:M684 in Chlamydomonas reinhardtii,” *Sci. Access*, vol. 3, no. 1.

[71] W. V. Fairclough, A. Forsyth, M. C. W. Evans, S. E. J. Rigby, S. Purton, and P. Heathcote, “Bidirectional electron transfer in photosystem I: electron transfer on the PsaA side is not essential for phototrophic growth in Chlamydomonas,” *Biochim. Biophys. Acta - Bioenerg.*, vol. 1606, no. 1–3, pp. 43–55, Sep. 2003.

[72] M. Guergova-Kuras, B. Boudreaux, A. Joliot, P. Joliot, and K. Redding, “Evidence for two active branches for electron transfer in photosystem I.,” *Proc. Natl. Acad. Sci. U. S. A.*, vol. 98, no. 8, pp. 4437–42, Apr. 2001.

[73] W. Xu, P. R. Chitnis, A. Valieva, A. van der Est, K. Brettel, M. Guergova-Kuras, Y. N. Pushkar, S. G. Zech, D. Stehlik, G. Shen, B. Zybailov, and J. H. Golbeck, “Electron transfer in cyanobacterial photosystem I: II. Determination of forward electron transfer rates of site-directed mutants in a putative electron transfer pathway from A0 through A1 to FX.,” *J. Biol. Chem.*, vol. 278, no. 30, pp. 27876–87, Jul. 2003.

[74] W. Xu, P. Chitnis, A. Valieva, A. van der Est, Y. N. Pushkar, M. Krzystyniak, C. Teutloff, S. G. Zech, R. Bittl, D. Stehlik, B. Zybailov, G. Shen, and J. H. Golbeck, “Electron transfer in cyanobacterial photosystem I: I. Physiological and spectroscopic characterization of site-directed mutants in a putative electron transfer pathway from A0 through A1 to FX.,” *J. Biol. Chem.*, vol. 278, no. 30, pp. 27864–75, Jul. 2003.

[75] S. Santabarbara, I. Kuprov, W. V Fairclough, S. Purton, P. J. Hore, P. Heathcote, and M. C. W. Evans, “Bidirectional electron transfer in photosystem I: determination of two distances between P700+ and A1- in spin-correlated radical pairs.,” *Biochemistry*, vol. 44, no. 6, pp. 2119–28, Feb. 2005.

[76] K. Ali, S. Santabarbara, P. Heathcote, M. C. W. Evans, and S. Purton, “Bidirectional electron transfer in photosystem I: replacement of the symmetry-breaking tryptophan close to the PsaB-bound phylloquinone A1B with a glycine residue alters the redox properties of A1B and blocks forward electron transfer at cryogenic tempera,” *Biochim. Biophys. Acta*, vol. 1757, no. 12, pp. 1623–33, Dec. 2006.

[77] A. Zehetner, H. Scheer, P. Siffel, and F. Vacha, “Photosystem II reaction center with altered pigment-composition: reconstitution of a complex containing five chlorophyll a per two pheophytin a with modified chlorophylls,” *Biochim. Biophys. Acta - Bioenerg.*, vol. 1556, no. 1, pp. 21–28, Oct. 2002.

[78] J. A. Weil, J. R. Bolton, and J. E. Wertz, *Electron Paramagnetic Resonance: Elementary Theory and Practical Applications (Google eBook)*. John Wiley & Sons, 2007, p. 688.

[79] W. R. Hagen, *Biomolecular EPR Spectroscopy*. CRC Press, 2009.

[80] G. E. Uhlenbeck and S. Goudsmit, “Spinning Electrons and the Structure of Spectra,” *Nature*, vol. 117, no. 2938, pp. 264–265, Feb. 1926.

[81] W. Gerlach and O. Stern, “Das magnetische Moment des Silberatoms,” *Zeitschrift Phys.*, vol. 9, no. 1, pp. 353–355, Dec. 1922.

[82] P. H. Rieger, *Electron Spin Resonance: Analysis and Interpretation*. Royal Society of Chemistry, 2007, p. 173.

[83] N. M. Atherton, *Electron Spin Resonance, Volume 15*. Royal Society of Chemistry, 1996, p. 294.

[84] R. Haberkorn, M. E. Michel-Beyerle, and R. A. Marcus, “On spin-exchange and electron-transfer rates in bacterial photosynthesis,” *Proc. Natl. Acad. Sci.*, vol. 76, no. 9, pp. 4185–4188, Sep. 1979.

[85] D. Murphy, “EPR (Electron Paramagnetic Resonance) Spectroscopy of Polycrystalline Oxide Systems,” *ChemInform*, 2010.

[86] J. H. Golbeck and A. van der Est, “Electron Paramagnetic Resonance Spectroscopy,” in *Molecular Biophysics for the life sciences*, N. Allwell, L. Narhi, and I. Rayment Eds, Eds. New York: Springer, New York, 2013, pp. 175–213.

[87] A. van derEst, T. Prisner, R. Bittl, P. Fromme, W. Lubitz, and K. Mo, “Time-resolved X-, K-, and W-band EPR of the radical pair state of Photosystem I in comparison with in bacterial reaction centers,” *J. Phy. Chem*, vol. 10, no. 96, pp. 1437–1443, 1997.

[88] J. Tang, M. C. Thurnauer, and J. R. Norris, “Electron spin echo envelope modulation due to exchange and dipolar interactions in a spin-correlated radical pair,” *Chem. Phys. Lett.*, vol. 219, no. 3–4, pp. 283–290, Mar. 1994.

[89] M. T. Colvin, R. Carmieli, T. Miura, S. Richert, D. M. Gardner, A. L. Smeigh, S. M. Dyar, S. M. Conron, M. A. Ratner, and M. R. Wasielewski, “Electron spin polarization transfer from photogenerated spin-correlated radical pairs to a stable radical observer spin.,” *J. Phys. Chem. A*, vol. 117, no. 25, pp. 5314–25, Jun. 2013.

[90] A. ; J. G. Schweiger, *Principles of Pulse Electron Paramagnetic Resonance*. Oxford University Press, 2001, p. 604.

[91] G. Zwanenburg and P. J. Hore, “Analytical Theory of Electron-Spin-Echo Modulations in Correlated Radical Pairs,” *J. Magn. Reson. Ser. A*, vol. 114, no. 2, pp. 139–146, Jun. 1995.

[92] S. Weber, G. Kothe, and J. R. Norris, “Transient nutation electron spin resonance spectroscopy on spin-correlated radical pairs: A theoretical analysis on hyperfine-induced nuclear modulations,” *J. Chem. Phys.*, vol. 106, no. 15, p. 6248, Apr. 1997.

[93] G. Link, T. Berthold, M. Bechtold, J.-U. Weidner, E. Ohmes, J. Tang, O. Poluektov, L. Utschig, S. L. Schlesselman, M. C. Thurnauer, and G. Kothe, “Structure of the Radical Pair Intermediate in Photosystem I by High Time Resolution Multifrequency Electron Paramagnetic Resonance: Analysis of Quantum Beat Oscillations,” *J. Am. Chem. Soc.*, vol. 123, no. 18, pp. 4211–4222, May 2001.

[94] G. Kothe, S. Weber, E. Ohmes, M. C. Thurnauer, and J. R. Norris, “High Time Resolution Electron Paramagnetic Resonance of Light-Induced Radical Pairs in Photosynthetic Bacterial Reaction Centers: Observation of Quantum Beats,” *J. Am. Chem. Soc.*, vol. 116, no. 17, pp. 7729–7734, Aug. 1994.

[95] A. van der Est, “Transient EPR: using spin polarization in sequential radical pairs to study electron transfer in photosynthesis.,” *Photosynth. Res.*, vol. 102, no. 2–3, pp. 335–47.

[96] Y. E. Kandrashkin, W. Vollmann, D. Stehlik, K. Salikhov, and a. Van Der Est, “The magnetic field dependence of the electron spin polarization in consecutive spin correlated radical pairs in type I photosynthetic reaction centres,” *Mol. Phys.*, vol. 100, no. 9, pp. 1431–1443, May 2002.

[97] Y. E. Kandrashkin and A. Est, “Time-resolved EPR spectroscopy of photosynthetic reaction centers: from theory to experiment,” *Appl. Magn. Reson.*, vol. 31, no. 1–2, pp. 105–122, Mar. 2007.

[98] Z. Liu, H. Yan, K. Wang, T. Kuang, J. Zhang, L. Gui, X. An, and W. Chang, “Crystal structure of spinach major light-harvesting complex at 2.72 A resolution.,” *Nature*, vol. 428, no. 6980, pp. 287–92, Mar. 2004.

[99] N. Dashdorj, W. Xu, R. O. Cohen, J. H. Golbeck, and S. Savikhin, “Asymmetric electron transfer in cyanobacterial Photosystem I: charge separation and secondary electron transfer dynamics of mutations near the primary electron acceptor A0.,” *Biophys. J.*, vol. 88, no. 2, pp. 1238–49, Feb. 2005.

[100] Y. Li, A. van der Est, M. G. Lucas, V. M. Ramesh, F. Gu, A. Petrenko, S. Lin, A. N. Webber, F. Rappaport, and K. Redding, “Directing electron transfer within Photosystem I by breaking H-bonds in the cofactor branches.,” *Proc. Natl. Acad. Sci. U. S. A.*, vol. 103, no. 7, pp. 2144–9, Feb. 2006.

[101] J. Niklas, B. Epel, M. L. Antonkine, S. Sinnecker, M.-E. Pandelia, and W. Lubitz, “Electronic structure of the quinone radical anion A1*- of photosystem I investigated by advanced pulse EPR and ENDOR techniques.,” *J. Phys. Chem. B*, vol. 113, no. 30, pp. 10367–79, Jul. 2009.

[102] V. M. Ramesh, K. Gibasiewicz, S. Lin, S. E. Bingham, and A. N. Webber, “Bidirectional electron transfer in photosystem I: accumulation of A0- in A-side or B-side mutants of the axial ligand to chlorophyll A0.,” *Biochemistry*, vol. 43, no. 5, pp. 1369–75, Feb. 2004.

[103] V. M. Ramesh, K. Gibasiewicz, S. Lin, S. E. Bingham, and A. N. Webber, “Replacement of the methionine axial ligand to the primary electron acceptor A0 slows the A0- reoxidation dynamics in photosystem I.,” *Biochim. Biophys. Acta*, vol. 1767, no. 2, pp. 151–60, Feb. 2007.

[104] J. G. J. Sun, S. Hao, W. Xu, I. Shelaev, V. Nadtochenko, V. Shuvalov, A. Semenov, H. Gordon, A. van der Est, “M688HPsaA and M668HPsaB Variants of Synechocystis sp. PCC Form a Second H-Bond to the A1A and A1B Phylloquinones and a Coordination Bond to the A0A and A0B Chlorophylls,” *Biochim. Biophys. Acta,*, 2013.

[105] S. Santabarbara, I. Kuprov, O. Poluektov, A. Casal, C. A. Russell, S. Purton, and M. C. W. Evans, “Directionality of electron-transfer reactions in photosystem I of prokaryotes: universality of the bidirectional electron-transfer model.,” *J. Phys. Chem. B*, vol. 114, no. 46, pp. 15158–71, Nov. 2010.

[106] A. Savitsky, J. Niklas, J. H. Golbeck, K. Möbius, and W. Lubitz, “Orientation resolving dipolar high-field EPR spectroscopy on disordered solids: II. Structure of

spin-correlated radical pairs in photosystem I.," *J. Phys. Chem. B*, vol. 117, no. 38, pp. 11184–99, Sep. 2013.

[107] J. Sun, S. Hao, M. Radle, W. Xu, I. Shelaev, V. Nadtochenko, V. Shuvalov, A. Semenov, H. Gordon, A. van der Est, and J. H. Golbeck, "Evidence that histidine forms a coordination bond to the A0A and A0B chlorophylls and a second H-bond to the A1A and A1B phylloquinones in M688HPsaA and M668HPsaB variants of Synechocystis sp. PCC 6803.," *Biochim. Biophys. Acta*, Apr. 2014.

[108] M. D. McConnell, "Biochemical and biophysical studies of photosystem I in Chlamydomonas reinhardtii : directionality of electron transfer and state transitions," Arizona State University, 2008.

[109] M. McConnell, J. Sun, R. Siavashi, A. Webber, K. Redding, J. H. Golbeck, and A. van der Est, "Species Dependent Alteration of Electron Transfer in Photosystem I," *Manuscr. Prep.*

[110] S. Mula, M. D. McConnell, A. Ching, N. Zhao, H. L. Gordon, G. Hastings, K. E. Redding, and A. van der Est, "Introduction of a hydrogen bond between phylloquinone PhQ(A) and a threonine side-chain OH group in photosystem I.," *J. Phys. Chem. B*, vol. 116, no. 48, pp. 14008–16, Dec. 2012.

[111] I. P. Muhiuddin, P. Heathcote, S. Carter, S. Purton, S. E. J. Rigby, and M. C. W. Evans, "Evidence from time resolved studies of the P700+/A1− radical pair for photosynthetic electron transfer on both the PsaA and PsaB branches of the photosystem I reaction centre," *FEBS Lett.*, vol. 503, no. 1, pp. 56–60, Aug. 2001.

[112] H. Käss, P. Fromme, H. T. Witt, and W. Lubitz, "Orientation and Electronic Structure of the Primary Donor Radical Cation in Photosystem I: A Single Crystals EPR and ENDOR Study," *J. Phys. Chem. B*, vol. 105, no. 6, pp. 1225–1239, Feb. 2001.

[113] S. Santabarbara, L. Galuppini, and A. P. Casazza, "Bidirectional electron transfer in the reaction centre of photosystem I.," *J. Integr. Plant Biol.*, vol. 52, no. 8, pp. 735–49, Aug. 2010.

[114] G. Link, T. Berthold, M. Bechtold, E. Ohmes, J. Tang, O. Poluektov, L. Utschig, S. L. Schlesselman, M. C. Thurnauer, and G. Kothe, "Structure of the P700 + A1 - Radical Pair Intermediate in Photosystem I by High Time Resolution Multifrequency Electron Paramagnetic Resonance: Analysis of Quantum Beat Oscillations," no. 8, pp. 4211–4222, 2001.

[115] T. Berthold, E. D. von Gromoff, S. Santabarbara, P. Stehle, G. Link, O. G. Poluektov, P. Heathcote, C. F. Beck, M. C. Thurnauer, and G. Kothe, "Exploring the electron transfer pathways in photosystem I by high-time-resolution electron paramagnetic resonance: observation of the B-side radical pair P700(+)A1B(-) in

whole cells of the deuterated green alga Chlamydomonas reinhardtii at cryogenic temp," *J. Am. Chem. Soc.*, vol. 134, no. 12, pp. 5563–76, Mar. 2012.

[116] S. Mula, A. Savitsky, K. Möbius, W. Lubitz, J. H. Golbeck, M. D. Mamedov, A. Y. Semenov, and A. van der Est, "Incorporation of a high potential quinone reveals that electron transfer in Photosystem I becomes highly asymmetric at low temperature.," *Photochem. Photobiol. Sci.*, vol. 11, no. 6, pp. 946–56, Jun. 2012.

[117] O. G. Poluektov, S. V Paschenko, L. M. Utschig, K. V Lakshmi, and M. C. Thurnauer, "Bidirectional Electron Transfer in Photosystem I : Direct Evidence from," pp. 11910–11911, 2005.

[118] R. Bittl and S. G. Zech, "Pulsed EPR Study of Spin-Coupled Radical Pairs in Photosynthetic Reaction Centers : A in Bacterial Reaction Centers," vol. 5647, no. 96, pp. 1429–1436, 1997.

[119] M. Mac, N. R. Bowlby, G. T. Babcock, and J. McCracken, "Monomeric Spin Density Distribution in the Primary Donor of Photosystem I as Determined by Electron Magnetic Resonance: Functional and Thermodynamic Implications," *J. Am. Chem. Soc.*, vol. 120, no. 50, pp. 13215–13223, Dec. 1998.

[120] S. L. Badshah, "Mutations that affect bidirectional electron transfer in photosystem I," Arizona State University, 2014.

[121] A. Van Der Est, A. I. Valieva, Y. E. Kandrashkin, G. Shen, D. A. Bryant, and J. H. Golbeck, "Removal of PsaF alters forward electron transfer in photosystem I: evidence for fast reoxidation of QK-A in subunit deletion mutants of Synechococcus sp. PCC 7002.," *Biochemistry*, vol. 43, no. 5, pp. 1264–75, Feb. 2004.

[122] R. K. Rappaport Fabrice , Diner Bruce A., "Optical Measurements of Secondary Electron Transfer in Photosystem I," *Adv. Photosynth. Respir.*, vol. 24, pp. 223–244, 2006.

[123] O. G. Poluektov, S. V Paschenko, L. M. Utschig, K. V Lakshmi, and M. C. Thurnauer, "Bidirectional electron transfer in photosystem I: direct evidence from high-frequency time-resolved EPR spectroscopy.," *J. Am. Chem. Soc.*, vol. 127, no. 34, pp. 11910–1, Aug. 2005.

[124] A. Savitsky, A. A. Dubinskii, M. Flores, W. Lubitz, and K. Möbius, "Orientation-resolving pulsed electron dipolar high-field EPR spectroscopy on disordered solids: I. Structure of spin-correlated radical pairs in bacterial photosynthetic reaction centers.," *J. Phys. Chem. B*, vol. 111, no. 22, pp. 6245–62, Jun. 2007.

[125] S. Surendran Thamarath, A. Alia, E. Roy, K. B. Sai Sankar Gupta, J. H. Golbeck, and J. Matysik, "The field-dependence of the solid-state photo-CIDNP effect in

two states of heliobacterial reaction centers.," *Photosynth. Res.*, vol. 117, no. 1–3, pp. 461–9, Nov. 2013.

[126] S. S. Thamarath, A. Alia, E. Daviso, D. Mance, J. H. Golbeck, and J. Matysik, "Whole cell nuclear magnetic resonance characterization of two photochemically active states of the photosynthetic reaction center in heliobacteria.," *Biochemistry*, vol. 51, no. 29, pp. 5763–73, Jul. 2012.

[127] M. Kobayashi, T. Hamano, M. Akiyama, T. Watanabe, K. Inoue, H. Oh-oka, J. Amesz, M. Yamamura, and H. Kise, "Light-independent isomerization of bacteriochlorophyll g to chlorophyll a catalyzed by weak acid in vitro," *Anal. Chim. Acta*, vol. 365, no. 1–3, pp. 199–203, Jun. 1998.

[128] B. Ferlez, "Electron Transfer in Reaction Centers from Heliobacterium modesticaldum," Pennsylvania State University.